# ELECTRICAL PROPERTIES OF NANOSCALE MATERIALS FOR ENERGY CONVERSION APPLICATIONS

A Dissertation

by

CODY JON CHALKER

Submitted to the Office of Graduate and Professional Studies of
Texas A&M University
in partial fulfillment of the requirements for the degree of

DOCTOR OF PHILOSOPHY

| | |
|---|---|
| Chair of Committee, | James Batteas |
| Committee Members, | Sarbajit Banerjee |
| | Dong Hee Son |
| | Jodie Lutkenhaus |
| Head of Department, | Simon North |

December 2019

Major Subject: Chemistry

ABSTRACT

Materials that show the greatest efficacy, stability and reactivity for energy conversion and storage often have hierarchical structures that range from microscale to nanoscale. There are a diverse number of ways of engineering nanomaterials but those that are from earth abundant materials or are processed from low cost methods are highly sought after.

The first section of this thesis focuses on how structuring metal oxide materials can impact their electrochemical properties. Monolayer mesoscopic $V_2O_5$ sol gels were prepared using colloidal crystal lithography. The structuring was compared to a thin film material demonstrating the structured surface showed much higher electrochemical activity, as evidenced by the cyclic voltammetry (CV). The charging and discharging was performed at various rates, with the templated structure able to retain higher capacity at rates of 1C compared to the thin film. Over extended cycling the patterned surface was also much more resilient to structural alteration as a result of the open structure.

Following from the $V_2O_5$ work sol gel $MoO_3/MoS_2$ structures were prepared on carbon fiber paper for use as an HER cathodic electrode. Two means of preparing $MoS_2$ from $MoO_3$ was assessed, one prepared by chemical vapor deposition and the other through hydrothermal sulfurization. Polarization curves, corrected for the iR drop, show very promising overpotentials of 172 mV. Calculations performed suggested that the interfacial chemistry of the $MoO_3/MoS_2$ is likely the largest contributor to the enhancement however patterning may further show potential with increased mass loading.

In the second portion of the thesis self-assembled nanowires from porphyrin monomers were assembled through ionic assembly. The electrical properties of these wires were investigated using a modified scanning probe microscope. The current-voltage characteristics that were measured suggested that the vertical conductive pathway is thickness dependent and the LUMO state is altered as result of the thickness of the wire.

As part of this work scanning thermoelectric voltage microcopy was reviewed and the important characteristics were considered. As a proof of concept a modified atomic force microscopy is used to measure the small voltages (from 1 μV-1000 mV) that were produced upon an applied thermal gradient. All noise sources were sufficiently suppressed to provide an appropriate circuit for performing a scanning measurement. A prototype board and power supply was designed to create an ambient pressure, low noise scanning thermoelectric voltage microscope.

# ACKNOWLEDGEMENTS

I would like to thank my committee chair, Prof. James D. Batteas, for all his insight in the diverse world of nanoscience and providing me a landscape which I could explore my scientific curiosities. I would also like to thank Prof. Sarbajit Banerjee, one of my committee members, for helping me during my first draft of my paper, his incredible gift of bridging various disciplines has been inspiring. Additional thanks my other committee members Prof. Dong Hee Son and Prof. Jodie Lutkenhaus for their openness and research insight.

I would also like to thank many of the staff members in the department of chemistry whom helped me develop my skills in building and troubleshooting various components in my research. In particular I would like to thank William T Seward, who was a great mentor and a talented machinist. I would also like to thank Timothy P. Pehl for his help troubleshooting circuits and giving me confidence to pursue electronics as a hobby. I would also like to thank Richard Horner and Cody Lewis with their help designing the power supply and providing guidance in proper PCB layout.

A special thanks goes out to all the colleagues that I worked with over the years. Meagan Elinski, was there from the very beginning, without her help I'm not sure I would have made it. I would also like to thank Alison Pawlicki, whom trained me in scanning tunneling microscopy and mentored me during my formative years. I'd like to also thank other members of the Batteas group for listening to my scientific ramblings, Fanglue Wu,

Zhuotong Liu, Maelani Negrito, Nathaniel Hawthorne, Thomas Reyes, Xinyuan Chen and Quentarius Moore.

I would lastly like to thank all my friends and family for their love and support. To my older brothers Jeff, Clinton and Jesse Chalker, for being there when I need you and for being the talented caring people you are. Jeremy Weaver for always lending an ear and supporting me during the hard times. John Losek and Vito Capuano for all the late night conversations about philosophical and scientific curiosities which have pushed me to get my doctoral degree. Finally my mother and father for their unconditional love and support.

CONTRIBUTORS AND FUNDING SOURCES

## Contributors

The work in this thesis was guided by a dissertation committee comprised of Professor James D. Batteas (advisor), Professor Sarbajit Banerjee, as well as Professor Dong Hee Son of the Department of Chemistry and Professor Jodie Lutkenhaus of the Department of Chemical Engineering.

Some of the samples made in chapter II were prepared by with the help of Jose Zavela, an REU student in the summer of 2014. The electrochemical data that is shown in Chapter II was performed by Hyosong An in Dr. Lutkenhaus lab. The calculations that are displayed in Chapter III were performed by Abihisek Paraji form Dr. Banerjees lab.

Some of the samples that were prepared in chapter IV were made by Thomas Reyes. Conductive probe data from Chapter IV as well as the thermalvoltage data in Chapter V was performed using Professor Karen Wooley's microscope.

## Funding Sources

This work in this dissertation was supported by U.S. National Science Foundation under CHE-1062840, CHE-1213082 and CHE-1611119.

TABLE OF CONTENTS

LIST OF FIGURES

Page

# CHAPTER I

# INTRODUCTION AND MOTIVATION: PATTERNING AND SELF ASSEMBLY O[1]F NANOMATERIALS

## 1.1 Energy Conversion Material Impact on Society

Within the last 30 years there has been a large number of weather events (wildfires, floods, droughts, etc.) that have resulted in losses accruing over 150 billion per year USD.[1] The evidence of these extreme weather patterns is linked to climate change. As a means of combating this governments have poured in an enormous number of resources into researching next generation technologies that will move us farther away from fossil fuels such as coal and oil for producing electricity. Figure 1.1 shows a list of various technologies that researchers are actively exploring for energy conversion and storage applications. Energy storage is not necessarily just the conventional energy storage such as with batteries and supercapacitors but also with newer technologies such as the use of a fly wheel. A fly wheel is a mechanical means of storing energy (instead of electrochemical energy storage such as with batteries this is a mechanical analog) by placing a flywheel with a rolling-element bearing into a vacuum chamber to reduce frictional energy losses.[2] Other types of energy storage technologies that are less well known are $H_2$ storage.[3] Storing $H_2$ or $CO_2$ can either involve storing the gas or the liquid. For storing as a liquid the use of cryogens are usually necessary (the boiling point of hydrogen is -252.8 $^oC$), for $CO_2$ dry ice is stable at much lower temperatures. Material

scientists and chemists have been developing specific types of sorbents that can store the gases so that large compressed storage is unnecessary. Technologies used for converting light into electrical energy benefit from the always changing materials research which

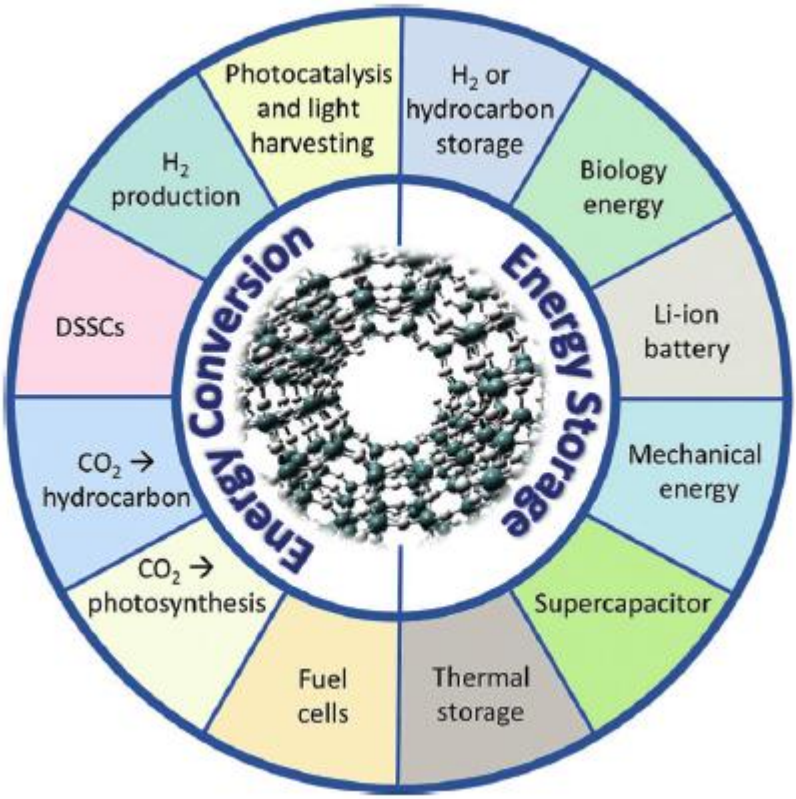


**Figure 1.1.** Schematic of various energy storage and energy conversion technologies Reprinted with permission Linares *et al*.[4] Copyright 2014 RSC Publishing.

provides increase in charge carrier mobilities, stability, and efficiency.

Collecting and storing energy using cost effective manufacturing practices is a challenge still being explored. One of the features that connects many of these technologies together is the shared interest in using nanoscience to address increasing stability, efficiency, capacity, weight as well as other figures of merit. There are many

benefits for creating nanoscale materials. For one, material physical properties change as the materials surface area increases. Figure 1.2a shows the subdivision of a material into smaller pieces. The reduction in material volume exposes more surface atoms. The nanoparticle shape (or geometry) will also affect the surface area. For example the surface area of a cube is 1.24 times larger than a sphere. As stated earlier the physical properties of materials will change as the material dimensions change. Figure 1.2b plots the density of states (DOS) of a semiconductor with different levels of dimensionality. For a bulk semiconductor small changes in DOS leads to a small change in energy. As the dimensionality decreases the DOS changes abruptly with increase in energy. The change in electronic structure helps explain the large varieties of material property changes that occur as the physical size decreases. Gold nanoparticles are an interesting example of 0D quantum dots. Depending on the size and shape of the nanoparticle the surface plasmon resonance (collective oscillations of electrons) will either red shift (increase in wavelength) or blue shift (decrease wavelength).[5] The nanoparticles will not have the same melting point and will likely have electrical properties that show coulomb blockade (a single electron tunneling event that is defined as the threshold voltage to overcome the charging energy as the inverse of the capacitance times the electric charge).[6] For 1D materials, one axis is longer than 100 nm while the others have confinement effects. Various biological and synthetic nanowires have been made with diverse applications ranging from biological sensors, battery materials to new kinds of electrical contact inks.[7] One type of 1D material that has the potential to change flexible electronics is the use of silver nanowires as the contact electrodes and the electrical path. One of the challenges of

using these materials is need for the wires to be aligned.[8, 9] 2D materials, such as graphene and $MoS_2$ have very interesting property that implications in next generation transistors, optoelectronic sensors, water splitting catalysis and thermoelectrics.[10, 11]

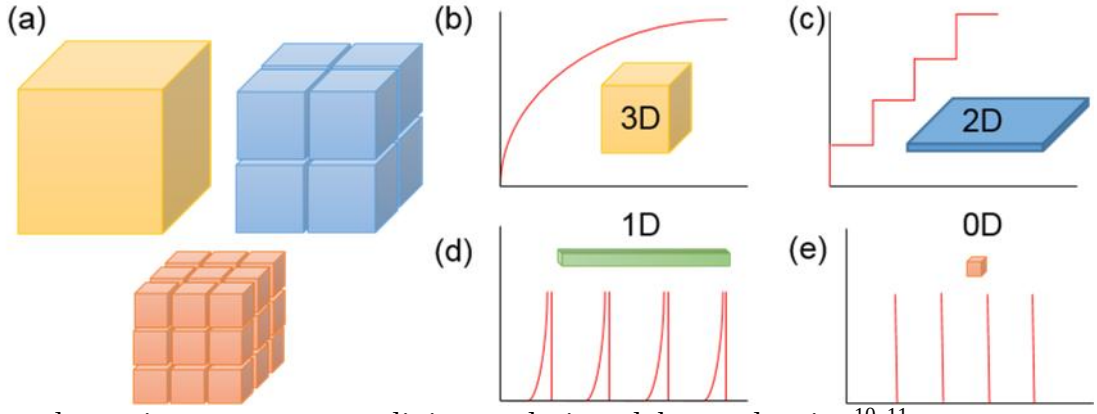


**Figure 1.2.** a) Visual depiction of increased surface area. Density of electronic states of semiconductor material for b) bulk, c) 2D sheets, d) 1D wires and e) 0D quantum dots.

### 1.2 Nanoscale Engineering:Top-Down and Bottom-Up

There are a number of ways to produce nanomaterials, some more industrious than others. The creation can be roughly generalized into to two approaches, top-down and bottom-up. It should be noted that there are some techniques that could be considered both top-down or bottom-up. Typically top-down as the approach that involves the removal of material. Figure 1.3 shows examples of fabrication methods that involve a top-down approach. An energy intensive but simple means for making nanomaterials involves what is known as ball milling (Figure 1.3a).[12] This involves the use of kinetic energy transfer from stainless steel ball bearings to the sample through collisions and friction. One of the disadvantages of this technique is that nanomaterials that are made are typically polydispersed and there may be contaminant induced from all the various

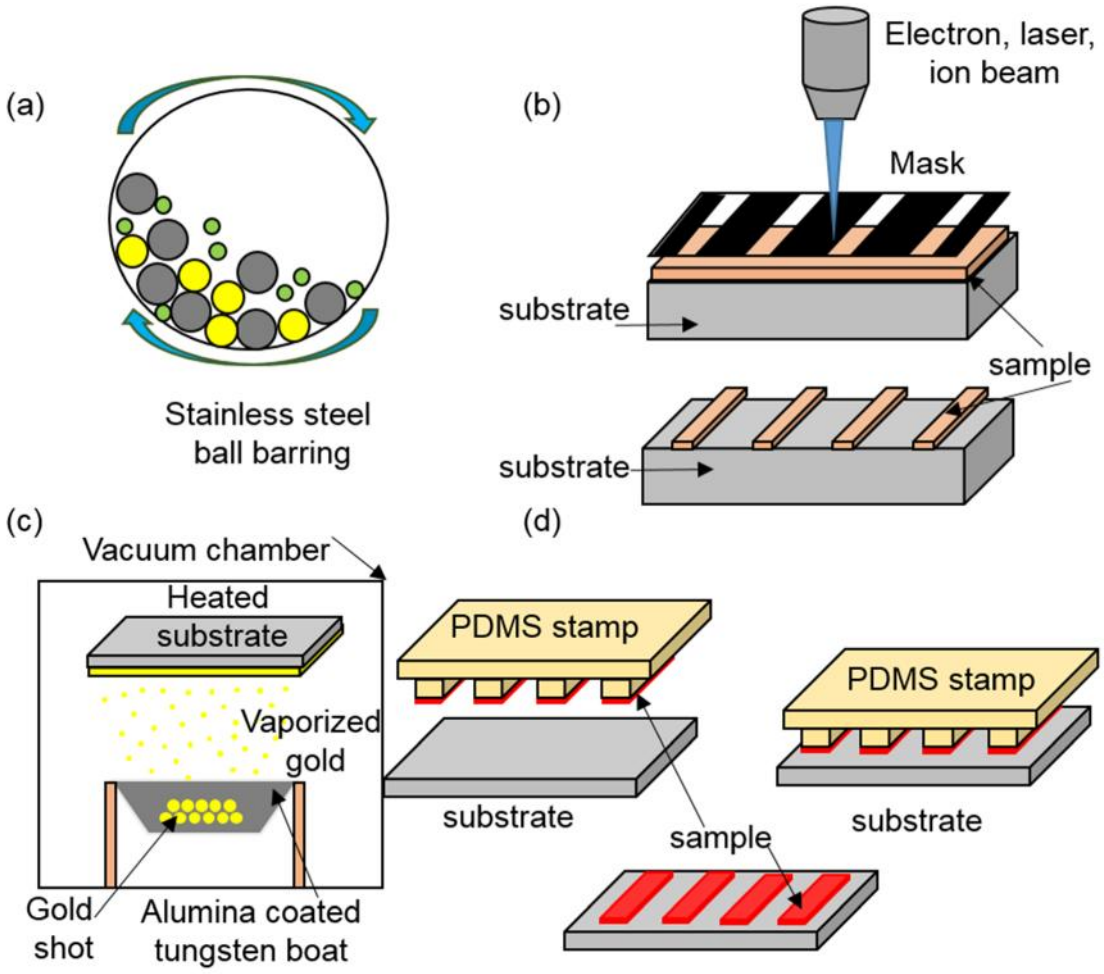


**Figure 1.3.** Various Top-down fabrication methods, a)ball milling, b)Mask/maskless lithography l, c)thermal evaporation and d)micro-contact printing.

collisions. Electronic circuit elements and microelectromechanical systems (MEMS) are typically fabricated using a broad range of techniques called top-down lithographic fabrication. Figure 1.3b shows an illustration of a mask (but the mask could also be removed) fabrication technique that uses some sort of electromagnetic radiation (such as deep UV light) to create patterns on surfaces. This is the preferred method of for creating the very small transistors as well as many integrated circuits. One of the main issues is the upfront cost for appropriate clean rooms and processing equipment make it out of reach

for all but the most resourceful organizations. Direct write methods (such as electron beam lithography and focused ion beam) can be used as “direct write” meaning that a mask is not necessary. This could be used to make electrical contacts directly onto nanomaterials as well as cutting out material to form a lamella for preparing TEM samples. Direct write methods are used most often in industry and academia for rapid prototyping and studying fundamental questions related to sample preparation, ion implantation, and plasmonic resonators among many others. The helium ion microscope has been around for some time and offers the high resolution of the scanning electron microscope and the milling capabilities of a focused ion beam. The beam currents can be made low enough to image organic materials without significant damage as well as mill away small amounts of material such as making lamella films.

Moving beyond material removal as a means of patterning surfaces, altering the phase of the material can be used for the fabrication of nanomaterials. Physical vapor deposition is a class of methods involving the deposition of material from a condensed phase, transporting through a vacuum and condensed onto a surface. Thermal evaporation (Figure 1.3c) is a technique that can deposit thin coatings of metal on surfaces. This is accomplished in a vacuum chamber which, under the reduced pressure, changes the melting point of the material by changing its vapor pressure. When current is sent through the electrical contacts to a tungsten boat (lined with alumina) the metal will undergo a phase change and evaporate into vacuum. The mean free path of the atoms in vacuum is related to the pressure so that lower pressures decrease the likelihood that atoms will collide with each other (and that contamination gases are present). The metal atoms will

evaporate on top of a target substrate and the thickness of the material added is monitored via a quartz crystal microbalance. Microcontact printing is a lithographic technique that involves the addition of molecules or particles to a patterned polydimethylsiloxane (PDMS) structure (made through a negative replica). Figure 1.3d shows a schematic that gives an overview of the process of transferring material (usually colloidal materials, self-assemble monolayer molecules etc.) to a substrate of interest. The resolution of these

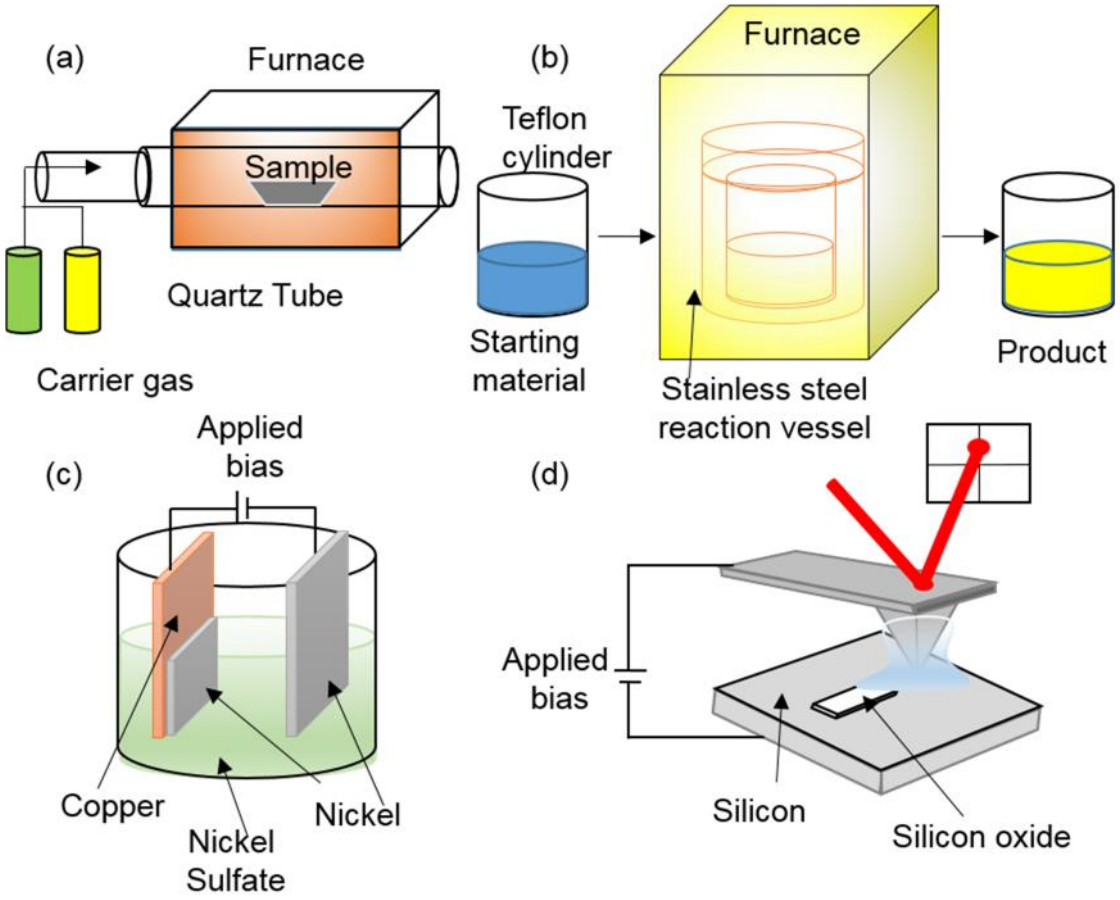


**Figure 1.4.** Various bottom-up fabrication methods, a) chemical vapor deposition, b) hydrothermal, c) electrodeposition and d) local oxidation lithography.

patterns can be as small as a 100 nm. There are in fact many other techniques that are top-down, chemical etching, erosion, photon polymerization, sonication, combustion, electrospinning, etc.

Bottom-up methods are a means of fabricating nanostructures by using building blocks (atomic or molecular) and creating a system from which the desired nanomaterial and its properties can be tailored. Chemical vapor deposition (CVD) is one of the most important techniques for making nanoscale materials from the bottom up.[13] In many cases the starting material is a gas that is carried through a quartz tube, held inside a furnace, a will deposit onto a substrate usually held in a ceramic boat (Figure 1.4a). If the carrier gas is methane for example, and the temperature is from 400 $^{o}$C-1000 $^{o}$C, decomposition of the methane gas will produce carbon nanotubes as well as hydrogen gas. There are cases where chemical vapor deposition would be seen as a top-down technique, for example, during the sulfurization of $MoO_3$ pure sulfur is added upstream from the sample substrate. Upon heating the furnace the sulfur will vaporize and deposit downstream converting the $MoO_3$ to $MoS_2$, but since the material is, in a sense, atomizing from a bulk material is this still considered bottom up? Another fabrication method that is very important in nanomaterials research is known as hydrothermal synthesis(Figure 1b).[14] This involves using a liquid or solid precursor material inside a Teflon cylinder and solvent is added to solvate the mixture. The Teflon cylinder is then placed inside a stainless steel container and sealed then placed into an oven to a certain temperature. Since the volume is fixed and the temperature is increased we expect the pressure inside the Teflon cylinder to increase. This provides the opportunity for creating materials that may have metastable

phases to be created by taking advantage of tuning the temperature and consequentially the pressure inside the reaction vessel. Electroplating is a very mature technique that allows

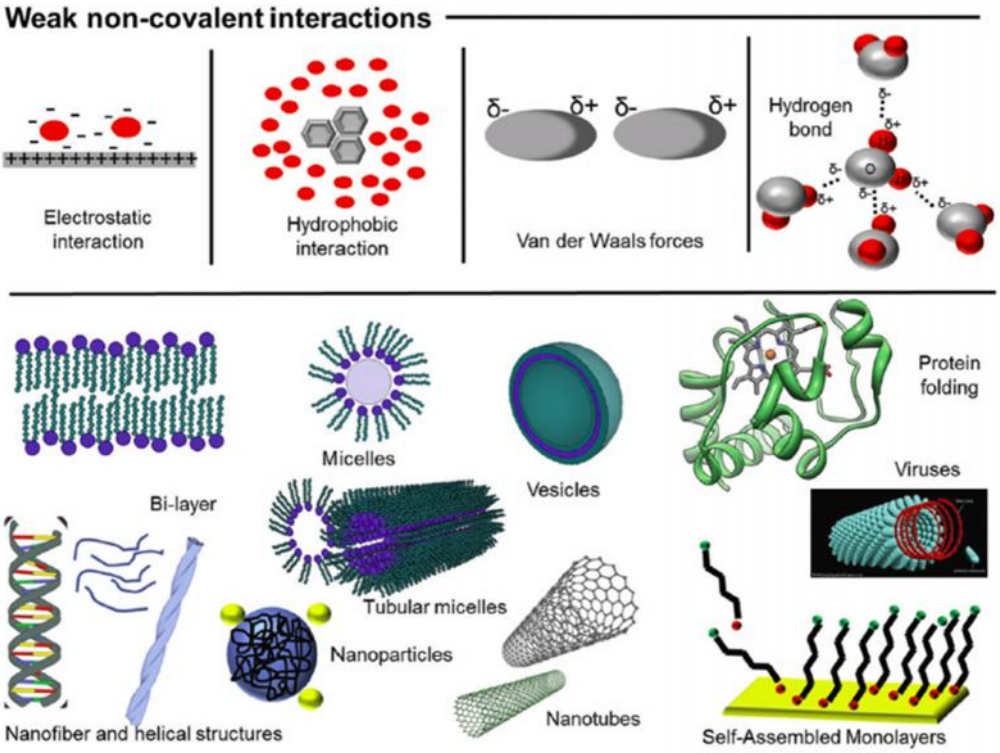


**Figure 1.5.** Schematic of different non-covalent interactions and the various biological hierarchical assemblies. Reprinted with permission Casalini *et al.*[15] Copyright 2017 RSC Publishing.

the deposition of metals on conductive surfaces. Plating over top of surfaces, such as nickel over copper, can change the properties of that surface, in this case providing better corrosion resistance (Figure 1.4c). Electroplating is an example of a bottom up manufacturing because starting from metal salts and under the influence of an electric field, atoms will deposit on the cathodic side of the cell.[16] Another technique that is very similar to electroplating is known as anodizing. Anodizing is a process that forms a porous

insulating surface over top of a conductive surface (typically aluminum).These pores that are formed can be tuned in size and depth by controlling the type of electrolytic solution, temperature and applied electric field. Interestingly the formation of these porous hexagonal structures can be combined with other fabrication techniques and create lithography templated structures.[17] These structures have a number of advantages such as being optically transparent, chemically inert, insulating as well as high thermal stability. Many interesting tubular like structures have been formed using either sol-gel infiltration, or using the nanopore template as a mask to make nanoparticle arrays separated by pore diameter.[18, 19, 20] It is also possible to deposit metal without an electric field, this is known as electroless deposition. This is an autocatalytic deposition that involves a reduction process of the metal so that it can be deposited on the material of interest, including plastics.[21, 22] A method to make nanostructures locally on the surface can be accomplished using a scanning probe microscope (SPM). As shown in Figure 1.4d an Atomic Force Microscope is being used to create $SiO_2$ on a Si(100) surface using local oxidation lithography.[23] This is accomplished by electrically connecting the tip and sample together such that a bias voltage can be applied through the tip to the grounded surface (or vice versa). The experiment is done under a humid environment with biases from 2-7 volts. Features as small as a nanometer can be made in the z-direction which is exceedingly difficult using other means of fabrication (although the through-put is very low). Other types of bottom-up assemblies that exist are the creation of single crystals of atomic and molecular precursors such as molecular beam epitaxy and atomic layer deposition.[24, 25]

Two other assemblies that are worth mentioning in some detail are supramolecular and self-assembly where their formations are ultimately driven not through direct bonding but through intermolecular and intramolecular interactions. Figure 1.5 shows a schematic detailing how various forces, electrostatic interactions, van der Waals forces, hydrogen bonding and hydrophobic effects are the forethought for researcher when trying to design molecular systems. Biological systems are completely driven by these types of forces and by understanding how complex biological structures are formed through these various levels of meta-stable states is at the heart of these strategies. A good example of the power of these types of interactions is attempting to solvate carbon nanotubes and fullerenes. The stability of the interactions between these materials (especially when having multiwall carbon nanotubes) means that bundles of these materials form, which are kinetically stable, making it necessary to use ultrasonic and aggressive solvents to unwind them. Other forces, such as hydrogen bonding, have incredible importance for supramolecular assembly, particularly with deoxyribonucleic acid (DNA) base pairing and sulfide bridges in proteins from amino acids. Combining many of the forces together give structures that begin as nanoscale assemblies but through hierarchical assembly can form macroscopic assemblies (bone, collagen, human hair, chromatin etc.)

## 1.3 Sol-Gel Chemistry and Colloidal Lithography

Sol-gel chemistry is also a bottom-up fabrication approach that has been used for over a century to make glass ceramics. In the last sixty year or so the use of sol-gel reactions have had a large impact on the fabrication of nanostructures.[26, 27] Figure 1.6

shows an over view of the process for creating nanomaterials from sol-gels. In general most sol-gel reactions start with the hydrolysis of a precursor molecule. After subsequent hydrolysis condensation of the products of hydrolysis, in addition to other growth mechanisms such as Ostwald ripening create a sol-gel network for which the morphology will depend on the various conditions. Nanoparticle synthesis was an important step in this direction

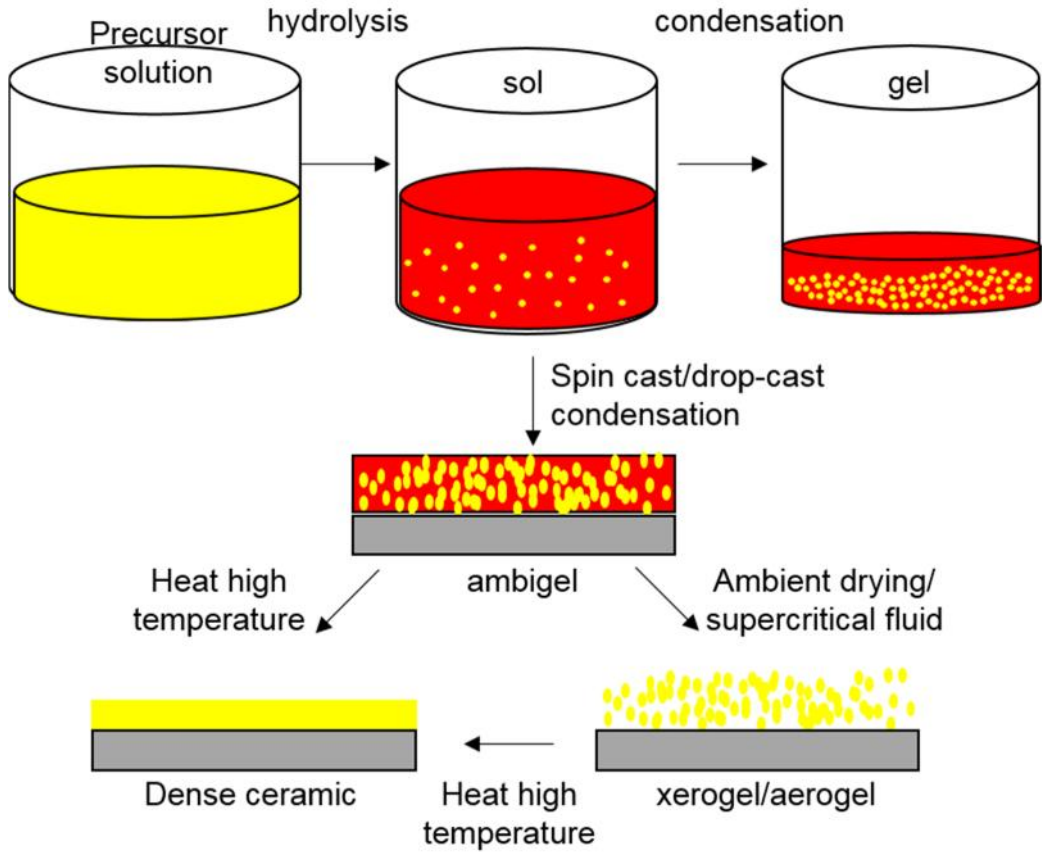


**Figure 1.6.** Schematic showing the process for sol-gel fabrication of nanomaterials and the various physical transformations.

where silica particles were fabricated using tetraethylorthosilicate, ammonium hydroxide and water.[28] The size of the particles can be directed by varying the concentration of the

precursor, the base catalysis and the temperature.[29] Other structures have been formed such as vanadium pentoxide nanowires through the use of $V_2O_5$-$H_2O_2$ precursors.[30, 31] In addition to the concentration of the precursor, the amount of water present determines the kinetics of the reaction (since hydrolysis is one of the steps in the formation). There are ways to create very high surface area sol-gel materials following the condensation of the sol-gel. Aerogels are a material where the solid material is dispersed in space through a gas. This is accomplished by removing the solvent that accompanying the sol-gel material through the use of super critical fluid extraction (usually through $CO_2$) without capillary forces collapsing the solid matrix.[32, 33, 34, 35] Xerogels are formed by removing the liquid phase without using a supercritical means. These structures most often have much less surface area as the aerogels because when the liquid is removed (usually by ambient drying or drying under vacuum) leads to a collapse of the internal structure.

In 1994 Richard van Duyne of Northwestern University developed what is known as colloidal particle lithography as a way to low cost, high throughput, nanoscale fabrication.[36] The original conception was made to provide surface enhanced Raman spectroscopy substrates by using the spheres as masks for metal evaporation. Other scientists found many additional uses for colloidal lithography using a variety of materials such as nanoparticles, quantum dots, self-assembled monolayers (SAMs), and sol-gels.[37, 38, 39, 40] The use of sol-gels has produced many publications for a variety of energy conversion applications. Figure 1.7a shows a basic schematic of templating with a sol-gel material using colloidal lithography. The spheres are ordered in a way that form a closed pack structure, in many cases drop casting the spheres on a substrate is sufficient

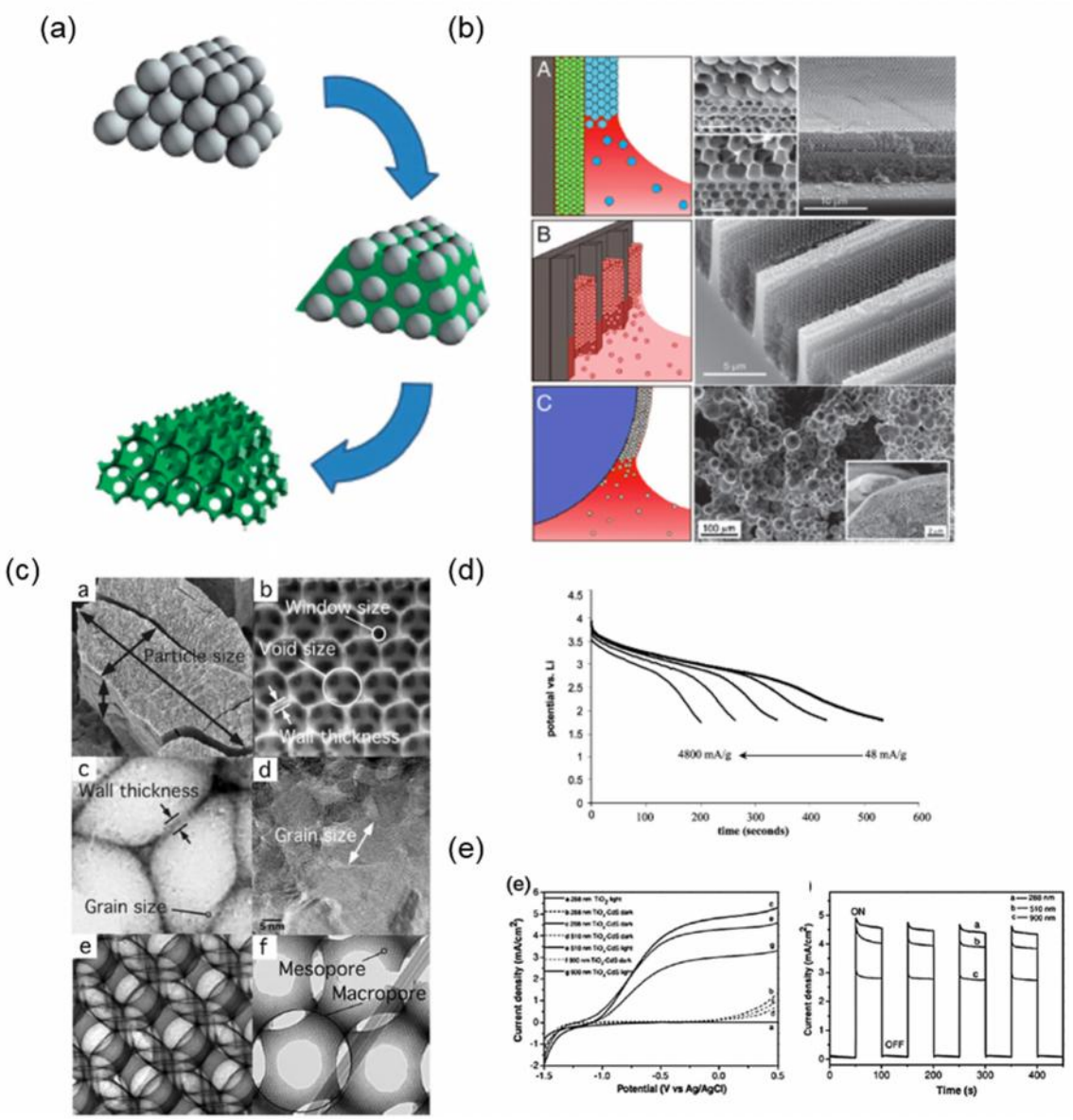


**Figure 1.7.** (a) Illustration of the templating process for colloidal crystal templating from assembly, infiltration and template removal. (b) Micro/nanosphere vertical-assembly method on arbitrarily shaped surfaces. (c) Length scales and characteristics of inverse opal structures. (d) charge-discharge curves of $V_2O_5$ inverse opal structures with rates varying from 48 mA/g to 4800 mA/g. Part (a) and (c) reproduced with permission from Stein et.al.[41] Copyright 2013. RSC Publishing. Part (b) reproduced with permission from Hatton et.al. Copyright 2010, National Academy of Sciences. Part (c) reproduced with permission from Sakamoto et.al.[42] Copyright 2002, RSC Publishing. Part (e) reproduced with permission from Chen et.al.[43] Copyright 2012, Wiley-VCH

as a first trial to see what the structures make look like after infiltrating with the precursor. Once the precursor is added usually there is time to allow the sol-gel to slowly undergo hydrolysis and condensation. Either supercritical fluid extraction is performed or the spheres are removed. The spheres can be removed through a number of ways but two of the most popular are either burning the spheres off under oxygen (or vacuum/Ar, this produces a carbon film over the inverse opal structure) or dissolving the spheres in an appropriate solvent/etching solution (for polymer spheres toluene or dichloromethane are popular and for silica spheres 0.1 M NaOH works great). The deposition of the spheres on surfaces can occur in a number of ways. As stated above simple drop casting can provide local order over a large area, albeit the thickness of the spheres and their uniformity are not well controlled. Other techniques for creating pattern surfaces have included using charged polymers spheres (sulfate terminated or amine terminated) and using electrodeposition. The advantage of this technique is the ease of deposition and the control of thickness. Spheres can also be floated on a water surface if the spheres are larger than 200 nm and in a compatible solvent such as ethanol or butanol.[44] The differences in density of the solvents as well as the hydrophobicity of the particles (polystyrene spheres) can lead to colloidal crystals that are monolayers. This layer-by-layer assemble of the spheres has implications in photonic crystals that demand a very low defect density of the pattern surfaces. The infiltration step (after depositing the spheres on a desired surface) can be done not only with a sol-gel but also by use of pre-cursor gases. Atomic layer deposition is a technique that involves the use of a precursor material (usually an alkoxide) that is flowed into a high vacuum chamber onto a templated surface. The precursor is allowed to

adsorb onto the surface and the excess is evacuated from the chamber. Water is then flowed into the chamber and hydrolysis occurs. If the conditions are well controlled (gas flow rate, temperature etc.) then an atomic layer can be formed that can be fabricated with high fidelity. A technique known as vertical deposition involves putting the precursor and the spheres together in the same solution. The substrate is held vertically in a beaker with the mixture and the solution is heated to 50 $^{o}$C. As the solvent evaporates the beads will settle onto the substrate and a gradient will form that will create the sol-gel pattern. The most interesting feature is that since capillary forces are driving the assembly surfaces with different degrees of curvature can be patterned (see Figure 1.7b).[45] Figure 1.7c shows scanning electron and transmission electron microscopy images of inverse opal structures. Characteristics can be assigned to the inverse opal structures such as the wall thickness, void size, window size, grain size, and particle size. These characteristics will determine the effect of their end use application. For example, in batteries research it has been shown that the particles with void sizes around 200 nm had a faster discharges at similar capacities, and had longer cycling stability. The patterning creates the thin wall thickness for the patterned structures which leads to smaller diffusion lengths for lithium ions and thus better performance (see Figure 1.7d). The enhancement of supercapacitors is very noteworthy as well. The increased surface area provides larger active surface sites for faradaic capacitance to occur. For both the batteries and supercapacitors there's no need to add an electrical binder for low charge/discharge rates. Photocatalysts have been made using inverse opal $TiO_2$ structures functionalized with CdS quantum dots.[43] The void sizes were varied with 900, 510 and 288 nm to see the effect on catalytic performance. Figure

1.7e shows the polarization curves of the various catalysts sizes with the light on and off and the switching behavior (current vs time plot). The 288 nm void sizes were shown to have the highest performance, this has been attributed to the thinner wall thicknesses that likely decreased electron-hole recombination and increased charge transfer capabilities.

### 1.4 Conclusion: Bottom-up Strategies for Enhanced Energy Conversion Materials

The various techniques for building nanostructures and how their material properties change as a result of this have been discussed in some detail here. Through the use of colloidal crystal templating or self-assembly inorganic and organic nanostructures can be fabricated rather easily, without much skill. In Chapter II colloidal crystal templating is used to create a monolayer of vanadium pentoxide on fluorine tin oxide surfaces. This will explore the effect of a patterned structure versus a non-patterned structure via morphological and by electrochemical means. Chapter III seeks to understand what effect colloidal crystal templating has on the catalytic performance of sol-gel derived, hydrothermally prepared $MoS_2$. Chapter IV moves away from the use of colloidal crystal templating and instead uses ionic assembly to form porphyrin nanowires. These wires electrical properties are then investigated using conductive probe atomic force microscopy. Chapter V, seeks to understand the noise characteristics and implementation of a low noise scanning thermoelectric voltage microscopy set-up to study doping of nanostructured materials at ambient pressure using a modified atomic force microscope.

## 1.5 References


1. Chu, S.; Majumdar, A. Opportunities and challenges for a sustainable energy future. *Nature* **2012,** *488* (7411), 294-303.

2. Mousavi G, S. M.; Faraji, F.; Majazi, A.; Al-Haddad, K. A comprehensive review of Flywheel Energy Storage System technology. *Renewable and Sustainable Energy Reviews* **2017,** *67*, 477-490.

3. Karellas, S.; Tzouganatos, N. Comparison of the performance of compressed-air and hydrogen energy storage systems: Karpathos island case study. *Renewable and Sustainable Energy Reviews* **2014,** *29*, 865-882.

4. Linares, N.; Silvestre-Albero, A. M.; Serrano, E.; Silvestre-Albero, J.; Garcia-Martinez, J. Mesoporous materials for clean energy technologies. *Chem Soc Rev* **2014,** *43* (22), 7681-717.

5. Yeh, Y.-C.; Creran, B.; Rotello, V. M. Gold nanoparticles: preparation, properties, and applications in bionanotechnology. *Nanoscale* **2012,** *4* (6), 1871-1880.

6. Zhao, J.; Sun, S.; Swartz, L.; Riechers, S.; Hu, P.; Chen, S.; Zheng, J.; Liu, G.-y. "Size-Independent" Single-Electron Tunneling. *The Journal of Physical Chemistry Letters* **2015,** *6* (24), 4986-4990.

7. Gong, C. C.; Sun, S. W.; Zhang, Y. J.; Sun, L.; Su, Z. Q.; Wu, A. G.; Wei, G. Hierarchical nanomaterials via biomolecular self-assembly and bioinspiration for energy and environmental applications. *Nanoscale* **2019,** *11* (10), 4147-4182.

8. Kang, S.; Kim, T.; Cho, S.; Lee, Y.; Choe, A.; Walker, B.; Ko, S.-J.; Kim, J. Y.; Ko, H. Capillary Printing of Highly Aligned Silver Nanowire Transparent Electrodes for High-Performance Optoelectronic Devices. *Nano Letters* **2015,** *15* (12), 7933-7942.

9. Tomiyama, T.; Seri, Y.; Yamazaki, H. Relationship between wire orientation and optical and electrical anisotropy in silver nanowire/polymer composite films. *Applied Surface Science* **2019,** *469*, 340-347.

10. Wang, Y.; Mao, J.; Meng, X.; Yu, L.; Deng, D.; Bao, X. Catalysis with Two-Dimensional Materials Confining Single Atoms: Concept, Design, and Applications. *Chem Rev* **2019,** *119* (3), 1806-1854.

11. Babu, V. J.; Vempati, S.; Uyar, T.; Ramakrishna, S. Review of one-dimensional and two-dimensional nanostructured materials for hydrogen generation. *Physical Chemistry Chemical Physics* **2015,** *17* (5), 2960-2986.

12. Xing, T.; Sunarso, J.; Yang, W.; Yin, Y.; Glushenkov, A. M.; Li, L. H.; Howlett, P. C.; Chen, Y. Ball milling: a green mechanochemical approach for synthesis of nitrogen doped carbon nanoparticles. *Nanoscale* **2013,** *5* (17), 7970-7976.

13. Crowell, J. E. Chemical methods of thin film deposition: Chemical vapor deposition, atomic layer deposition, and related technologies. *Journal of Vacuum Science & Technology A* **2003,** *21* (5), S88-S95.

14. Shi, W.; Song, S.; Zhang, H. Hydrothermal synthetic strategies of inorganic semiconducting nanostructures. *Chem Soc Rev* **2013,** *42* (13), 5714-5743.

15. Casalini, S.; Bortolotti, C. A.; Leonardi, F.; Biscarini, F. Self-assembled monolayers in organic electronics. *Chem Soc Rev* **2017,** *46* (1), 40-71.

16. Gurrappa, I.; Binder, L. Electrodeposition of nanostructured coatings and their characterization—A review. *Science and Technology of Advanced Materials* **2008,** *9* (4), 043001.

17. Wen, L.; Xu, R.; Mi, Y.; Lei, Y. Multiple nanostructures based on anodized aluminium oxide templates. *Nat Nanotechnol* **2017,** *12* (3), 244-250.

18. Lakshmi, B. B.; Patrissi, C. J.; Martin, C. R. Sol−Gel Template Synthesis of Semiconductor Oxide Micro- and Nanostructures. *Chemistry of Materials* **1997,** *9* (11), 2544-2550.

19. Kelly, D. N.; Wakabayashi, R. H.; Stacy, A. M. A Modified Sol–Gel Technique for Pore Size Control in Porous Aluminum Oxide Nanowire Templates. *ACS Applied Materials & Interfaces* **2014,** *6* (22), 20122-20129.

20. Lee, W.; Park, S.-J. Porous Anodic Aluminum Oxide: Anodization and Templated Synthesis of Functional Nanostructures. *Chem Rev* **2014,** *114* (15), 7487-7556.

21. Ghosh, S. Electroless copper deposition: A critical review. *Thin Solid Films* **2019,** *669*, 641-658.

22. Lahiri, A.; Pulletikurthi, G.; Endres, F. A Review on the Electroless Deposition of Functional Materials in Ionic Liquids for Batteries and Catalysis. *Frontiers in Chemistry* **2019,** *7* (85).

23. Garcia, R.; Knoll, A. W.; Riedo, E. Advanced scanning probe lithography. *Nature Nanotechnology* **2014,** *9* (8), 577-587.

24. Park, J. H.; Vishwanath, S.; Liu, X.; Zhou, H.; Eichfeld, S. M.; Fullerton-Shirey, S. K.; Robinson, J. A.; Feenstra, R. M.; Furdyna, J.; Jena, D.; Xing, H. G.; Kummel, A.

C. Scanning Tunneling Microscopy and Spectroscopy of Air Exposure Effects on Molecular Beam Epitaxy Grown WSe2 Monolayers and Bilayers. *ACS Nano* **2016,** *10* (4), 4258-4267.

25. Manfra, M. J. Molecular Beam Epitaxy of Ultra-High-Quality AlGaAs/GaAs Heterostructures: Enabling Physics in Low-Dimensional Electronic Systems. *Annual Review of Condensed Matter Physics* **2014,** *5* (1), 347-373.

26. Dislich, H.; Hinz, P. History and principles of the sol-gel process, and some new multicomponent oxide coatings. *Journal of Non-Crystalline Solids* **1982,** *48* (1), 11-16.

27. Hench, L. L.; West, J. K. The sol-gel process. *Chem Rev* **1990,** *90* (1), 33-72.

28. Stöber, W.; Fink, A.; Bohn, E. Controlled growth of monodisperse silica spheres in the micron size range. *Journal of Colloid and Interface Science* **1968,** *26* (1), 62-69.

29. Han, Y.; Lu, Z.; Teng, Z.; Liang, J.; Guo, Z.; Wang, D.; Han, M.-Y.; Yang, W. Unraveling the Growth Mechanism of Silica Particles in the Stöber Method: In Situ Seeded Growth Model. *Langmuir* **2017,** *33* (23), 5879-5890.

30. Takahashi, K.; Wang, Y.; Lee, K.; Cao, G. Fabrication and Li+-intercalation properties of V2O5-TiO2 composite nanorod arrays. *Applied Physics A* **2006,** *82* (1), 27-

31. Cao, G.; Liu, D. Template-based synthesis of nanorod, nanowire, and nanotube arrays. *Advances in Colloid and Interface Science* **2008,** *136* (1), 45-64.

32. Loy, D. A.; Russick, E. M.; Yamanaka, S. A.; Baugher, B. M.; Shea, K. J. Direct Formation of Aerogels by Sol−Gel Polymerizations of Alkoxysilanes in Supercritical Carbon Dioxide. *Chemistry of Materials* **1997,** *9* (11), 2264-2268.

33. Pierre, A. C.; Pajonk, G. M. Chemistry of Aerogels and Their Applications. *Chem Rev* **2002,** *102* (11), 4243-4266.

34. Wu, Y.; Gao, G.; Wu, G. Self-assembled three-dimensional hierarchical porous V2O5/graphene hybrid aerogels for supercapacitors with high energy density and long cycle life. *Journal of Materials Chemistry A* **2015,** *3* (5), 1828-1832.

35. Sudant, G.; Baudrin, E.; Dunn, B.; Tarascon, J. M. Synthesis and electrochemical properties of vanadium oxide aerogels prepared by a freeze-drying process. *J Electrochem Soc* **2004,** *151* (5), A666-A671.

36. Hulteen, J. C.; Van Duyne, R. P. Nanosphere lithography: A materials general fabrication process for periodic particle array surfaces. *Journal of Vacuum Science & Technology A* **1995,** *13* (3), 1553-1558.

37. Chen, J.; Liao, W.-S.; Chen, X.; Yang, T.; Wark, S. E.; Son, D. H.; Batteas, J. D.; Cremer, P. S. Evaporation-Induced Assembly of Quantum Dots into Nanorings. *ACS Nano* **2009,** *3* (1), 173-180.

38. Pravitasari, A.; Negrito, M.; Light, K.; Chang, W.-S.; Link, S.; Sheldon, M.; Batteas, J. D. Using Particle Lithography to Tailor the Architecture of Au Nanoparticle Plasmonic Nanoring Arrays. *The Journal of Physical Chemistry B* **2018,** *122* (2), 730-736.

39. Li, J.-R.; Ross, S. S.; Liu, Y.; Liu, Y. X.; Wang, K.-h.; Chen, H.-Y.; Liu, F.-T.; Laurence, T. A.; Liu, G.-y. Engineered Nanostructures of Haptens Lead to Unexpected Formation of Membrane Nanotubes Connecting Rat Basophilic Leukemia Cells. *ACS Nano* **2015,** *9* (7), 6738-6746.

40. Lusker, K. L.; Li, J.-R.; Garno, J. C. Nanostructures of Functionalized Gold Nanoparticles Prepared by Particle Lithography with Organosilanes. *Langmuir* **2011,** *27* (21), 13269-13275.

41. Stein, A.; Wilson, B. E.; Rudisill, S. G. Design and functionality of colloidal-crystal-templated materials--chemical applications of inverse opals. *Chem Soc Rev* **2013,** *42* (7), 2763-803.

42. Sakamoto, J. S.; Dunn, B. Hierarchical battery electrodes based on inverted opal structures. *Journal of Materials Chemistry* **2002,** *12* (10), 2859-2861.

43. Cheng, C.; Karuturi, S. K.; Liu, L.; Liu, J.; Li, H.; Su, L. T.; Tok, A. I. Y.; Fan, H. J. Quantum-Dot-Sensitized TiO2 Inverse Opals for Photoelectrochemical Hydrogen Generation. *Small* **2012,** *8* (1), 37-42.

44. Moon, G. D.; Lee, T. I.; Kim, B.; Chae, G.; Kim, J.; Kim, S.; Myoung, J.-M.; Jeong, U. Assembled Monolayers of Hydrophilic Particles on Water Surfaces. *ACS Nano* **2011,** *5* (11), 8600-8612.

45. Hatton, B.; Mishchenko, L.; Davis, S.; Sandhage, K. H.; Aizenberg, J. Assembly of large-area, highly ordered, crack-free inverse opal films. *Proc Natl Acad Sci U S A* **2010,** *107* (23), 10354-10359.

CHAPTER II

# FABRICATION AND ELECTROCHEMICAL PERFORMANCE OF STRUCTURED MESOSCALE OPEN SHELL $V_2O_5$ NETWORKS

## 2.1. Introduction

Vanadium pentoxide ($V_2O_5$) is a desirable cathode material for energy storage because of its low cost and availability, as well as high specific energy and power.[1, 2, 3, 4, 5, 6] However, the material's low ion diffusion coefficient and moderate electronic conductivity, which results in stabilization of small polarons at low Li-ion concentrations, have hindered its use in wider application.[7, 8] In addition, $V_2O_5$ electrodes may fracture during cycling as a result of volume expansion during cycling, leading to a loss of structural stability and rapid capacity fade.[9] Nano-structured preparation methods have proven successful for addressing the issue of cycling.[6, 8, 10, 11, 12, 13, 14]

Colloidal crystal templating (CCT) is an attractive method for the fabrication of nanostructures because of its low cost and simplicity in patterning methodology. A variety of different materials have been used as templating agents for patterning surfaces including silica,[15] poly(methyl methacrylate) PMMA,[16] and polystyrene. In particular, polystyrene microspheres are a popular choice and have been used to produce a number

---

of architectures ranging from 2D rings,[17] nanobowls,[18, 19] and 3D ordered macroporous materials.[20, 21, 22, 23, 24, 25, 26]

One popular method for fabricating CCT involves using a solvent evaporation technique at an air/water interface.[18, 27, 28] Polymer microbeads (usually polystyrene) are dispersed into ethanol and added to a water surface by pipetting slowly. The resulting dense monolayer on the water surface can be packed further by adding a surfactant such as sodium dodecyl sulfate (SDS) to create a well ordered structure. The monolayer is transferred to a desired substrate simply by scooping the beads onto the surface. The deposited structure is allowed to dry, sintered slightly below or approximately near the glass transition temperature to improve adhesion to the substrate and additional layers can then be added simply by scooping another layer on top. A precursor solution is then infiltrated into the void spaces using atomic layer deposition (ALD), chemical vapor deposition (CVD) or sol-gel methods, followed subsequently by removal of the template.

Dunn and coworkers fabricated aerogel $V_2O_5$ inverse opal networks for a battery electrode and showed that the advantage of increased surface area and open structure allowed for excellent C-rate performance at high discharge rate (4.9 A/g).[29] It was also reported that the electrochromic performance of $V_2O_5$ was enhanced by an inverse opal structure.[30] Films with small pores provide faster switching time due to decreased mass transport resistances. These studies suggest that hierarchical porous structuring are promising to improve electrochemical kinetics. Other studies have shown how the increased surface area provides an enhancement in the pseudocapacitance, which may

explain the origin for the high energy storage performance of CCT materials.[31, 32] However, the effects of hierarchical porous structure in battery electrodes have not been fully understood in terms of the cycling performance and cell impedance. Specifically, there is a lack of an investigation of $V_2O_5$ patterned by CCT (described here as "patterned $V_2O_5$) versus other structures or its analogous dense phase. Previous work has either focused on the fabrication of the CCT structures themselves, the lithium ion diffusion coefficient or pseudocapacitive effect.

Here, we present a means of investigating how a crystallized patterned $V_2O_5$ structure affects the electrochemical performance, in the context of 3D electrodes, for electrochemical energy storage. We harness a facile and robust method for making single-layer inverse opal structures to compare patterned and unpatterned $V_2O_5$ thin film electrodes of similar mass. By keeping the mass equivalent, we are able to isolate the affect of the electrode structure. Our approach uses X-ray diffraction (XRD) spectroscopy, X-ray photoelectron spectroscopy (XPS), Raman spectroscopy, cyclic voltammetry, galvanostatic cycling, and electrochemical impedance spectroscopy (EIS). We find that a patterned $V_2O_5$ structure increases the charge storage capabilities and capacity retention performance during cycling test compared to an unpatterned $V_2O_5$ electrode. The unique structure obtained by CCT patterning provides low mass transfer resistance due to higher surface area and shorter diffusion lengths for lithium ions throughout the electrode surface.

## 2.2 Experimental Methods

Polystyrene (PS) microspheres were synthesized based on a modified dispersion

polymerization approach described elsewhere.[33,34] Briefly, 17 mL of styrene, 1.5 g of 40,000 MW poly(vinylpyrrolidone) and 98 mL of anhydrous ethanol were added to a three neck round bottom flask. The solution was stirred at 200 rpm and kept at a constant temperature of 70 $^{o}$C while nitrogen was bubbled into the system. After 30 minutes nitrogen bubbling was stopped, 0.15 g of 2,2′-azobis(2-methylpropionitrile) in 28 mL of ethanol was added to the flask and the system was allowed to react for 24 hours. The synthesized microspheres were then centrifuged at 3,500 rpm for 15 minutes and washed with ethanol three times. Stocks of 1:3 v:v of polystyrene:ethanol mixtures were prepared. The nominal diameter of the PS microspheres were approximately 2.4 µm.

Fluorine tin oxide (FTO) slides (5.0 × 1.2 cm$^2$) were cleaned with dichloromethane, acetone, methanol and 18.2 MΩ•cm water sequentially for 15 minutes via sonication. Clean slides were rinsed with 18.2 MΩ•cm deionized water and dried under flowing nitrogen gas. Stock PS microsphere mixtures were slowly pipetted onto a surface of deionized water contained within a glass dish. Enough PS microspheres were added until the surface of the water was completely covered. To pack the microspheres sufficiently 12 µL of 2% w/w SDS was added to the water surface. A clean FTO slide was used to scoop a monolayer of packed microspheres onto the surface. The slide was left to dry in air then sintered at 110 °C for 10 minutes at a ramp rate of 3 °C/min.

V2O5 sol-gel precursor solutions were prepared by adding 100 µL of vanadium (V) oxytriisopropoxide (Sigma-Aldrich) to 10 mL of isopropanol in a moisture free environment (relative humidity ~0.1%). To this solution 10 µL of 18.2 MΩ•cm water was

added to produce a clear precursor. Infiltration of the PS microsphere template took place in a humidity tent (relative humidity ~10%). Approximately 45 µLs of precursor solution were pipetted slowly onto the sintered PS microsphere templates (or FTO slides in absence of microsphere template) and allowed to dry, in all, three times. After deposition the patterned $V_2O_5$ was exposed to atmospheric humidity (~45%) for 1 day, dried for 2 hours at 80 °C, and then calcined at 400 °C for 2 hours at a ramp rate of 3 °C/min.

XRD patterns were recorded using a Bruker D8 using a Cu Kα radiation source (λ = 1.5418 Å). Scanning electron microscopy (SEM, JEOL JSM-7500F) was utilized to obtain detailed morphological information of the patterned samples. A WITec Alpha300 atomic force microscope (AFM) operated in tapping mode using a silicon nitride tips with nominal radii of curvature of ~ 10 nm and 170 kHz cantilever resonance was used to image the 3D topography of the surface. A Jobin-Yvon Horiba Labram HR instrument coupled to an Olympus BX41 microscope was used to acquire Raman spectra. A diode laser with a wavelength of 785 nm was used as the excitation source. Raman spectra were acquired with spectral resolution ~ 2 $cm^{-1}$ using an 1800 lines per mm grating. XPS data were acquired with a Scientia Omicron XPS/UPS system using an Argus energy analyzer (at a pass energy of 20 eV) and a Mg $K_\alpha$ band (1253.6 eV) for the excitation source at a take-off angle was 90°. The power for the source was 300 W (acceleration voltage 15kV, current 20.0 mA). A CN-10 electron flood gun was used for charge neutralization.

Electrochemical characterization was performed in a three-electrode cell using separate lithium ribbons as the anode and reference electrode. The working electrode, the $V_2O_5$-coated FTO slide (patterned or unpatterned), was dried in a vacuum oven at 70 °C

for 12 hours prior to electrochemical testing. A Solartron 1260/1287 and Biologic SP-200 were used for cyclic voltammetry (CV), charge-discharge (CD), and EIS data acquisition. For EIS, the frequency range was from 100 kHz to 10 mHz with 10 mV AC amplitude. The electrolyte consisted of 0.5 M lithium perchlorate in propylene carbonate. All electrochemical tests were performed in an argon-filled glove box (MBraun). The mass of the electrode was determined by weighing the substrate before and after fabrication using a 5-decimal balance (Mettler Toledo Company XS205, +/- 0.01 mg) with typical masses around 0.2 mg with the masses of the patterned and unpatterned $V_2O_5$ material varying by no more than 10%.

## 2.3. Results and Discussion

The fabrication procedure for creating the mesostructured patterned $V_2O_5$ is illustrated in Figure 2.1. Drop-casting of the alkoxide precursor onto the PS microsphere template, in a properly controlled humid environment, allowed for the void spaces to be filled via a sol-gel reaction. Sol-gel hydrolysis and condensation is an ideal reaction for patterning nanoarchitectures since the $V_2O_5$ can quickly and easily mold to the patterned PS template. The alkoxide, vanadium (V) oxytriisopropoxide, reacts with atmospheric moisture, to form a xerogel. The structures formed from the resulting hydrolysis and condensation reactions depend on the hydrolysis ratio, $h=(H_2O)/(V_2O_5)$, the moles of water to moles of $V_2O_5$.[35] A high concentration of water molecules relative to precursor ($h >100$) forms structures that are long and ribbon-like, which by eye are red in color.

For lower concentration ratios (i.e. $h\sim1$), molecular oligomers form, which yields a

more continuous film (at a cost of a decrease in surface area) and gives an orange appearance. The low hydrolysis ratio is preferred since uncontrolled hydrolysis has the

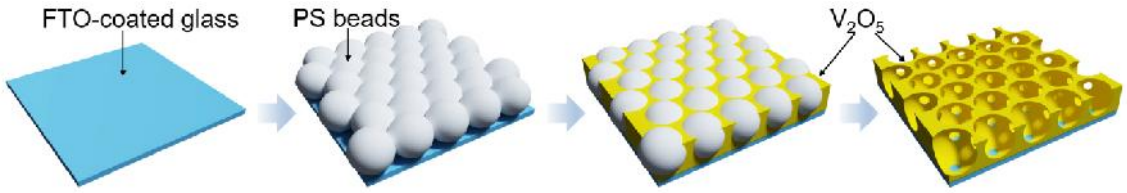


**Figure 2.1.** Schematic representation for fabricating open shell patterned $V_2O_5$ structures

disadvantage of displacing the PS microspheres across the surface leading to large cracks in the $V_2O_5$ film after calcination.[36] A low viscosity liquid, such as isopropanol, was used as the solvent so that the precursor could completely wet the surface and establish good contact with the substrate providing desirable adhesive properties. It is important to note that the PS microspheres need to be properly sintered to the substrate to avoid being displaced upon drop casting the precursor, otherwise only small patterned domains are obtained. The time and temperature of the sintering were chosen so as not to sinter the spheres to the point that they would have little to no void spaces but instead allow the template structure to remain intact during infiltration. Following infiltration, the $V_2O_5$ was calcined to form the crystalline $V_2O_5$ structure. The calcination served two purposes; first it crystallized the $V_2O_5$ and second it conveniently burned off the PS microspheres, leaving a $V_2O_5$ open shell network. Due to the need for thermal treatment, FTO was chosen as the current collector as it has good thermal stability. SEM images (Figure 2.2 a,b ) show the morphology of unpatterned and patterned $V_2O_5$ structure and Figure 2.3 shows the FTO surface. The uniformity of the $V_2O_5$ shells was consistent with the packing of the PS microsphere template throughout the entire electrode surface. These open thin structures

allow for a minimal $Li^+$ diffusion distance into the layered $V_2O_5$, reducing the undesirable effects of concentration polarization as well as a smaller effect of volumetric expansion throughout the electrode. There are approximately six interior pores per shell which allow for a highly porous morphology. The domain sizes of the open shell structures formed

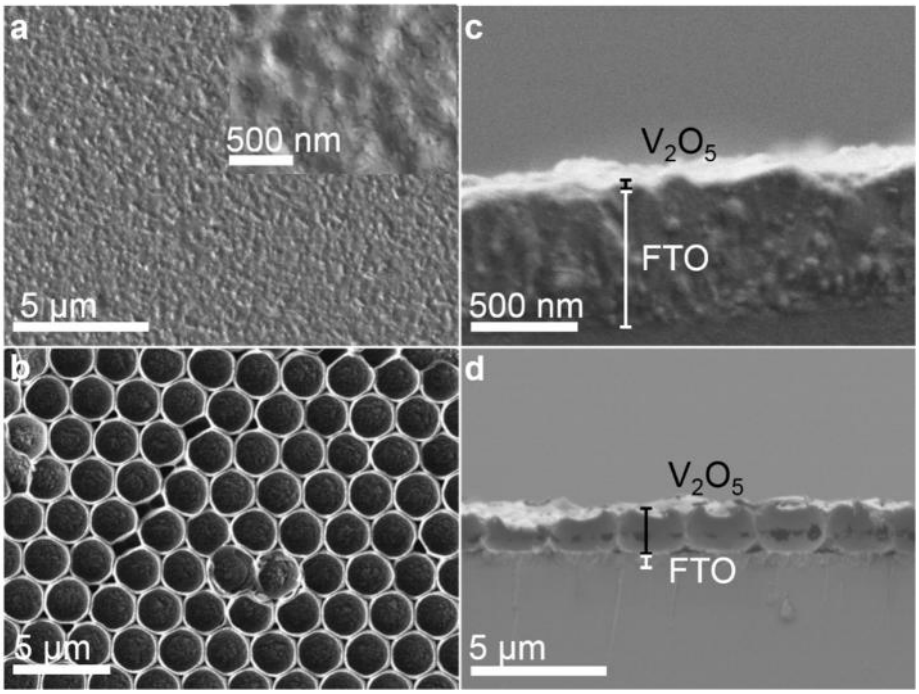


**Figure 2.2.** SEM images of (a) unpatterned $V_2O_5$ (higher resolution in the inset) and (b) patterned $V_2O_5$. (c) Side view of unpatterned $V_2O_5$, (d) side view of patterned $V_2O_5$

were on average 70 × 70 $\mu m^2$ with grain boundaries creating disconnected areas, however these grain boundaries are not likely to strongly affect the electrochemical performance. The height of the patterned surface was ~ 1.1 µm on average (however they could be as large as 2 µm), which corresponds to approximately half of the diameter of the PS microspheres (Figure 2.4 a,b) used to create the structures.

Unlike the patterned $V_2O_5$ electrode, the unpatterned $V_2O_5$ electrode suffers from a non-uniform particulate morphology. The $V_2O_5$ sol-gel fills in the grains of the FTO, decreasing the surface area of the material. Figure 2.2 c shows a cross sectional view of

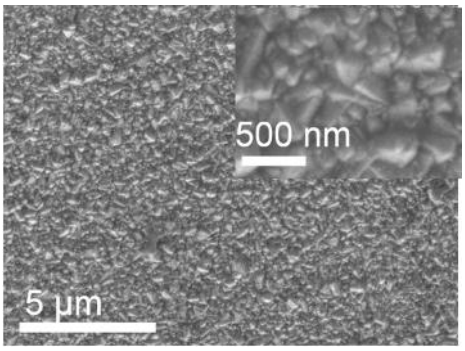


**Figure 2.3** SEM image of FTO electrode inset shows higher resolution image.

the unpatterned substrate. The thickness of the material varies across the whole surface as a result of the drop casting technique however it was approximately 40-150nm. Figure 2.2d shows a cross sectional view of the patterned $V_2O_5$ on FTO. The thickness of the patterned material varied between 75-110 nm, a much more narrow thickness distribution. This is reasonable since other authors have reported a thickness variance based on the size of the microspheres used.[30, 31] From powder X-ray diffraction measurements (Figure 2.5a), the phase of the patterned crystallized $V_2O_5$ bowl structures was found to be orthorhombic (space group Pmmn). Using $2\theta=20.1°$, corresponding to the (001) plane, the crystallite size was calculated from the Scherrer equation (integral breadth) to be ~31 nm for the patterned and ~25 nm for unpatterned $V_2O_5$ electrode. It is worth noting that the Scherrer broadening of XRD reflections is likely also derived to some extent from strain within the substrate-integrated thin films.

XPS of the V(2p) region (Figure 2.5b) for the open shell sample, showed two peaks for the V($2p^{3/2}$) and V($2p^{1/2}$) at binding energies of 517.5 eV and 524.9 eV, respectively, illustrating that the open shell $V_2O_5$ structures were composed of the expected $V^{5+}$ species.

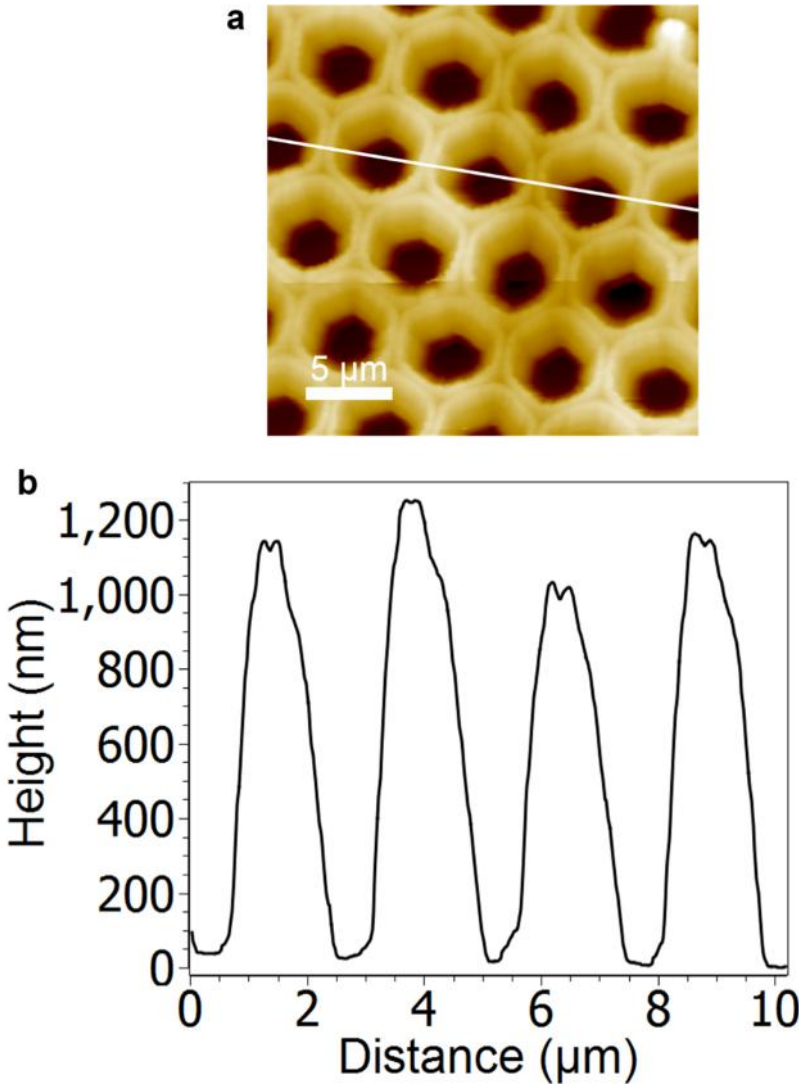


**Figure 2.4.** (a) AFM image topography of the patterned $V_2O_5$ open shell network. (b) Cross-section of (a).

The measured Raman spectra (Figure 2.5c) were consistent with the XPS and XRD analysis. The Raman spectrum for the patterned $V_2O_5$ surface showed strong peak intensities indicative of a well-structured material. The Raman bands of interest for $V_2O_5$ lie within the regions of 200 $cm^{-1}$ to 1000 $cm^{-1}$ .[37, 38] The sharp peak at 1000 $cm^{-1}$

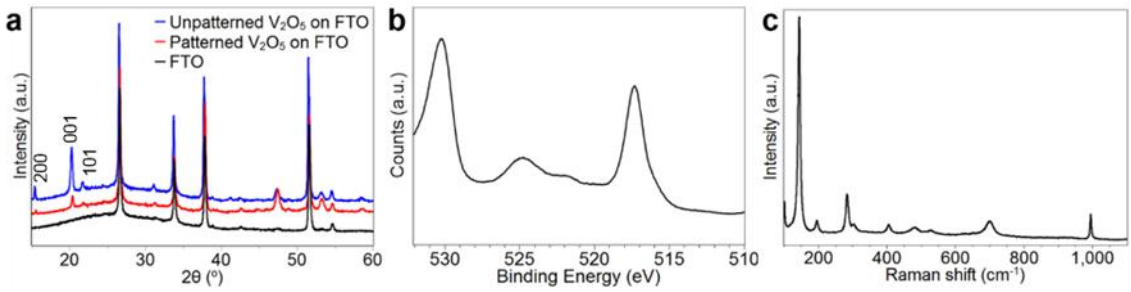


**Figure 2.5.** (a) XRD patterns, (b) XPS -V(2p) spectra, and (c) Raman spectra acquired for patterned $V_2O_5$ structures.

corresponds to the vanadyl V=O stretching mode. The next highest modes at 701 $cm^{-1}$ and 523 $cm^{-1}$ are the double and triple coordinated oxygen stretching modes respectively. The lower frequency modes at 480 $cm^{-1}$ and 303 $cm^{-1}$ are the doubly coordinated oxygen and triply coordinated oxygen bending modes, and modes at 405 $cm^{-1}$ and 287 $cm^{-1}$ are attributed to the C=O bond rocking oscillations.

Cyclic voltammetry of unpatterned and patterned $V_2O_5$ films were carried out in the range of 2-3.8 V vs. $Li/Li^+$ at a scan rate 1 mV/s (Figure 2.6a) for electrodes of similar mass. For the unpatterned $V_2O_5$, three anodic peaks at around 2.6 V, 3.3 V, and 3.5 V, corresponding to the γ/δ, δ/ε, and ε/α phase transitions for $V_2O_5$ were observed.[39, 40, 41, 42] The patterned film displayed a similar response, but with sharper redox peaks. With increasing scan rate, the unpatterned $V_2O_5$ film (Figure 2.6b) exhibited only a small increase in current

response. In contrast, the patterned $V_2O_5$ (Figure 2.6c) showed a much larger increase in current response. This is indicative of the open shell structure being more accessible to lithium ions, resulting in good electrochemical activity even at higher scan rates.[43, 44]

The total charge stored as a result of both the capacitive and diffusion-controlled (intercalation) mechanisms was calculated using the CV data and plotted in Figure 2.7.[45]

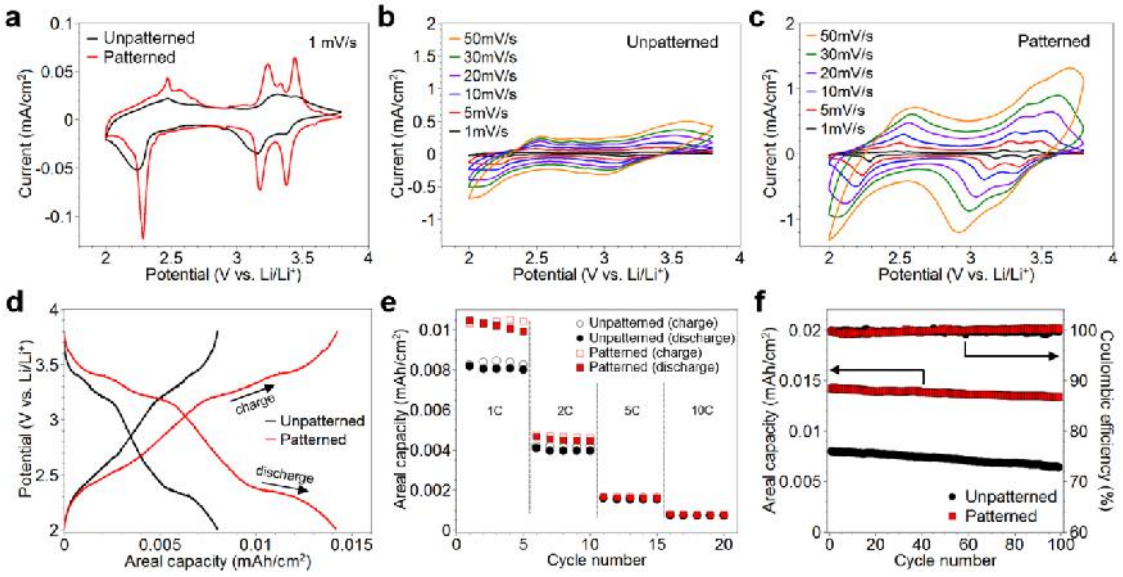


**Figure 2.6.** Cyclic voltammograms of (a) unpatterned and patterned $V_2O_5$ electrodes at 1 mV/s, (b) unpatterned $V_2O_5$ at various scan rates, and (c) patterned $V_2O_5$ at various scan rates. Unpatterned and patterned $V_2O_5$ electrodes were 40 μg/cm$^2$ and 38 μg/cm$^2$ in mass per area. (d) Charge-discharge behavior at 1 C-rate, (e) rate capability, and (f) cycling behavior of unpatterned $V_2O_5$ and patterned $V_2O_5$ electrodes. Open- and closed-dots are charge and discharge capacity values, respectively.

Both unpatterned and patterned electrodes had a similar intercalation ability. The patterned electrode showed a higher capacitance contribution compared to the

unpatterned due to higher surface area. The total stored charge of the patterned electrode was about 1.7 higher than that of the unpatterned electrode. These results reveal that patterning improves the capacitance contribution for energy storage which is consistent with the literature.[31, 32]Figure 4d shows first galvanostatic charge-discharge cycle for the unpatterned and patterned $V_2O_5$ films in the range of 2 V – 3.8 V vs. $Li/Li^+$ at rate of 1 C.

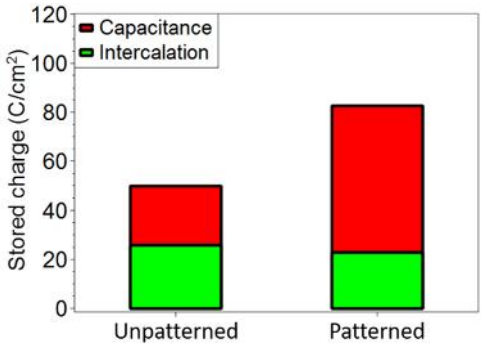


**Figure 2.7.** Total charge stored with capacitive and intercalation contributions of unpatterned and patterned $V_2O_5$ electrodes. Scan rate 1 mV/s.

The curve shapes are typical of crystalline $V_2O_5$.[41, 42] Three discharge plateaus at about 3.4 V, 3.2 V and 2.4 V were observed, corresponding to the peaks observed in the cyclic voltammetry. Figure 2.8 shows the galvanostatic charge discharge behavior for the case when capacities are normalized by the actual surface area measured by AFM. The patterned electrode (8.03 $cm^2$) showed 1.7 times higher surface

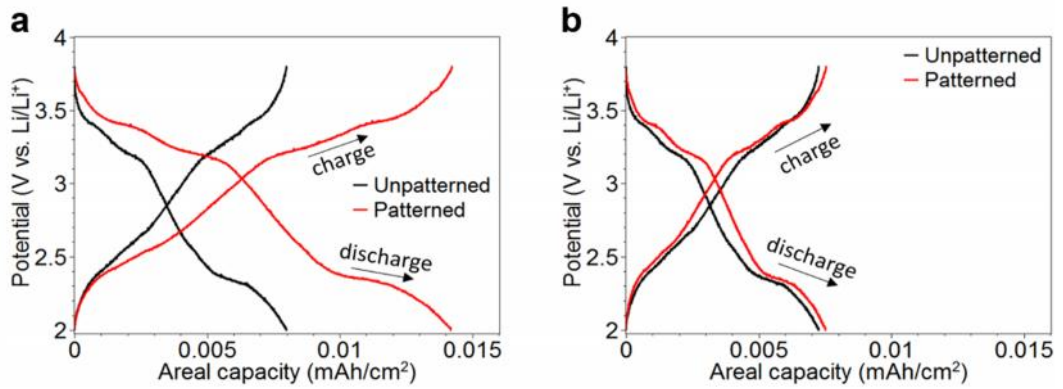


**Figure 2.8.** Charge-discharge behavior (a) based on the projected surface area of the underlying substrate and (b) based on the measured surface area of electrodes by AFM. Test C-rate is 1 C.

area compared to the unpatterned electrode (4.68 $cm^2$) (surface area was measured using AFM). Consequently, the normalized areal capacities were quite close to each other. This demonstrates the impact of texture and surface area brought by the CCT approach. Figure 2.6e shows continuous cycling behavior at various C-rates from 1 C to 10 C. The patterned $V_2O_5$ exhibited an enhanced rate capability at 1 C and 2 C, although the rate performance of both were similar at higher C-rates. This is not surprising since the electrical conductivity of $V_2O_5$ is quite low and no carbon binders were added to either electrode systems. At 1 C-rate, the average areal discharge capacity for the unpatterned $V_2O_5$ electrode was 8.1 $\mu Ah/cm^2$ whereas for the patterned $V_2O_5$ electrode the discharge capacity was higher at 10.2 $\mu Ah/cm^2$. These values correspond to a specific capacity of 200 mAh/g for the unpatterned electrode and 269 mAh/g for the patterned electrode. These values equate to lithium insertion levels for $Li_xV_2O_5$ of x=1.36 and x=1.83 for the unpatterned and patterned electrodes, respectively.

Figure 2.6f illustrates the cycling behavior and coulombic efficiency of the unpatterned and patterned $V_2O_5$ electrodes at rate of 1 C. For the unpatterned $V_2O_5$ electrode, the discharge capacity gradually decreased during cycling. Patterned $V_2O_5$ electrodes showed a similar decline in capacity, retaining 94% of the initial discharge capacity after 100 cycles. Both unpatterned and patterned $V_2O_5$ electrodes exhibited an average coulombic efficiency of about 100%. SEM images of the electrodes before (Figure 2.9) and after (Figure 2.10) cycling of the electrodes show how well the patterned structure can tolerate repeated cycling. On the other hand, the unpatterned substrate showed a dramatic difference in morphology after cycling. In a separate but identical experiment (Figure 2.11), the discharge capacity of the unpatterned $V_2O_5$ gradually decreased during

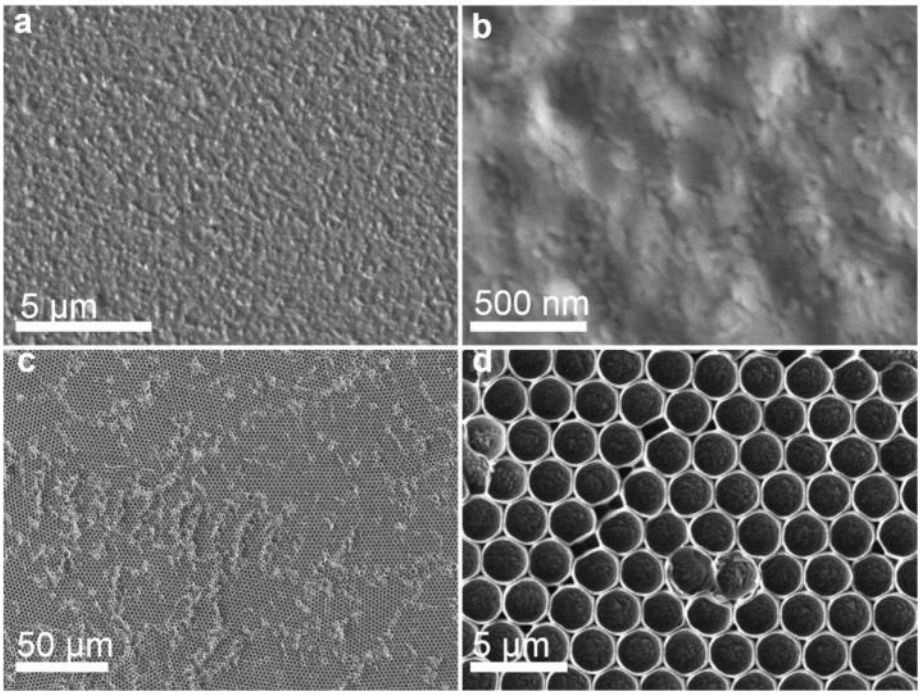


**Figure 2.9.** SEM images of unpatterned $V_2O_5$ (a, b) and patterned $V_2O_5$ (c, d) before galvanic cycling.

cycling until a dramatic decline at the 80th cycle. This is most likely a result of volume expansion and pulverization. This is most likely a result of volume expansion.[46, 47] Figure 2.12 shows the XRD pattern before and after cycling, which indicates that the FTO crystal structure was largely unaffected by repeated cycling and that no ordered $V_2O_5$ crystallites appeared due to the lithium intercalation.

Electrochemical impedance spectroscopy (EIS) of the unpatterned and patterned $V_2O_5$ electrodes at 2.4 V vs. $Li/Li^+$ is shown in Figure 2.13. The impedance spectra were analyzed using the equivalent circuits shown in Figure 2.13a and 2.13b.[48, 49, 50] The elements in both equivalent circuits include the ohmic resistance ($R_e$) of the cell

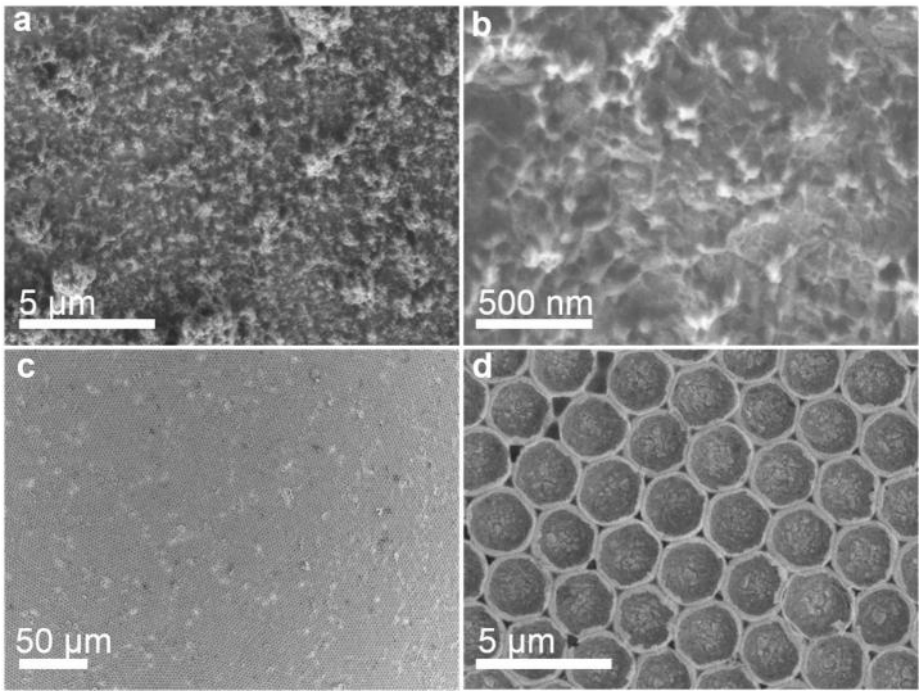


**Figure 2.10.** SEM images of unpatterned $V_2O_5$ (a, b) and patterned $V_2O_5$ (c, d) after galvanic cycling.

components and electrolyte, the combined resistances of the surface film and the charge transfer resistance ($R_{sf+ct}$), a constant phase element ($CPE_i$) (i = surface film (sf), double layer (dl)), and the Warburg impedance ($Z_W$). In addition, the equivalent circuit for the unpatterned film includes a bulk resistance ($R_b$) and a corresponding phase element ($CPE_b$). In the Nyquist plot (Figure 2.13c), the $R_e$ values of both the unpatterned $V_2O_5$ and patterned $V_2O_5$ electrodes were similar (47.7 Ω vs. 41.4 Ω). For the unpatterned $V_2O_5$ electrode the, $R_{sf+ct}$ (393.8 Ω) was much higher than for the patterned $V_2O_5$ electrode (13.2 Ω). The unpatterned $V_2O_5$ has a $R_b$ (4586.0 Ω) element arising from the need to flow electrons across an insulating wide band gap material from the surface, which in this system is known to occur through propagation of small polarons.[7] The patterned $V_2O_5$

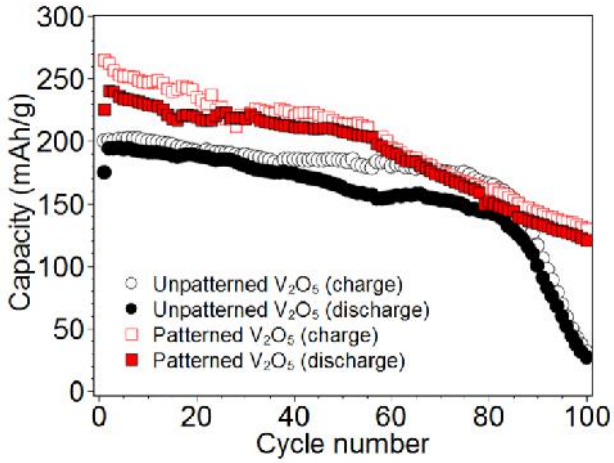


**Figure 2.11.** Second trial of galvanostatic cycling at 1 C-rate. Open-and closed-dots are charge and discharge capacity values, respectively.

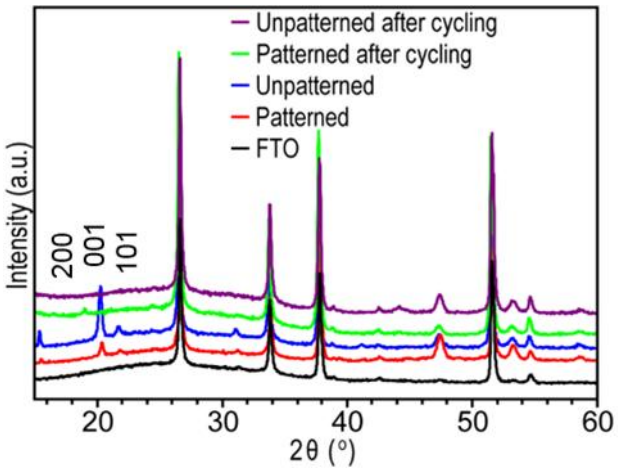


**Figure 2.12.** XRD of patterned and unpatterned electrodes before and after cycling.

electrode does not have an $R_b$ element, as indicated by slope in the Bode plot (Figure 2.13d), since the electrolyte interface and the current collector is separated by an ultra-thin layer, substantially mitigating polaronic impediments to charge transport.[7] By comparing the phase angle in the low-frequency region, mass transfer resistance (mainly of $Li^+$) can be evaluated.[48, 51] The angle of unpatterned $V_2O_5$ (38°) was lower than that of the patterned

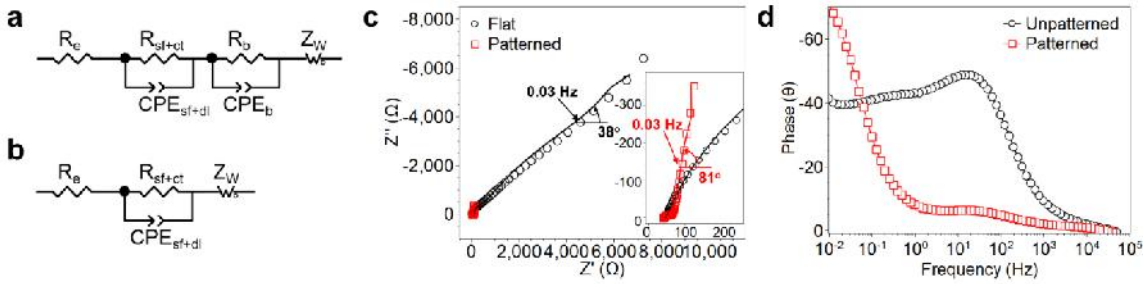


**Figure 2.13. (**a) Equivalent circuit models of (a) unpatterned and (b) patterned $V_2O_5$ electrodes. Nyquist plots for unpatterned and patterned $V_2O_5$ electrodes at 2.4 V. The experimental data and fitted curves are dots and solid lines, respectively. The inset shows the expanded curves at the high frequency region. The AC amplitude was 10 mV. The frequency range was from 100 kHz to 10 mHz. (d) Bode plots of the experimental data of unpatterned and patterned $V_2O_5$ electrodes at 2.4V.

$V_2O_5$ (81°), indicating greater mass transfer resistance in the unpatterned film. As expected, these results suggest that patterning effectively improves electrode kinetics by providing higher surface area and shorter diffusion lengths for lithium ions throughout the electrode surface. From electrochemical impedance spectroscopy at 2.4 V vs. $Li/Li^+$, the diffusion coefficients ($D_{Li^+}$) were determined for the unpatterned and patterned electrodes as $4.7 \times 10^{-13}$ $cm^2/s$ and $4.6 \times 10^{-10}$ $cm^2/s$, respectively. [52, 53, 54] This shows an enhancement in ion transport with patterning.

## 2.4 Conclusion

In summary, a mesostructured open shell patterned $V_2O_5$ network was fabricated using CCT and the electrochemical performance was examined. $V_2O_5$ precursors were infiltrated into colloidal crystal templates consisting of PS microspheres. Following calcination, crystalline open shell patterned $V_2O_5$ electrodes were obtained. These high surface area patterned electrodes were compared against unpatterned $V_2O_5$ electrodes of comparable mass. By increasing the surface area using the open shell structure, the capacity and cyclability were enhanced. The capacity of the patterned open shell electrode at 1 C was approximately 78% higher as compared to the unpatterned, and approximately 94% of the initial capacity was retained after 100 cycles. This was attributed to an increase in the pseudocapacitance of the patterned structure (due to the greater surface area) and resistance to failure by volume expansion. This work has shown quantitatively the added benefits of patterning a $V_2O_5$ electrode system. Future work will be focused on thicker hybrid $V_2O_5$ containing a redox active polymer.

## 2.5 References


1. Chan, C. K.; Peng, H.; Twesten, R. D.; Jarausch, K.; Zhang, X. F.; Cui, Y. Fast, completely reversible Li insertion in vanadium pentoxide nanoribbons. *Nano Lett.* **2007,** *7* (2), 490-495.

2. Galiote, N. A.; Camargo, M. N.; Iost, R. M.; Crespilho, F.; Huguenin, F. Effects of self-assembled materials prepared from $V_2O_5$ for lithium ion electroinsertion. *Langmuir* **2011,** *27* (19), 12209-17.

3. Liu, J.; Xia, H.; Xue, D.; Lu, L. Double-shelled nanocapsules of $V_2O_5$-based composites as high-performance anode and cathode materials for Li ion batteries. *J. Am. Chem. Soc.* **2009,** *131* (34), 12086-12087.

4. Yan, J.; Sumboja, A.; Khoo, E.; Lee, P. S. V2O5 Loaded on $SnO_2$ Nanowires for High-Rate Li Ion Batteries. *Adv. Mater.* **2011,** *23* (6), 746-750.

5. Pan, A.; Zhang, J.-G.; Nie, Z.; Cao, G.; Arey, B. W.; Li, G.; Liang, S.-q.; Liu, J. Facile synthesized nanorod structured vanadium pentoxide for high-rate lithium batteries. *J. Mater. Chem.* **2010,** *20* (41), 9193-9199.

6. Li, Y.; Yao, J.; Uchaker, E.; Yang, J.; Huang, Y.; Zhang, M.; Cao, G. Leaf-Like $V_2O_5$ Nanosheets Fabricated by a Facile Green Approach as High Energy Cathode Material for Lithium-Ion Batteries. *Adv. Energy. Mater.* **2013,** *3* (9), 1171-1175.

7. De Jesus, L. R.; Horrocks, G. A.; Liang, Y.; Parija, A.; Jaye, C.; Wangoh, L.; Wang, J.; Fischer, D. A.; Piper, L. F.; Prendergast, D.; Banerjee, S. Mapping polaronic states and lithiation gradients in individual $V_2O_5$ nanowires. *Nat Commun* **2016,** *7,* 12022.

8. Wang, Y.; Takahashi, K.; Lee, K.; Cao, G. Nanostructured vanadium oxide electrodes for enhanced lithium-ion intercalation. *Adv. Funct. Mater.* **2006,** *16* (9), 1133.

9. Sun, X.; Zhou, C.; Xie, M.; Hu, T.; Sun, H.; Xin, G.; Wang, G.; George, S. M.; Lian, J. Amorphous vanadium oxide coating on graphene by atomic layer deposition for stable high energy lithium ion anodes. *Chem. Commun.* **2014,** *50* (73), 10703-10706.

10. Cao, A. M.; Hu, J. S.; Liang, H. P.; Wan, L. J. Self-assembled vanadium pentoxide ($V_2O_5$) hollow microspheres from nanorods and their application in lithium-Ion batteries. *Angew. Chem. Int. Ed.* **2005,** *44* (28), 4391-4395.

11. Zhai, T.; Liu, H.; Li, H.; Fang, X.; Liao, M.; Li, L.; Zhou, H.; Koide, Y.; Bando, Y.; Golberg, D. Centimeter-Long $V_2O_5$ Nanowires: From Synthesis to Field-Emission, Electrochemical, Electrical Transport, and Photoconductive Properties. *Adv. Mater.* **2010,** *22* (23), 2547-2552.

12. Wang, H. g.; Ma, D. l.; Huang, Y.; Zhang, X. b. Electrospun $V_2O_5$ Nanostructures with Controllable Morphology as High-Performance Cathode Materials for Lithium-Ion Batteries. *Chem. Eur. J.* **2012,** *18* (29), 8987-8993.

13. Pan, A.; Wu, H. B.; Yu, L.; Lou, X. W. D. Template-Free Synthesis of $VO_2$ Hollow Microspheres with Various Interiors and Their Conversion into $V_2O_5$ for Lithium-Ion Batteries. *Angew. Chem.* **2013,** *125* (8), 2282-2286.

14. Nguyen, T. D.; Do, T. O. Solvo-hydrothermal approach for the shape-selective synthesis of vanadium oxide nanocrystals and their characterization. *Langmuir* **2009,** *25* (9), 5322-32.

15. Zhang, X.; Yan, W.; Yang, H.; Liu, B.; Li, H. Gaseous infiltration method for preparation of three-dimensionally ordered macroporous polyethylene. *Polymer* **2008,** *49* (25), 5446-5451.

16. Lange, B.; Jhaveri, S. J.; Steidl, L.; Ayothi, R.; Ober, C. K.; Zentel, R. Creating Defined 3-D Defects Inside an Opaline Ormocer® Matrix with Two-Photon Lithography. *Macromol. Rapid Commun.* **2007,** *28* (8), 922-926.

17. Chen, J.; Liao, W.-S.; Chen, X.; Yang, T.; Wark, S. E.; Son, D. H.; Batteas, J. D.; Cremer, P. S. Evaporation-induced assembly of quantum dots into nanorings. *ACS Nano* **2008,** *3* (1), 173-180.

18. Park, H. K.; Yoon, S. W.; Do, Y. R. Fabrication of wafer-scale $TiO_2$ nanobowl arrays via a scooping transfer of polystyrene nanospheres and atomic layer deposition for their application in photonic crystals. *J. Mater. Chem. C.* **2013,** *1* (9), 1732-1738.

19. Dai, Z.; Lee, C.-S.; Kim, B.-Y.; Kwak, C.-H.; Yoon, J.-W.; Jeong, H.-M.; Lee, J.-H. Honeycomb-like periodic porous $LaFeO_3$ thin film chemiresistors with enhanced gas-sensing performances. *ACS. Appl. Mater. Interfaces.* **2014,** *6* (18), 16217-16226.

20. Rudisill, S. G.; Wang, Z.; Stein, A. Maintaining the structure of templated porous materials for reactive and high-temperature applications. *Langmuir* **2012,** *28* (19), 7310-24.

21. Hong, J.-Y.; Oh, W.-K.; Shin, K.-Y.; Kwon, O. S.; Son, S.; Jang, J. Spatially controlled carbon sponge for targeting internalized radioactive materials in human body. *Biomaterials* **2012,** *33* (20), 5056-5066.

22. Qi, D.; Lu, L.; Wang, L.; Zhang, J. Improved SERS Sensitivity on Plasmon-Free $TiO_2$ Photonic Microarray by Enhancing Light-Matter Coupling. *J. Am. Chem. Soc.* **2014,** *136* (28), 9886-9889.

23. Gao, R.; Hu, L.; Chen, M.; Wu, L. Controllable Fabrication and Photoelectrochemical Property of Multilayer Tantalum Nitride Hollow Sphere-Nanofilms. *Small* **2014,** *10* (15), 3038-3044.

24. Kim, J.-H.; Kang, S. H.; Zhu, K.; Kim, J. Y.; Neale, N. R.; Frank, A. J. Ni–NiO core–shell inverse opal electrodes for supercapacitors. *Chem. Commun.* **2011,** *47* (18), 5214-5216.

25. Woo, S.-W.; Okada, N.; Kotobuki, M.; Sasajima, K.; Munakata, H.; Kajihara, K.; Kanamura, K. Highly patterned cylindrical Ni–Sn alloys with 3-dimensionally ordered macroporous structure as anodes for lithium batteries. *Electrochim. Acta* **2010,** *55* (27), 8030-8035.

26. Sorensen, E. M.; Barry, S. J.; Jung, H.-K.; Rondinelli, J. M.; Vaughey, J. T.; Poeppelmeier, K. R. Three-dimensionally ordered macroporous $Li_4Ti_5O_{12}$: effect of wall structure on electrochemical properties. *Chem. Mater.* **2006,** *18* (2), 482-489.

27. Gao, P.; He, J.; Zhou, S.; Yang, X.; Li, S.; Shen, J.; Wang, D.; Yu, T.; Ye, J.; Cui, Y. Large-Area Nanosphere Self-Assembly by a Micro-Propulsive Injection Method for High Throughput Periodic Surface Nanotexturing. *Nano Lett.* **2015**.

28. Moon, G. D.; Lee, T. I.; Kim, B.; Chae, G.; Kim, J.; Kim, S.; Myoung, J.-M.; Jeong, U. Assembled monolayers of hydrophilic particles on water surfaces. *ACS Nano* **2011,** *5* (11), 8600-8612.

29. Sakamoto, J. S.; Dunn, B. Hierarchical battery electrodes based on inverted opal structures. *J. Mater. Chem.* **2002,** *12* (10), 2859-2861.

30. Tong, Z.; Hao, J.; Zhang, K.; Zhao, J.; Su, B.-L.; Li, Y. Improved electrochromic performance and lithium diffusion coefficient in three-dimensionally ordered macroporous $V_2O_5$ films. *J. Mater. Chem. C.* **2014,** *2* (18), 3651-3658.

31. Tong, Z. Q.; Xu, H. B.; Liu, G. Q.; Zhao, J. P.; Li, Y. Pseudocapacitive effect and Li+ diffusion coefficient in three-dimensionally ordered macroporous vanadium oxide for energy storage. *Electrochem. Commun.* **2016,** *69*, 46-49.

32. Armstrong, E.; McNulty, D.; Geaney, H.; O'Dwyer, C. Electrodeposited Structurally Stable $V_2O_5$ Inverse Opal Networks as High Performance Thin Film Lithium Batteries. *ACS. Appl. Mater. Interfaces.* **2015,** *7* (48), 27006-27015.

33. Song, J.-S.; Winnik, M. A. Cross-linked, monodisperse, micron-sized polystyrene particles by two-stage dispersion polymerization. *Macromolecules* **2005,** *38* (20), 8300-8307.

34. Li, F.; Geng, C.; Yan, Q. Growth Kinetics of Monodisperse Polystyrene Microspheres Prepared by Dispersion Polymerization. *Int. J. Polym. Sci.* **2013,** *2013*.

35. Livage, J. Vanadium pentoxide gels. *Chem. Mater.* **1991,** *3* (4), 578-593.

36. Glynn, C.; Creedon, D.; Geaney, H.; O'Connell, J.; Holmes, J. D.; O'Dwyer, C. Optimizing Vanadium Pentoxide Thin Films and Multilayers from Dip-Coated Nanofluid Precursors. *ACS. Appl. Mater. Interfaces.* **2014,** *6* (3), 2031-2038.

37. Abello, L.; Husson, E.; Repelin, Y.; Lucazeau, G. Vibrational spectra and valence force field of crystalline $V_2O_5$. *Spectrochim. Acta, Part A* **1983,** *39* (7), 641-651.

38. Horrocks, G. A.; Likely, M. F.; Velazquez, J. M.; Banerjee, S. Finite size effects on the structural progression induced by lithiation of $V_2O_5$: a combined diffraction and Raman spectroscopy study. *J. Mater.Chem. A.* **2013,** *1* (48), 15265-15277.

39. Braithwaite, J.; Catlow, C.; Gale, J.; Harding, J. Lithium intercalation into vanadium pentoxide: a theoretical study. *Chem. Mater.* **1999,** *11* (8), 1990-1998.

40. Li, Y.; Yao, J.; Uchaker, E.; Zhang, M.; Tian, J.; Liu, X.; Cao, G. Sn-Doped $V_2O_5$ Film with Enhanced Lithium-Ion Storage Performance. *J. Phys. Chem. C.* **2013,** *117* (45), 23507-23514.

41. Liu, Y.; Clark, M.; Zhang, Q.; Yu, D.; Liu, D.; Liu, J.; Cao, G. $V_2O_5$ Nano-Electrodes with High Power and Energy Densities for Thin Film Li-Ion Batteries. *Adv. Energy. Mater.* **2011,** *1* (2), 194-202.

42. Chae, O. B.; Kim, J.; Park, I.; Jeong, H.; Ku, J. H.; Ryu, J. H.; Kang, K.; Oh, S. M. Reversible lithium storage at highly populated vacant sites in an amorphous vanadium pentoxide electrode. *Chem. Mater.* **2014,** *26* (20), 5874-5881.

43. Li, Z.; Zhao, T.; Zhan, X.; Gao, D.; Xiao, Q.; Lei, G. High capacity three-dimensional ordered macroporous $CoFe_2O_4$ as anode material for lithium ion batteries. *Electrochim. Acta* **2010,** *55* (15), 4594-4598.

44. Goldman, J. L.; Long, B. R.; Gewirth, A. A.; Nuzzo, R. G. Strain Anisotropies and Self-Limiting Capacities in Single-Crystalline 3D Silicon Microstructures: Models for High Energy Density Lithium-Ion Battery Anodes. *Adv. Funct. Mater.* **2011,** *21* (13), 2412-2422.

45. An, H.; Li, X.; Chalker, C.; Stracke, M.; Verduzco, R.; Lutkenhaus, J. L. Conducting Block Copolymer Binders for Carbon-Free Hybrid Vanadium Pentoxide Cathodes with Enhanced Performance. *ACS Appl Mater Interfaces* **2016**. *8*, (42), 28585-28591.

46. Zhang, C.; Chen, Z.; Guo, Z.; Lou, X. W. D. Additive-free synthesis of 3D porous $V_2O_5$ hierarchical microspheres with enhanced lithium storage properties. *Energy Environ. Sci.* **2013,** *6* (3), 974-978.

47. Wang, Y.; Cao, G. Li+-intercalation electrochemical/electrochromic properties of vanadium pentoxide films by sol electrophoretic deposition. *Electrochim. Acta* **2006,** *51* (23), 4865-4872.

48. Zhou, G.; Wang, D.-W.; Yin, L.-C.; Li, N.; Li, F.; Cheng, H.-M. Oxygen bridges between NiO nanosheets and graphene for improvement of lithium storage. *ACS Nano* **2012,** *6* (4), 3214-3223.

49. Sakunthala, A.; Reddy, M.; Selvasekarapandian, S.; Chowdari, B.; Selvin, P. C. Energy storage studies of bare and doped vanadium pentoxide,$(V_{1.95}M_{0.05})O_5$, M=Nb, Ta, for lithium ion batteries. *Energy Environ. Sci.* **2011,** *4* (5), 1712-1725.

50. Reddy, M.; Subba Rao, G.; Chowdari, B. Preparation and characterization of $LiNi_{0.5}Co_{0.5}O_2$ and $LiNi_{0.5}Co_{0.4}Al_{0.1}O_2$ by molten salt synthesis for Li ion batteries. *J. Phys. Chem. C.* **2007,** *111* (31), 11712-11720.

51. Sun, J.; Zheng, G.; Lee, H.-W.; Liu, N.; Wang, H.; Yao, H.; Yang, W.; Cui, Y. Formation of Stable Phosphorus–Carbon Bond for Enhanced Performance in Black

Phosphorus Nanoparticle–Graphite Composite Battery Anodes. *Nano Lett.* **2014,** *14* (8), 4573-4580.

52. Yu, J. J.; Yang, J.; Nie, W. B.; Li, Z. H.; Liu, E. H.; Lei, G. T.; Xiao, Q. Z. A porous vanadium pentoxide nanomaterial as cathode material for rechargeable lithium batteries. *Electrochim. Acta* **2013,** *89*, 292-299.

53. Levi, M. D.; Lu, Z.; Aurbach, D. Li-insertion into thin monolithic $V_2O_5$ films electrodes characterized by a variety of electroanalytical techniques. *J. Power Sources* **2001,** *97-8*, 482-485.

54. Navone, C.; Baddour-Hadjean, R.; Pereira-Ramos, J. P.; Salot, R. A kinetic study of electrochemical lithium insertion into oriented $V_2O_5$ thin films prepared by rf sputtering. *Electrochim. Acta* **2008,** *53* (8), 3329-3336.

# CHAPTER III

# CATALYTIC ENHANCEMENT OF HYDROTHERMALLY GROWN $MOS_2$ THROUGH PARTICLE LITHOGRAPHY

## 3.1 Introduction

Clean, affordable energy is a challenge that is being approached through the development of technologies that can harness (wind, solar) as well as store energy (batteries, supercapacitors). Water splitting is a process that can occur either photocatalytically or electrocatalytically to produce hydrogen, a fuel that has a very high energy density. The hydrogen evolution reaction (HER, $2H^+ + 2e^- \rightarrow H_2$) is the cathodic portion of the half-cell reaction and is a two electron transfer reaction with one catalytic intermediate. In order to achieve high energetic efficiency the reaction requires a catalyst that can minimize the overpotential to drive the reaction. Platinum is considered to be the standard for the highest performing catalyst with a near zero overpotential in acidic medium.[1, 2, 3] However; since platinum is prohibitively expensive compared to other energy technologies, finding an earth abundant materials as an active catalyst is a very active field of research. Among the number of potential candidates for next generation HER catalysts are the dichalcogenides. Molybdenum based sulfides ($MoS_2$),[4, 5, 6] carbides $Mo_2C$,[7, 8, 9] and phosphides (MoP)[10, 11, 12] are promising earth abundant materials for HER

catalysts that were originally not considered useful until work related to nanostructuring $MoS_2$ showed a large increase in HER activity.[13, 14, 15]

A number of theoretical works and experiments were devised that were designed to understand why $MoS_2$ has such high catalytic activity. It was predicated that the edge states of the $MoS_2$ are the geometric points of highest activity and a number of papers have experimentally shown enhanced HER with selective design to enhance the edge sites. With this knowledge there are a number of studies that looked into structuring $MoS_2$ in ways that either exposed the edge sites by increasing surface area and/or preferential orientation.[4, 16, 17]

In this work colloidal crystal templating is used as a means of nanostructuring $MoS_2$ on carbon fiber paper for increasing the catalytic activity. The use of the sol gel allows for ease of structure formation with a colloidal crystal templates that has been successful in other architectural strategies. Comparing whether chemical vapor deposition sulfurized or hydrothermal sulfurization provides higher HER activity will be assessed. In addition calculations have been performed to identify possible synergetic interface effects of $MoS_2/MoO_3$ to the catalytic enhancement.

## 3.2 Experimental Methods

Polystyrene (PS) microspheres were synthesized based on a modified dispersion polymerization approach described elsewhere.[18, 19] Briefly, 17 mL of styrene, 1.5 g of 40,000 MW poly(vinylpyrrolidone) and 98 mL of anhydrous ethanol were added to a three neck round bottom flask. The solution was stirred at 200 rpm and kept at a constant

temperature of 70 $^{o}$C while nitrogen was bubbled into the system. After 30 minutes nitrogen bubbling was stopped, 0.15 g of 2,2′-azobis(2-methylpropionitrile) in 28 mL of ethanol was added to the flask and the system was allowed to react for 24 hours. The synthesized microspheres were then centrifuged at 3,500 rpm for 15 minutes and washed with ethanol three times. Stocks of 1:3 v:v of polystyrene:ethanol mixtures were prepared. The nominal diameter of the PS microspheres were approximately 2.4 µm.

The molybdenum acid peroxide sol-gel was synthesized following the work described by Zheng.[20] Briefly 1 g of molybdenum (Sigma-Aldrich, purity ≥99.5%) was reacted with 7 mL of 30% (v/v) aqueous hydrogen peroxide (Sigma-Aldrich, purity 29.0-32.0%) in a 150 mL beaker under ice water bath. An orange-red solution is obtained by stirring the above mixture for 4-5 minutes. The obtained solution was then diluted by adding distilled water till the total volume of the solution is 20 mL. Care must be taken with the solution because the reaction with hydrogen peroxide can last several days, unreacted peroxide can decompose to $O_2$ (g) leading to pressure increase in a sealed vial that can be an explosive hazard. The diluted sol-gel was then mixed 1:1 v/v with 2.5 % w/v PS microspheres. Carbon fiber paper (CFP) (Toray Paper 120) was cleaned via UV-ozone for 5 mins and washed with water to render the surface more hydrophilic. A piece of scotch tape was added to the top of each CFP sample to create a 1 cm$^2$ area sample. Using a micropipette, 150 $\mu$L of the sol-gel/microsphere mixture is added homogeneously across 1 cm$^2$ area of the CFP. The sol-gel/microsphere deposited CFP was dried in air and then annealed at 400 $^{o}$C in argon atmosphere between 1-3 hours, sample 1 (S1) and Sample 2 (S2) respectively. The annealed samples were either sulfurized by chemical vapor

deposition (CVD) or hydrothermally. CVD was accomplished by placing the substrate in the middle of the furnace downstream from an alumina boat containing 100mg of elemental sulfur powder (Alfa Aesar, 99.95% purity). The furnace was purged with Ar flow of 100 sccm and heated 20 $^{o}$C/min to a final temperature of 600 $^{o}$C for 1 hour. For hydrothermal sulfurization the annealed $MoO_3$ on CFP samples were added to a solution of 100 mg of thioacetamide (Sigma-Aldrich, purity ≥ 99.0%) and 16 mL water in a teflon cell. The $MoO_3$ on CFP samples with their respective solutions are annealed in the hydrothermal vessels to 210 $^{o}$C for 12 hours Sample 3 (S3). The samples are then removed from the vessels, washed with distilled water and dried by blowing argon.

The morphology of the as-synthesized samples were examined by filed-emission scanning electron microscopy using a JEOL JSM-7500F instrument. A Jobin-Yvon HORIBA LabRAM HR800 instrument coupled to an Olympus BX41 microscope was used to acquire Raman spectra. The excitation from the 514.5 nm line of an Ar ion laser with a 50x objective. To minimize photo-oxidation the power of the laser was kept below 10 mW. Raman spectra were acquired with a spectral resolution ~2 $cm^{-1}$ using an 1800 lines per mm grating.

Electrochemical characterization was performed in a three-electrode cell setup using a Bio-Logic potentiostat (SP-200) to measure the HER performance of the synthesized materials. For HER 0.5 M aqueous solution of $H_2SO_4$ purged with $N_2$ gas were used. The as-synthesized catalysts, on CFP were used individually as the working electrodes. The saturated calomel electrode (SCE) and a glassy carbon electrode were used as reference and counter electrodes, respectively. For HER, the formula used to convert

the potential *vs.* SCE ($E_{SCE}$) to the potential *vs.* the reversible hydrogen electrode (RHE) ($E_{RHE}$) was: $E_{RHE} = E_{SCE} + (0.241 + 0.059 \times pH)$ V.[4, 21, 22] Linear sweep voltammetry (LSV) was used in the range between 0.0 to –0.5 V *vs.* RHE for HER at a scan rate of 10 mV/s to measure the polarization curve. The ohmic potential drop (*iR*) losses were accounted for during the measurement of polarization curve, where *R* is the series resistance of the electrochemical cell measured by performing electrochemical impedance spectroscopy (EIS). The EIS was performed using a frequency range of 50 mHz to 200 kHz, with an AC amplitude of 25 mV at –0.15 V (*vs.* RHE in 0.5 M $H_2SO_4$).

The electronic structure calculations were performed using density functional theory (DFT),[23] as implemented in a Vienna *ab initio* simulation package (VASP).[24, 25] Generalized gradient approximation (GGA) of Perdew–Burke–Ernzerhof (PBE) functionals were used to implement the electron exchange-correlation interactions.[26] The electron–ion interactions were implemented in our calculations by using projector-augmented wave (PAW) formalism with a kinetic energy cutoff of 600 eV.[27] The on-site Coulomb interactions were included by using the rotationally invariant density functional theory (DFT+*U*) formalism of Dudarev *et al*.[28] For molybdenum atoms we used an on-site coulomb interaction parameter of U = 6.3 eV as suggested elsewhere in literature.[29] In the calculation of density of states, a Γ-point centered Monkhorst−Pack reciprocal grid of $2 \times 2 \times 2$ k-points was used for first Brillouin zone sampling. Whereas $2 \times 2 \times 2$ k-points reciprocal grid was used for the relaxation of the structures. To simulate the interfaces, supercell structure of $MoS_2$ (001), and $MoO_3$ (010) surfaces were used. The lattice mismatch for such surfaces is less than 2%. The structures were considered to be

relaxed until each Cartesian force component was less the 0.1 eV/Å unless otherwise noted. To avoid interlayer interactions due to periodic boundary conditions the distance between the motifs was kept at more than 10 Å. The cell size was kept fixed while the atoms were allowed to relax during the calculations of the structures. To accurately simulate the interlayer separations, the van der Waals interactions were included in the calculations by using the Grimme vdW-D2 approach.[30]

### 3.3 Results and Discussion

The stepwise synthetic process comprising of dropcasting, annealing, and CVD/hydrothermal sulfurization used to prepare catalytic samples is shown in Figure 3.1a. The first step involves the Mo sol-gel precursor forming into peroxo-polymolybdates by reacting Mo metal with hydrogen peroxide.[20, 31] Hydrogen peroxide acts as both an oxidizing agent and a complexing agent. The reaction is as follows:

$2Mo\ (s) + 10\ [H_2O_2] \leftrightarrow [Mo_2(O)_3(O_2)_4(H_2O)_2]^{2-} + 2[H_3O^+] + 5H_2O$ … (Eq. 1)

In more acidic solution (pH < 3), the dimeric species polymerizes to form tetraperoxtetramolybdate complex:

$2[Mo_2(O)_3(O_2)_4(H_2O)_2]^{2-} + 2[H_3O^+] \leftrightarrow [Mo_4(O)_9(O_2)_4]^{2-} + 4[H_2O_2] + 3H_2O$ … (Eq. 2)

As the concentration of $[H_3O^+]$ decreases, $[Mo_4(O)_9(O_2)_4]^{2-}$ reacts with water to form $[Mo_4(O)_{12}(O_2)_2]^{2-}$, and then coordinates and aggregates with water to form $[Mo_4(O)_{12}(O_2)_2(H_2O)_4]_n^{4n-1}$ and eventually the molybdenum acid peroxide sol-gel ($H_{4n}[Mo_4(O)_{12}(O_2)_2(H_2O)_4]_n$) is synthesized.

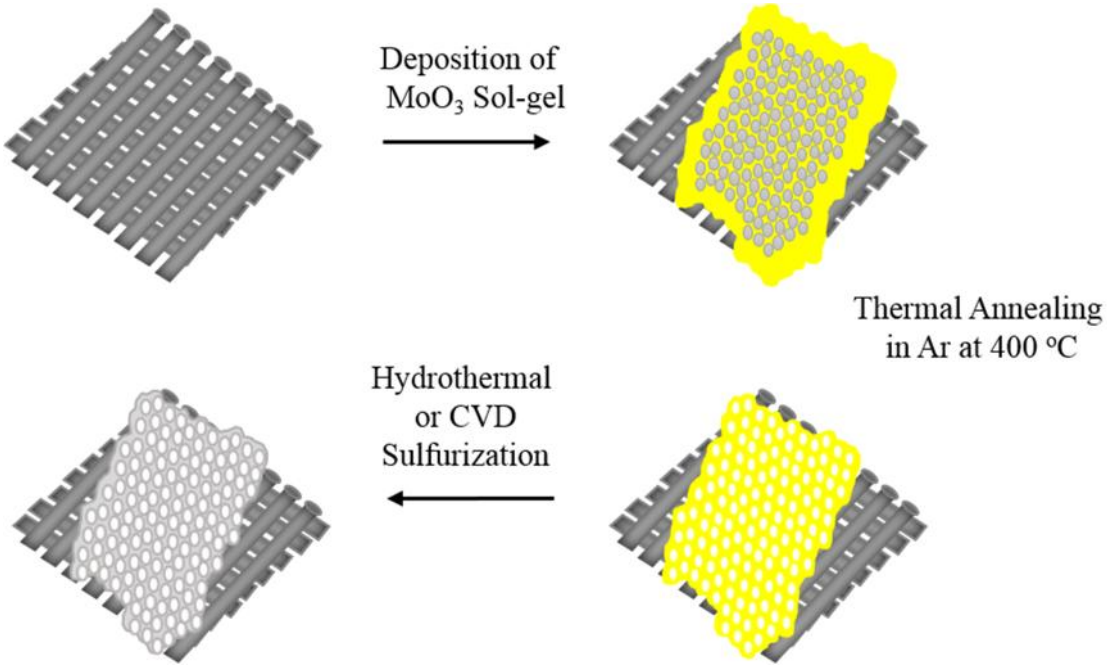


**Figure 3.1.** Schematic representation for step-wise process for creating inverse opal $MoS_2$ catalytic substrates via drop-casting, annealing and sulfurization.

The second step, 100 µL of the sol-gel/microsphere mixture is drop-casted homogeneously on the carbon fiber paper (CFP) as seen in Figure 3.2a. After allowing the sample which is then annealed at 400 °C in an argon environment to form $MoO_3$. The annealing step performs two functions. On the one hand the annealing transforms the amorphous $4MoO_3 \cdot 6H_2O$ into a more crystalline phase but also serves as a means of burning off the PS microspheres (Figure 3.2c). The honeycomb structure extends across multiple fibers laterally and appears to have infiltrated the interior of the CFP. Since the

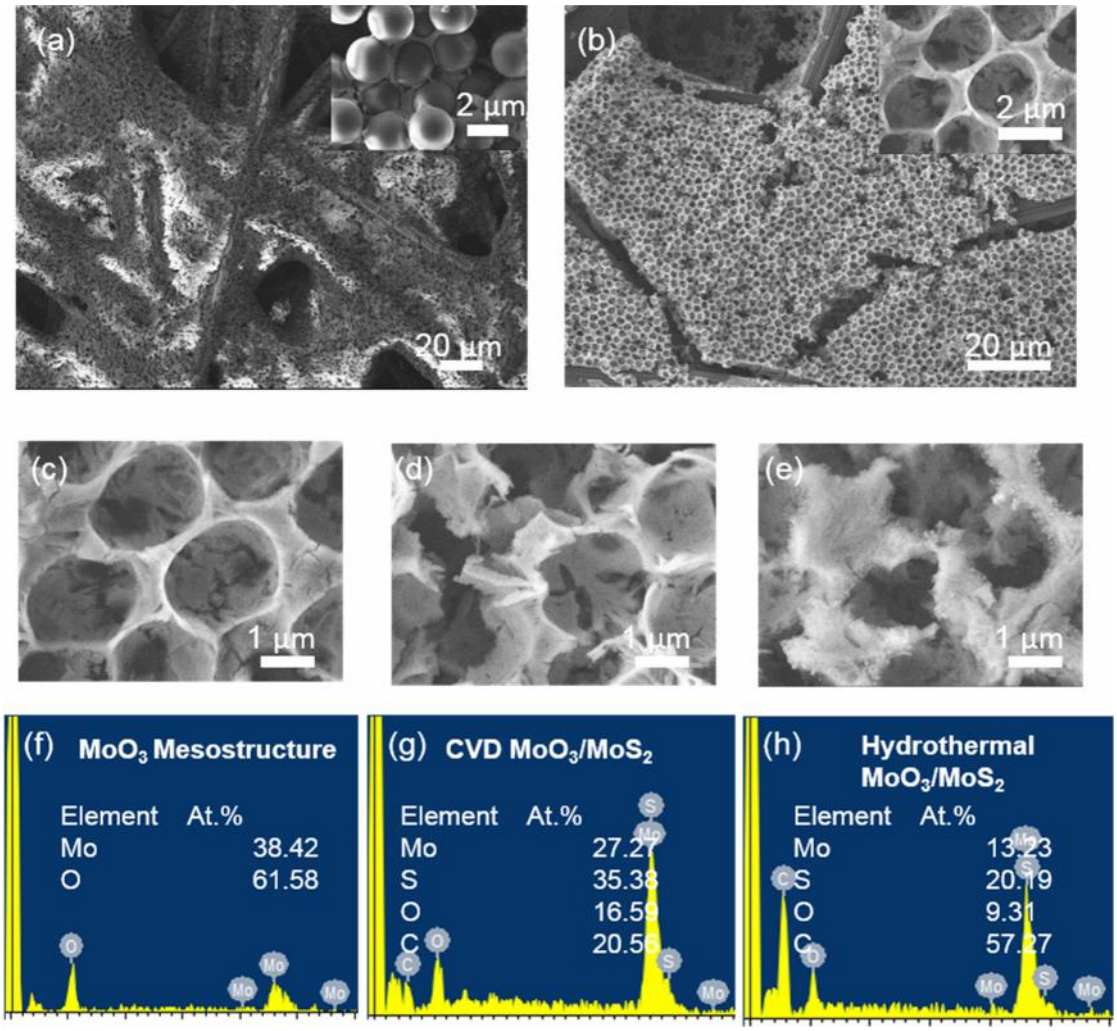


**Figure 3.2.** FE-SEM images of (a) polystyrene sphere/sol gel mixture on carbon fiber paper (CFP) (higher resolution in the inset), (b) after Ar thermal annealing (higher resolution in the inset). (c) $MoO_3$ structure, (d) after chemical vapor deposition sulfurization and (e) after hydrothermal sulfurization. Energy-dispersive X-ray spectroscopy of (f) $MoO_3$ (g) CVD $MoO_3/MoS_2$ and (h) hydrothermal $MoO_3/MoS_2$.

heating is performed in a reducing environment there will be a thin layer of graphitic carbon over top of the $MoO_3$ layer which may act as an electrical path to the CFP during HER. The annealed samples are then placed in a CVD furnace for sulfurization or

hydrothermally sulfurized (HS) by adding the $MoO_3$ samples in a solution of thioacetamide and water.

The morphology difference between the CVD and the HS grown $MoS_2$ is shown in Figure 3.2d, e respectively. The HS sample (Figure 3.2e) has a light, almost fluffy appearance that is very different from the highly crystalline CVD grown sample. The atomic composition was investigated using energy dispersive x-ray spectroscopy within the FE-SEM. The atomic ratios for $MoO_3$ are consistent with what would be expected upon annealing the amorphrous sol-gel precursor. The atomic composition of the CVD grown and hydrothermal sulfurized samples have oxygen present which could be from a number of sources. The carbon fiber substrates were UV-ozoned to make the substrate more hydrophilic so that the polystyrene/sol-gel could infiltrate the fiber more deeply. However it is also possible that there still exists some $MoO_3$ phase below the sulfurized exterior (more evidence will be shown with the Raman data).

To confirm the chemical identity of $MoS_2$ on the CFP Raman spectroscopy was used. $MoS_2$ has two main peaks at ~404 $cm^{-1}$ and 382 $cm^{-1}$ corresponding to the $E_{2g}$ (in plane mode) and $A_{1g}$ mode (out of plane).[4, 21] The Raman spectrum for $MoO_3$, CVD $MoS_2/MoO_3$ and HS $MoS_2$ are shown in Figure 3.3a,b, and c respectively. The CVD $MoS_2/MoO_3$ spectrum is very similar to spectrum $MoO_3$ except for the appearance of the 404 $cm^{-1}$ peak. The expected peak at 382 $cm^{-1}$ is likely obscured by $B_{1g}$ mode at 378 $cm^{-1}$ for $MoO_3$. HS $MoS_2$ has only comparatively weaker peaks at 404 $cm^{-1}$ and 382 $cm^{-1}$ as a result of the amorphous nature of the $MoS_2$. It is possible that there still exists some $MoO_3$

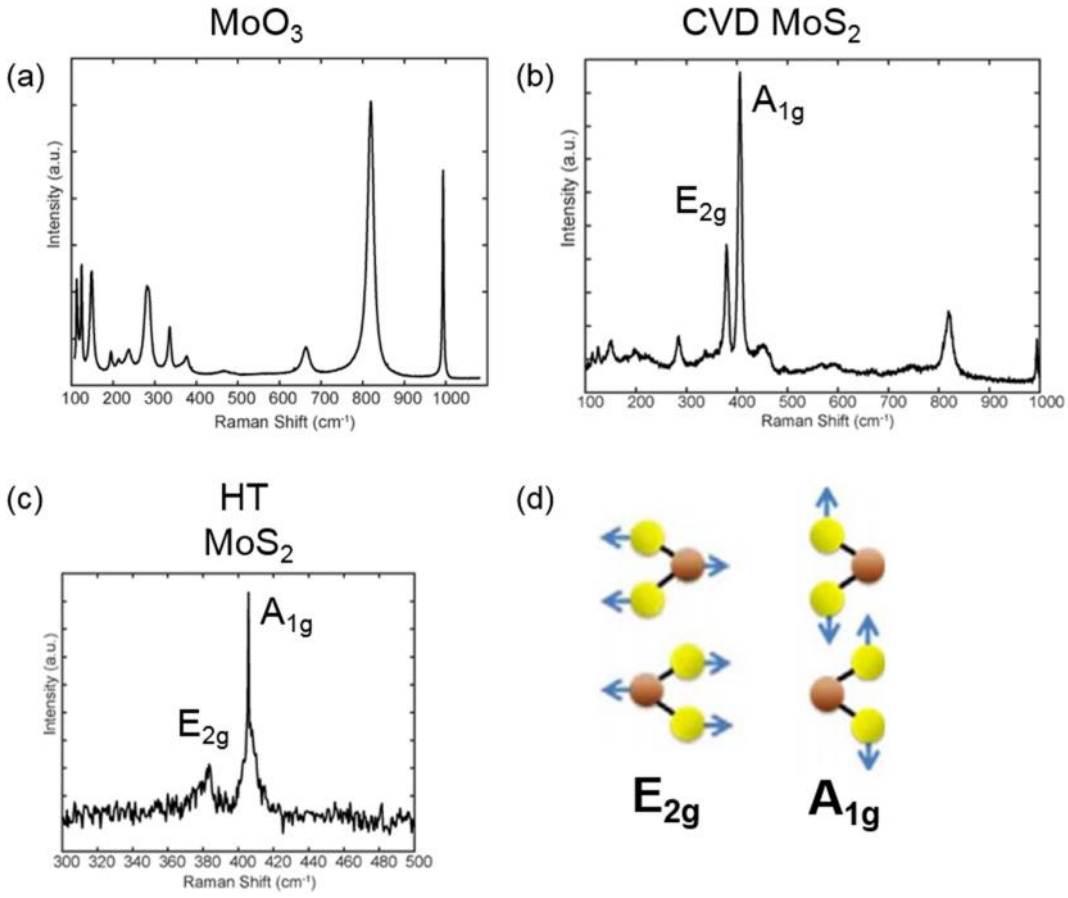


**Figure 3.3.** (a) Raman spectra for $MoO_3$ after annealing under Ar, (b) after sulfurization by chemical vapor deposition (CVD) and (c) hydrothermal sulfurization. (d) Illustration of the out of plane 380 $cm^{-1}$ $E^1_{2g}$ and in plane 402 $cm^{-1}A_{1g}$ vibrational modes.

phase interfacially within the HS $MoS_2$ but the cross section of the $MoO_3$ may be leave the signal to noise ratio to be too low.

The electrocatalytic activity of the CVD grown and hydrothermally grown CFP samples were investigated using the three electrode set-up asshown in Figure 3.4a. One of the metrics used for determining the overall efficiency of HER is based off of the measured potential at 10mA/$cm^2$. The reason for this is economical, since at 10mA/$cm^2$ this is the current density expected for a 12.3% efficient solar to hydrogen device that would be

required for competing with photoelectrochemical water splitting. Figure 3.4b shows the polarization curves (or linear sweep voltamograms (LSV)) for CFP, CVD $MoS_2$ (S1, S2) and HS annealed (S3). These curves are similar to the trends seen in the work from Choi where an optimization procedure was performed using polarization curves based on temperature.[4, 21] The optimal temperature in their work was around 300 $^oC$, in this work 3 hours was found to be optimal for both hydrothermal and CVD growth conditions (there is some evidence to suggest that 12 hours is the optimal temperature but could not be included prior to publishing this dissertation). Comparing the CVD versus the HS polarization curves it is clear that the HS shows better performance. Figure 3.4c shows the polarization curve for the best performing catalyst which have been correct for ohmic loses (iR). The overpotential of 178mV shows that the performance of this catalyst is among some of the best performing to date.[6] The could be a result of the increased surface area provided by the patterning and the thin amorphous shells that likely preferentially expose edge sites that are known to be the center of high catalytic activity.[32] Caution is needed however since much more work is needed in reproduce and identify the reason for this enhanced activity. The Tafel (shown in Figure 3.4d) slope determines the additional voltage required to increase the current by an order of magnitude. Most catalysts are determined by the overpotential necessary to reach the required current density (determined by Tafel slope and the onset potential). Tafel slopes that are small are desirable in general but different catalysts may still have the same onset potential but different Tafel slopes. The Tafel slope may potentially be used to determine the mechanism for hydrogen desorption from the surface. In this case with a Tafel slope

around 46.4 mV/dec might imply a Volmer-Heyrosky mechanism which involves both proton reduction and hydrogen desorption.[6] Work conducted by Parija with $MoS_2$ $MoO_3$ samples were synthesized similarly to what has been reported in this chapter.[33]

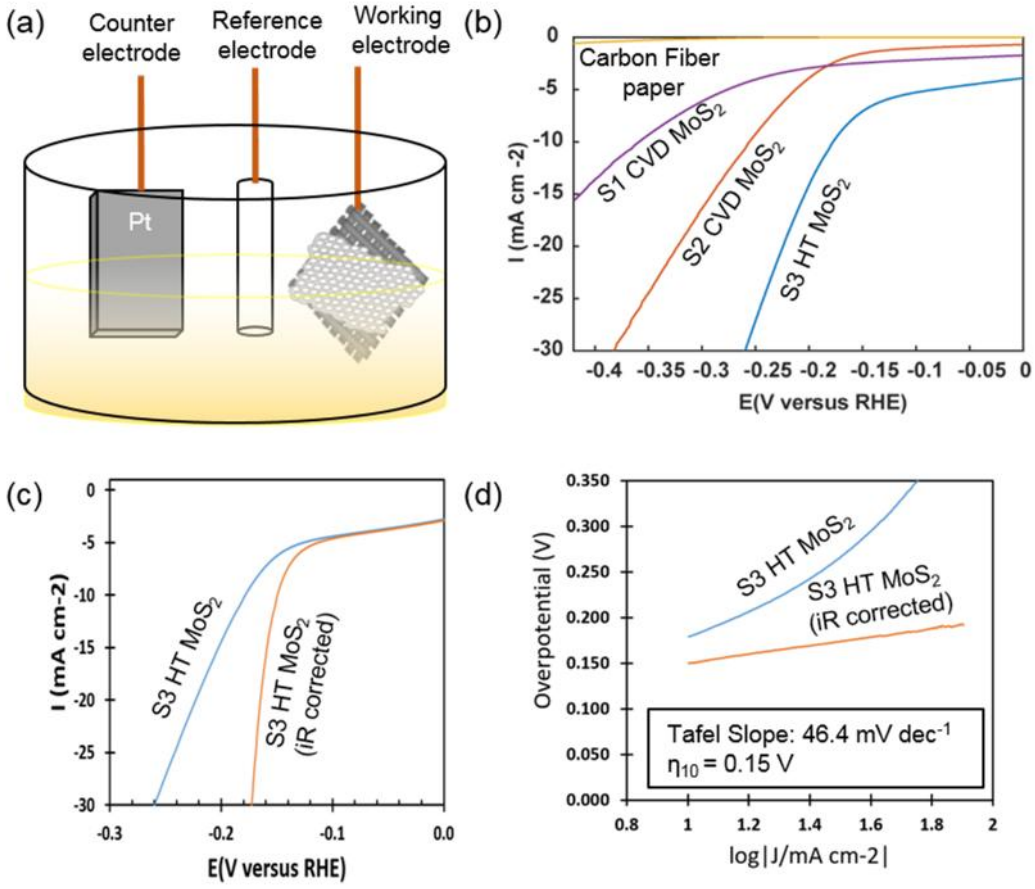


**Figure 3.4** (a) Schematic of the 3 electrode set-up for polarization measurements. (b) Polarization curves for samples carbon fiber paper (CFP) and S1-S3. Polarization curve with iR correction for the best performing catalyst S3. Tafel plot with iR correction for best performing catalyst. HER testing was performed in 0.5 M $H_2SO_4$. Linear sweeping voltammetry scan rate 5 mV/s.

From the EDX and Raman data there appears to exist an $MoO_3$ layer hidden beneath the $MoS_2$, even under the hydrothermally grown materials, which results in

interfacial charge transfer between the $MoO_3$ and $MoS_2$.[33, 34] This could be supported by XPS data which shows peaks at 232.9 eV and 236.1 eV which are derived from the hexavalent Mo in $MoO_3$ and peaks at 229.7 and 232.9 eV which correspond to the $+4<x<+6$ intermediate oxidation states of Mo at the interface between the chalcogenide and oxide layers (in this case oxysulfides). Thus if there are changes in the concentration of Mo, S and O and the degree of hybridization this will affect the energy positioning of the d-states in the Mo. In addition we should expect the $S^{2-}$ 2p level, with doublets being between 161.9-162.1 eV. The spin orbit splitting between the two peaks $Sp_{3/2}$ and $Sp_{1/2}$ is roughly 1.2 eV.

The electronic structure in terms of the conduction and valence bands of the material determines the activity of HER. Hydrogen adsorption is dependent on the states accessible in the conduction band that is the unoccupied states. For $MoS_2$ with hydrogen adsorption the high free energy of adsorption, 1.83 eV, (Figure 3.5 a) by interfacing with $MoO_3$ the conduction band minimum (CBM) is shifted which lowers the free energy of adsorption Figure 3.5b,c respectively . This may be partially the reason that there is an enhancement in the catalytic activity. This is again supported by work with $MoS_{2-x}Se_x$ systems on CFP that saw similar enhancements with HER and OER.[33]

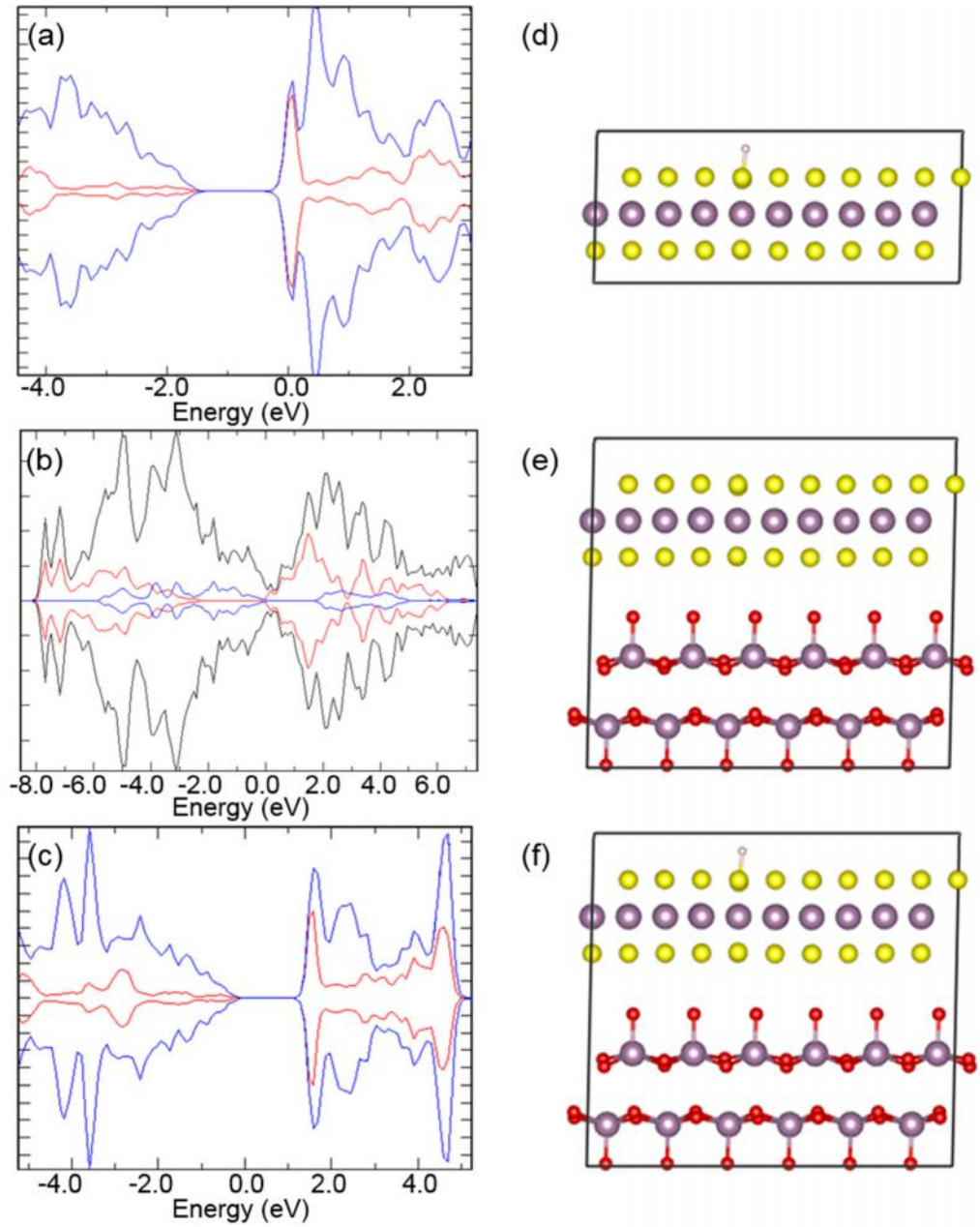


**Figure 3.5.** (a) Partial density of states (DOS) of $MoS_2$ with adsorbed hydrogen (red line) and Sulfur (S) states (blue line). (b) Interfacial DOS of $MoS_2/MoO_3$ with the total DOS (black line, $MoO_3$ (red line) and $MoS_2$ (blue line). (c) Partial density of states of interfacial $MoS_2/MoO_3$ with adsorbed hydrogen (red) and S states (blue). The cells used in the calculations are depicted in d, e, f. The molybdenum and sulfur atoms are represented as violet and yellow spheres respectively.

## 3.4 Conclusion

We have successfully engineered a high surface area high catalytically active sol-gel derived hydrothermal synthesized $MoS_2$ catalyst on CFP. The HER active was found to have an impressive be 178 mV after correcting for the iR drop. There are still many questions regarding the chemical reason for the enhancement and more characterization (XPS, TEM) and electrochemical studies are necessary to correct for electrochemically active surface area, determine the turn over frequency and evaluate the electrochemical impedance spectroscopy. Heterogeneous 2D materials and properly electrode engineering (through patterning) are likely going to play an important role in next generation, cost effective hydrogen evolution catalysts through bandgap engineering.

## 3.5 References

1. Bockris, J. O.; Ammar, I. A.; Huq, A. K. M. S. The Mechanism of the Hydrogen Evolution Reaction on Platinum Silver and Tungsten Surfaces in Acid Solutions. *J Phys Chem-Us* **1957**, *61* (7), 879-886.

2. Parsons, R. Hydrogen Evolution on Platinum Electrodes - the Heats of Activation for the Component Reactions. *T Faraday Soc* **1960,** *56* (9), 1340-1350.

3. Greeley, J.; Jaramillo, T. F.; Bonde, J.; Chorkendorff, I. B.; Norskov, J. K. Computational high-throughput screening of electrocatalytic materials for hydrogen evolution. *Nature Materials* **2006,** *5* (11), 909-913.

4. Choi, Y.-H.; Lee, J.; Parija, A.; Cho, J.; Verkhoturov, S. V.; Al-Hashimi, M.; Fang, L.; Banerjee, S. An in Situ Sulfidation Approach for the Integration of MoS2 Nanosheets

on Carbon Fiber Paper and the Modulation of Its Electrocatalytic Activity by Interfacing with nC60. *ACS Catalysis* **2016,** *6* (9), 6246-6254.

5. Park, S.-K.; Lee, J.; Bong, S.; Jang, B.; Seong, K.-d.; Piao, Y. Scalable Synthesis of Few-Layer MoS2 Incorporated into Hierarchical Porous Carbon Nanosheets for High-Performance Li- and Na-Ion Battery Anodes. *ACS Applied Materials & Interfaces* **2016,** *8* (30), 19456-19465.

6. Benck, J. D.; Hellstern, T. R.; Kibsgaard, J.; Chakthranont, P.; Jaramillo, T. F. Catalyzing the Hydrogen Evolution Reaction (HER) with Molybdenum Sulfide Nanomaterials. *ACS Catalysis* **2014,** *4* (11), 3957-3971.

7. Wu, H. B.; Xia, B. Y.; Yu, L.; Yu, X.-Y.; Lou, X. W. Porous molybdenum carbide nano-octahedrons synthesized via confined carburization in metal-organic frameworks for efficient hydrogen production. *Nat Commun* **2015,** *6*, 6512.

8. Ma, R. G.; Zhou, Y.; Chen, Y. F.; Li, P. X.; Liu, Q.; Wang, J. C. Ultrafine Molybdenum Carbide Nanoparticles Composited with Carbon as a Highly Active Hydrogen-Evolution Electrocatalyst. *Angew Chem Int Edit* **2015,** *54* (49), 14723-14727.

9. Lin, H. L.; Shi, Z. P.; He, S. N.; Yu, X.; Wang, S. N.; Gao, Q. S.; Tang, Y. Heteronanowires of MoC-Mo2C as efficient electrocatalysts for hydrogen evolution reaction. *Chem Sci* **2016,** *7* (5), 3399-3405.

10. Kibsgaard, J.; Jaramillo, T. F. Molybdenum Phosphosulfide: An Active, Acid-Stable, Earth-Abundant Catalyst for the Hydrogen Evolution Reaction. *Angew Chem Int Edit* **2014,** *53* (52), 14433-14437.

11. Shi, Y.; Zhang, B. Recent advances in transition metal phosphide nanomaterials: synthesis and applications in hydrogen evolution reaction. *Chemical Society Reviews* **2016,** *45* (6), 1529-1541.

12. Zhang, X.; Yu, X.; Zhang, L.; Zhou, F.; Liang, Y.; Wang, R. Molybdenum Phosphide/Carbon Nanotube Hybrids as pH-Universal Electrocatalysts for Hydrogen Evolution Reaction. *Advanced Functional Materials* **2018,** *28* (16), 1706523.

13. Byskov, L. S.; Bollinger, M.; Nørskov, J. K.; Clausen, B. S.; Topsøe, H. Molecular aspects of the H2 activation on MoS2 based catalysts — the role of dynamic surface arrangements. *Journal of Molecular Catalysis A: Chemical* **2000,** *163* (1), 117-122.

14. Hinnemann, B.; Moses, P. G.; Bonde, J.; Jorgensen, K. P.; Nielsen, J. H.; Horch, S.; Chorkendorff, I.; Norskov, J. K. Biornimetic hydrogen evolution: MoS2 nanoparticles as catalyst for hydrogen evolution. *Journal of the American Chemical Society* **2005,** *127* (15), 5308-5309.

15. Skrabalak, S. E.; Suslick, K. S. Porous MoS2 Synthesized by Ultrasonic Spray Pyrolysis. *Journal of the American Chemical Society* **2005,** *127* (28), 9990-9991.

16. Kibsgaard, J.; Chen, Z.; Reinecke, B. N.; Jaramillo, T. F. Engineering the surface structure of MoS2 to preferentially expose active edge sites for electrocatalysis. *Nature Materials* **2012,** *11*, 963.

17. Deng, J.; Li, H. B.; Wang, S. H.; Ding, D.; Chen, M. S.; Liu, C.; Tian, Z. Q.; Novoselov, K. S.; Ma, C.; Deng, D. H.; Bao, X. H. Multiscale structural and electronic control of molybdenum disulfide foam for highly efficient hydrogen production. *Nat Commun* **2017,** *8*.

18. Song, J.-S.; Winnik, M. A. Cross-Linked, Monodisperse, Micron-Sized Polystyrene Particles by Two-Stage Dispersion Polymerization. *Macromolecules* **2005,** *38* (20), 8300-8307.

19. Li, F.; Geng, C.; Yan, Q. Growth Kinetics of Monodisperse Polystyrene Microspheres Prepared by Dispersion Polymerization. *Journal of Polymers* **2013,** *2013*, 7.

20. Zheng, W.; Lin, J.; Feng, W.; Xiao, K.; Qiu, Y.; Chen, X.; Liu, G.; Cao, W.; Pantelides, S. T.; Zhou, W.; Hu, P. Patterned Growth of P-Type MoS2 Atomic Layers Using Sol–Gel as Precursor. *Advanced Functional Materials* **2016,** *26* (35), 6371-6379.

21. Choi, Y.-H.; Cho, J.; Lunsford, A. M.; Al-Hashimi, M.; Fang, L.; Banerjee, S. Mapping the electrocatalytic activity of MoS2 across its amorphous to crystalline transition. *Journal of Materials Chemistry A* **2017,** *5* (10), 5129-5141.

22. Guo, Y. N.; Tang, J.; Qian, H. Y.; Wang, Z. L.; Yamauchi, Y. One-Pot Synthesis of Zeolitic Imidazolate Framework 67-Derived Hollow Co3S4@MoS2 Heterostructures as Efficient Bifunctional Catalysts. *Chemistry of Materials* **2017,** *29* (13), 5566-5573.

23. Kohn, W.; Sham, L. J. Self-Consistent Equations Including Exchange and Correlation Effects. *Physical Review* **1965,** *140* (4A), A1133-A1138.

24. Kresse, G. Ab initio molecular dynamics for liquid metals. *Journal of Non-Crystalline Solids* **1995,** *192-193*, 222-229.

25. Kresse, G.; Furthmüller, J. Efficiency of ab-initio total energy calculations for metals and semiconductors using a plane-wave basis set. *Computational Materials Science* **1996,** *6* (1), 15-50.

26. Perdew, J. P.; Burke, K.; Ernzerhof, M. Generalized Gradient Approximation Made Simple. *Physical Review Letters* **1996,** *77* (18), 3865-3868.

27. Kresse, G.; Joubert, D. From ultrasoft pseudopotentials to the projector augmented-wave method. *Physical Review B* **1999,** *59* (3), 1758-1775.

28. Dudarev, S. L.; Botton, G. A.; Savrasov, S. Y.; Humphreys, C. J.; Sutton, A. P. Electron-energy-loss spectra and the structural stability of nickel oxide: An LSDA+U study. *Physical Review B* **1998,** *57* (3), 1505-1509.

29. Li, H.; Yu, K.; Tang, Z.; Fu, H.; Zhu, Z. High photocatalytic performance of a type-II α-MoO3@MoS2 heterojunction: from theory to experiment. *Physical Chemistry Chemical Physics* **2016,** *18* (20), 14074-14085.

30. Grimme, S. Accurate description of van der Waals complexes by density functional theory including empirical corrections. *Journal of Computational Chemistry* **2004,** *25* (12), 1463-1473.

31. McEvoy, T. M.; Stevenson, K. J. Electrochemical quartz crystal microbalance study of the electrodeposition mechanism of molybdenum oxide thin films from peroxo-polymolybdate solution. *Analytica Chimica Acta* **2003,** *496* (1), 39-51.

32. Benck, J. D.; Chen, Z.; Kuritzky, L. Y.; Forman, A. J.; Jaramillo, T. F. Amorphous Molybdenum Sulfide Catalysts for Electrochemical Hydrogen Production: Insights into the Origin of their Catalytic Activity. *ACS Catalysis* **2012,** *2* (9), 1916-1923.

33. Parija, A. Design of Low-Dimensional Materials for Energy Storage, Computing, and Catalysis Based on Electronic Structure Considerations. Ph.D., Texas A&M University **2019**.

34. Chen, Z.; Cummins, D.; Reinecke, B. N.; Clark, E.; Sunkara, M. K.; Jaramillo, T. F. Core–shell MoO3–MoS2 Nanowires for Hydrogen Evolution: A Functional Design for Electrocatalytic Materials. *Nano Letters* **2011,** *11* (10), 4168-4175.

# CHAPTER IV

# ELECTRICAL PROPERTIES OF TCPP NANOWIRES INVESTIGATED BY CONDUCTIVE PROBE AFM

## 4.1 Introduction

Self-assembled porphyriniod materials have enormous potential in energy conversion applications such as photovoltaics,[1, 2] memory materials,[3, 4] catalysis,[5, 6] and sensing. In nature, aggregation of biologically relevant molecules, such as chlorosomes, exist in green bacteria where the geometry of the aggregates reflect a tubular assembly. Artificial photosynthesis is a very active field of research aiming to understand how the structure and function of the aggregated photosensitive materials affect the light harvesting and charge transport efficiency. There are a number of ways to assemble porphyrins into hierarchical structures such as through metal ligand interactions, surface assisted vapor deposition, surfactant assisted and ionic assembly. Ionic assembly is a simple and effective way to study the various fundamental optical and electrical properties of aggregated porphyrin structures.

A large body of work exists studying the ionic assembly of tetra(p-sulfonatophenyl)porphyrin (TSPP). Much of the earlier work focused on the relationship between the morphology and the optical properties of the free-base, diacid and aggregates.[7, 8, 9] It was not until scanning tunneling microscopy (STM),[10, 11] diffraction,[12] and cryo-transmission electron microscopy(TEM)[13] techniques were utilized that additional insight into the internal structure was realized. It appeared, at least for TSPP, that the nanowires were likely a multi-helical nanotube where the diameter is 15-20 nm

and a wall width of 1.5-2 nm.[1] The major J band (stacking arrangement where the molecules are oriented head to tail) is polarized parallel to the tube axis and the H band (stacking arrangement where the molecules are oriented face-face) is perpendicular, which agrees with the linear dichroism studies. Electronic and photo-electronic information on the TSPP nanowires have been studied using scanning tunneling microscopy (STM) (for the electronic gap states) as well as the use of metal interdigitated electrodes (studying the photo generated currents).[14, 15, 16] From the scanning tunneling spectroscopy (STS) of TSPP on Au(111) the onset of conductivity happens at a higher energy than the monomer that may reflect a shift in the energy associated within the noncovalent interactions. Electroluminescence studies of the TSPP wires showed that the tubular J aggregates are not only decoupled from the Au(111) substrate but also generate excitons as a result of the strong dipole coupling in ordered assembly.[17] All this recent work provides an interesting fundamental look at how morphology relates to electronic structure and thus electrical and optical properties of the crystalline porphyrin aggregates.

Tetra(p-carboxyphenyl)porphyrin (TCPP) is a molecule similar in chemical structure to TSPP and also forms ionic nanowires in aqueous acidic solutions. Whereas there is a lot body of literature on the assembly and electrical properties of TSPP, there are very few works that aim at understanding these properties of TCPP aggregates.[18, 19] Other work that has been done with TCPP has been with dye-sensitized solar cells where aggregation can be a disadvantage.[2] Aggregation in this way, i.e. random, cannot be used because of a process called concentration quenching.[20] Thus organizing the aggregates in a way that removes trap states is advantageous for energy harvesting applications. The

acidification of TCPP in ethanol as well as aqueous $HNO_3$ and HCl have been studied in some detail.[21, 22] It is known that the TCPP aggregates are kinetically unstable in aqueous acidic conditions prompting the use of stabilizing agents such as poly (vinyl alcohol).[22]To date there has been no electrical characterization of TCPP aggregates.

In this work we hope to understand the morphology and the electrical properties of TCPP nanostructures at pH values below 1 on Au(111) using scanning probe microscopy. Typically, the condition for performing electrical measurements is that the AFM tip be placed in contact mode. We show the AFM tip slowly removes material from the nanowire, even at low imaging loads. Therefore a new strategy for locating the nanowires and measuring their electrical properties is proposed.

## 4.2 Experimental Methods

Tetra(*p*-carboxyphenyl)porphyrin (>97%) (TCPP) was purchased from Frontier Scientific Inc. The sample was used without further purification. High purity water (18.2 MΩ·cm, NANOpure Diamond, Barnstead) was used in this study. Ammonium hydroxide (29%) and hydrochloric acid (37%) were purchased from EMD Chemicals Inc. Double side polished silicon substrates (Cz, 368 µm, P doped) were purchased from Virginia Semiconductor. 200 nm thick, flame annealed, Au(111) films on mica (Phasis) were used for all conductive probe measurements.

Silicon wafers were cleaned using an acid piranha solution of 3:1 (v/v) ratio of $H_2SO_4$ to $H_2O_2$ for 15 mins. The wafers were rinsed sequentially with 18.2 MΩ·cm water, ethanol and dried with streaming $N_2$. Au(111) was cleaned by the following procedure:

the sample was UV-ozone irradiated for 10 mins, washed with copious amounts of 18.2 MΩ·cm water, ethanol, and dried with streaming $N_2$.

Porphyrin nanostructures were formed through a modified ionic assembly through an acidification procedure.[22] TCPP monomers were dissolved in 0.2 M $NH_4OH$ then titrated with 1M HCl until the appropriate pH was reached for forming the various structures. Materials were then static spincasted onto either 300 nm $SiO_2$ on Si(100) or Au(111).

**Optical Characterization:** The absorption spectra of the TCPP anions in $NH_4OH$ and acidic solutions were obtained using an ocean optics UV-Vis spectrometer.

**Morphological characterization:** Scanning Electron Microscopy (SEM, JEOL JSM 7500F) was utilized to provide a detailed look at the overall morphology of the wires. These analyzed samples were prepared by drop-casting TCPP wires onto Si(100) substrates. TCPP assemblies on 300 nm $SiO_2$ were characterized in tapping mode using an Alpha 300 WiTec Atomic Force Microscope (AFM). Nanowires that were spincasted on Au(111) were imaged using an Asylum MFP3D in tapping mode and contact mode. For general imaging in tapping mode silicon tips with nominal radii of 8 nm, 40N/m and 170 kHz resonance frequency were used.

**Electrical characterization of Nanowires:** The electrical characterization of the nanowires was performed with a modified Asylum MFP3D AFM holder and an RHK $10^8$ gain transimpedance amplifier powered through a RHK controller (version 8). The signal for the amplifier was routed from the RHK controller to the Asylum Arc2 controller for input. Biasing was accomplished through the Arc 2 controller to the sample. All metal

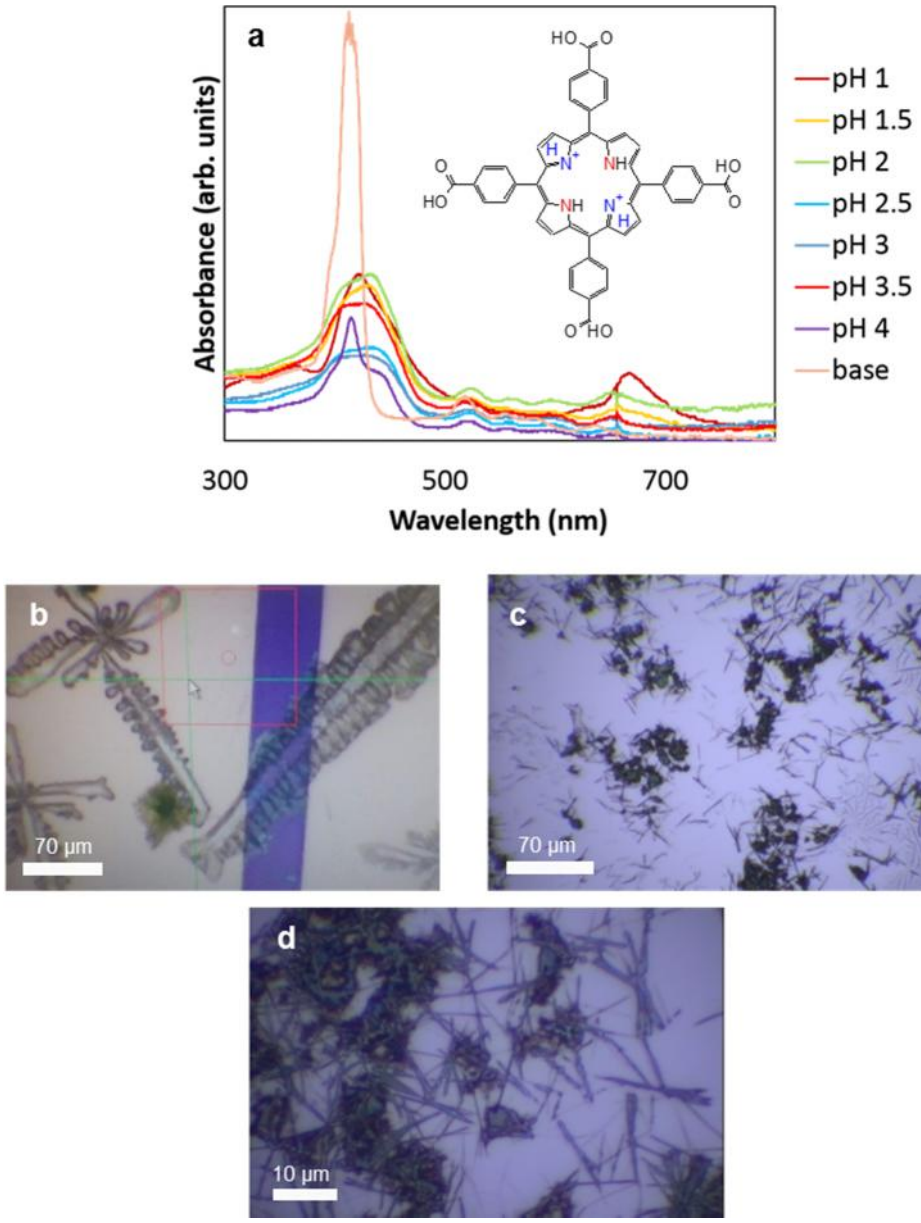


**Figure 4.1.** UV-vis spectra (a) of TCPP at different pH values showing the red shift of soret band and collapse of the Q bands at around pH 1. (b) Optical image of $NH_4Cl$ crystals on gold coated silicon substrates after dropcasting. Optical image, 20x (c) of TCPP nanowires and 100x (d)

platinum probes from Rocky Mountain Probes with a nominal radii of 20 nm and a 0.8 N/m spring constant (9kHz resonant frequency) were used for all conductive

measurements. The voltages applied varied from ±100 mV for Au(111) and ±3 volts for TCPP wires on Au(111).

### 4.3 Results and Discussion

The TCPP nanowires were made through a simple modification of an acidification procedure developed in McHaedes group.[22] Rather than using a polyvinyl stabilizer the TCPP starting material was first dissolved in $NH_4OH$ giving a precursor with a pH greater than 10. The $pK_a$ of the TCPP monomer is known to be approximately 5, which means that the carboxylic acid groups will be completely protonated. The precursor solution was titrated slowly with 0.1 M HCl until the pH of the solution was approximately 1. Figure 4.1a shows the UV-vis absorption spectrum of the TCPP precursor at different pH values. There exist three different unique peaks in the UV absorbance that help provide insight into the morphological characteristics of the TCPP assemblies. It has been shown that around a pH of 5 the TCPP forms a cationic $H_2TCPP^{2+}$.[21] At a pH just above 1 the soret band is split, with the origin of this split is not quite understood. It is possible that the arrangement of the species could be a dimer structure of two porphyrins mutually perpendicular to each other. It is also likely that there could be overlapping spectra of different species of aggregates and non-aggregates. At pH values below 1 aggregates form, the aggregates optical properties are counter-ion dependent.[21]

For further morphological characterization, the TCPP aggregates were then spincasted onto either Si(100) with 300 nm oxide layer or Au(111). A slight digression is in order to help better understand the need to spin cast the material versus using other

techniques such as drop cast or soaking. One unfortunate consequence of using ionic assembly for creating the TCPP aggregates is that salts will form on the surface once the

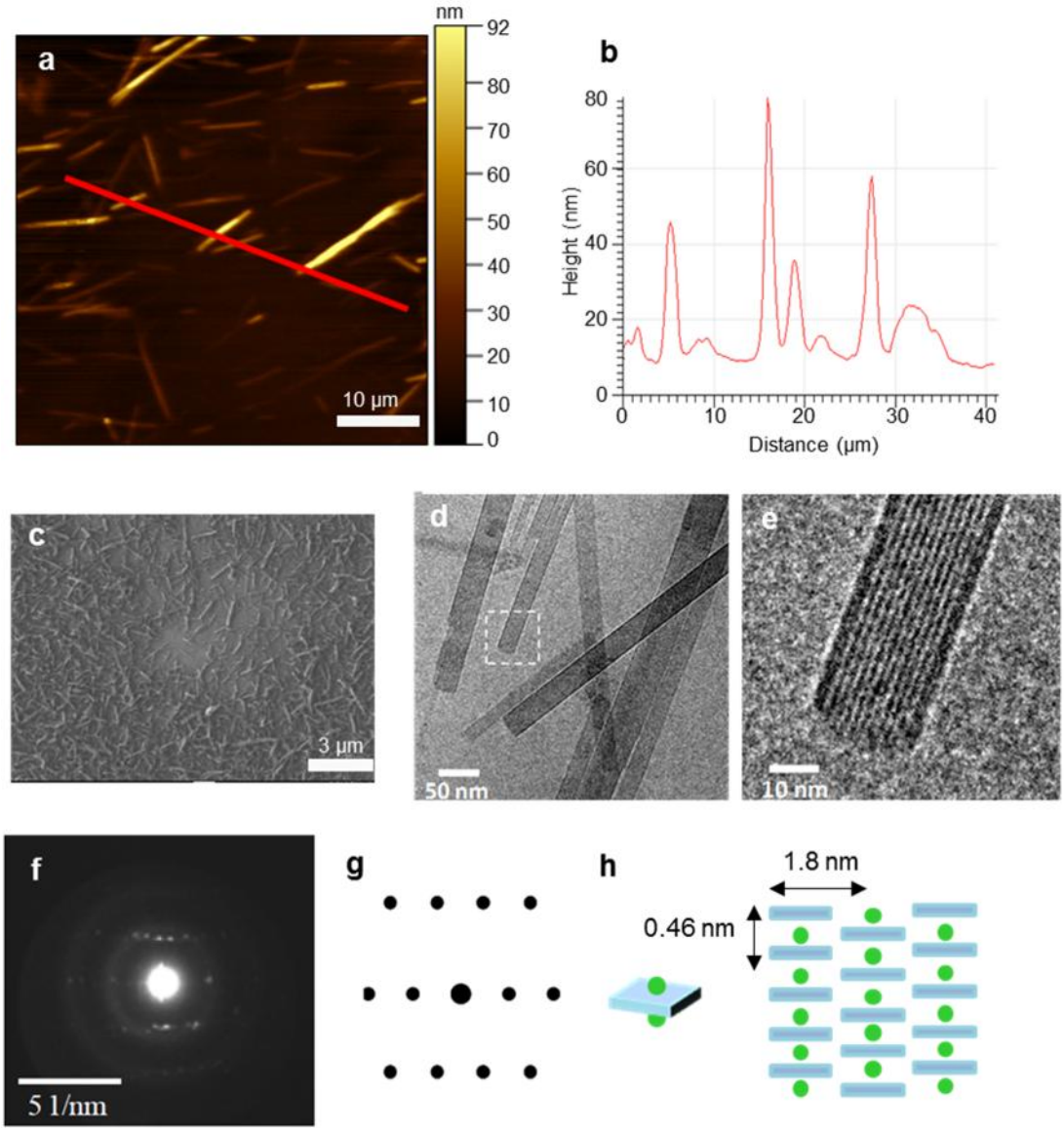


**Figure 4.2.** AFM images of (a) TCPP nanowires on $SiO_2$ and (b) cross section of (a). (c) SEM of TCPP nanowires on $SiO_2$, (d) cryo-TEM of TCPP nanowires, and(e) higher resolution cryoTEM.(f) Electron diffraction pattern with (g) the geometry of reflections, (h) a model of TCPP brick-like arrangement. Adapted with permission from Albert Wan.[23] Copyright 2011 by Albert Wan.

solution has dried. Figure 4.1b shows the fractal crystal patterns of $NH_4OH$ that cover most of the surface. If spincasting is not possible dropcasting can still be used as a deposition method however, the solution depositedon the surface needs to be blown dry with nitrogen (after a few mins of sitting on the surface) and new clean 0.1M HCl should be drop casted on the surface again and blown dry after 5 mins of settling of the surface.

Figures 4.1c,d show the TCPP nanowires that were formed at a pH around 1. The optical contrast of these wires are very pronounced, with wires with diameters down to several nanometers being resolved by the 100x objective. The morphological properties of the TCPP nanowires were explored using AFM, SEM and CryoTEM. Figure 4.2a shows an AFM topography image of the nanowires spin casted onto 300 nm $SiO_2$ substrates. The AFM cross section (Figure4.2b) and the SEM (Figure 4.2c) show that the wires vary in height, with some of the diameters reaching several hundred nanometers in thickness. This large thickness is a result of the smaller wires aggregating together to form bundles. The sizes of these smaller units are found to be around 2nm, which are roughly the sizes of the "nanoplates" observed previously.[23] Figure 4.2d,e is the cyroTEM of the TCPP nanowires giving some insight into the width of the wires, which appear to vary from less than 10 nm up to about 50 nm.[23] The lattice spacing was measured to be approximately 1.8 nm. Electron diffraction pattern (Figure 4.2f,g) supports this measurement of the lattice spacing along with a secondary spacing measured at 0.46 nm. Figure 4.2h shows a cartoon model of the TCCP assembly based on the TEM data where the 1.8 nm is the spacing across the width of the wire (the dark lines running along the long axis of the wire) and the 0.46 nm are likely the stacking distance between each of the porphyrins. Interestingly

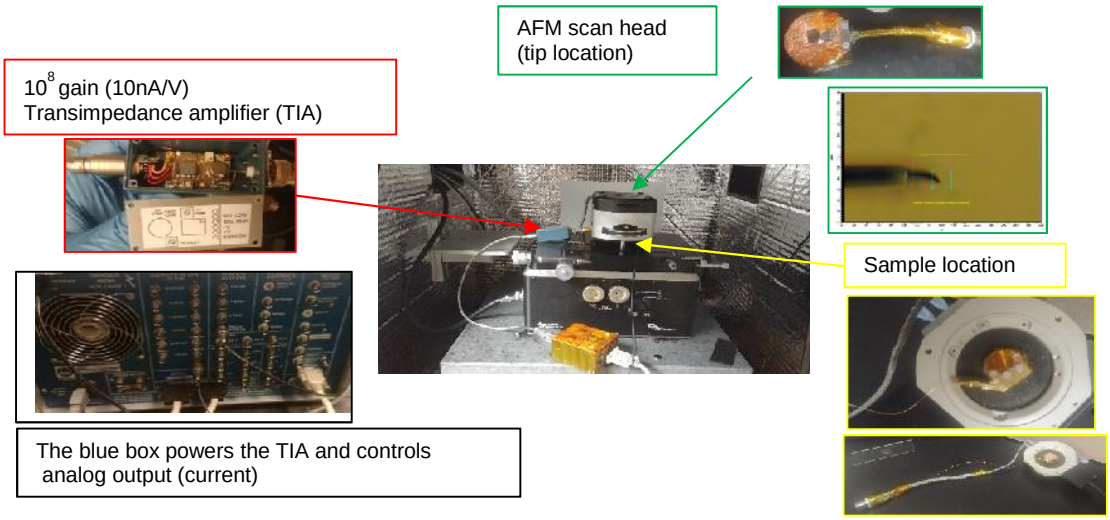


**Figure 4.3.** Modified commercial AFM for performing low noise conductive probe.

the 1.8 nm spacing is consistent with STM data of TCPP monomers organized on HOPG surfaces through hydrogen bonding.[24] Additional studies are looking into the transition from nanoplates to nanowires.Preliminary data suggests that the nanoplatelets, described by Albert Wan, are likely seeds for the growth of the nanowires as the pH decreases.[23]

The electrical properties of the TCPP wires were investigated using conductive probe. Figure 4.3 shows a commercial AFM (Asylum MFP 3D) that has been adapted for performing low noise conductive probe. The PEEK (polyether ether ketone) holder has been modified such that a homemade BNC cable is held in place via a piece of stainless sheet metal. The entire holder is covered in high purity copper foil and held in place with double sided kapton tape. The sheet metal makes mechanical and thus electrical contact with the shield of the cable and when the nylon screws are tighten provide a low impedance connection to ground. The signal wire is made of 38 gauge kapton coated copper wire that has been stripped at the end to allow the electrical connection to any AFM

chip (which has the cantilever). It is very important that the wire not have a great deal of strain because mechanical fluctuations can induce spurious current signals as seen in the power spectral density. The current from the tip is measured (the tip is held at virtual ground) using an RHK IVP-200 10nA/V transimpedance amplifier, which is powered by a revision 8 SPM100 controller. This was used because the current range was from 1pA to 100 nA, providing very large dynamic range and high bandwidth for obtaining current maps and obtaining IV curves. The sample holder will be discussed in more detail in chapter 5 but briefly the holder is a modified heating stage that provides the biasing capability to the sample. Biasing is comes from the Arc2 controller output, in the software the "BNC out1" was changed to OutC, which routes the biasing from the controller to the output. A full analysis of the current noise floor as well as the signal routing will be discussed in Chapter 5 when thermoelectric voltage will be discussed.

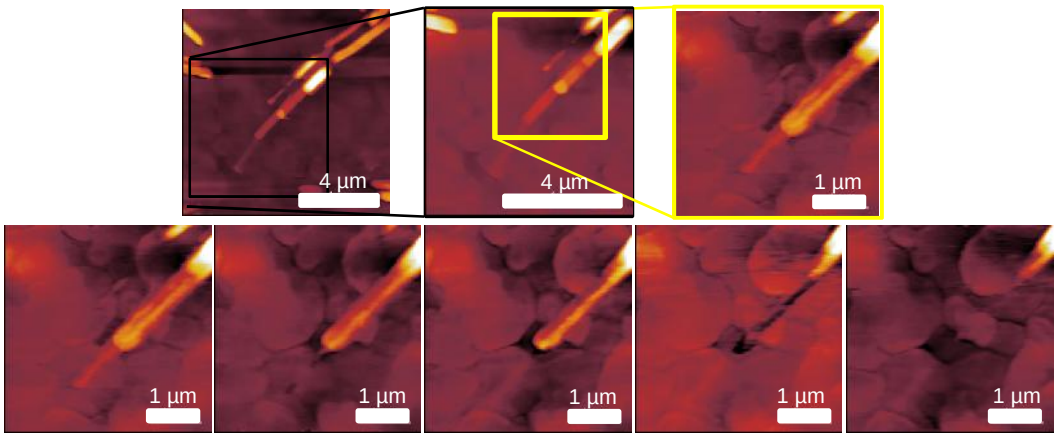


**Figure 4.4.** AFM image (topography) showing how, with continued scanning in contact mode, the TCPP wires are pushed away.

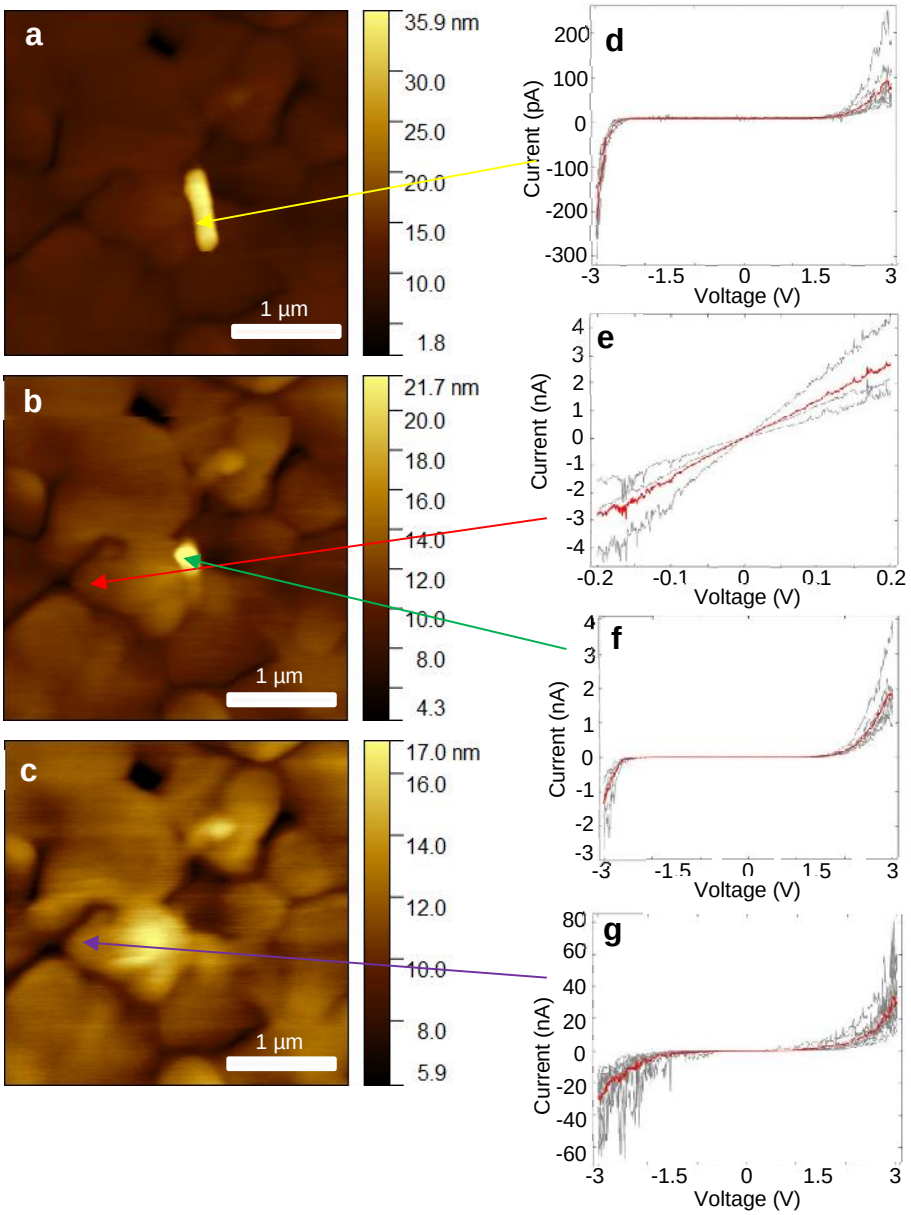


**Figure 4.5.** (a) AFM Topography of 20 nm TCPP nanowire, (b) after one scan, (c) after 2 scans. (d) IV curve on nanowire (yellow arrow), red curve is average. (e) IV curve on gold(red arrow) as a check of tip quality, (f) IV curve back on wire(green arrow), (g) IV curve on bare gold(purple arrow) suggesting either the tip or sample has TCPP residue.

Conductive probe is typically performed in contact mode which, for soft materials, the shear stresses can cause destruction of the material. Figure 4.4 displays the images

showing the morphological change of the wires upon continued scanning. The spring constant of the probes were 0.8 N/m with the applied load estimated around 10 nN. It is clear the wires cannot sustain continued contact mode scanning. It is worth noting the interesting structures of the wires on Au(111). The wires appear in a step wire formation with height variations between 5-15 nm in variations in some areas. As the wires are slowly pushed out of the scan area the interior of some of the wires have what appears to be a divot that has a height of approximately 2.5-5 nm in height. This could be the height of the clusters of the assembled monomeric units. As explained earlier the lattice structure was found to be approximately 1.8 nm suggesting that these wires are likely stacking on top of each other in a brick layer pattern. What is curious again is the divot, which stays in the image even after 2 or 3 scans, and if hollow structure on the inside suggests anything about how the wires are forming? While it is possible that the inside of some of the fibers are hollow, similar to what has been seen with TSPP nanofibers, more work is needed to understand the morphology of the wires.

The preliminary conductive probe data is presented in Figure 5. Figure 5a shows a TCPP wire that is approximately 20 nm in height, 750 nm in length and 212 nm wide. After successive images Figure 5b the wire is gone (as shown in Figure 4.5c). Figure 4.5d shows 10 IV curves, with the voltage swept from -3 to 3 V, that were taken at low loads on the wire, followed by on the gold (where the voltage was limited to -0.1 to 0.1 V) to show that the tip did not have the wire stuck to it (as shown in Figure 5e), then back on the wire (Figure 4.5f). The semiconducting nature of the wire is obvious from its shape with what appears to be the electronic bandgap in the IV curve, it is interesting to see how

dramatic the IV changes in the negative axis versus the positive. The transition voltages for all the curves had values being approximately 1.3 and -2.2V, giving a gap of 3.5 V.

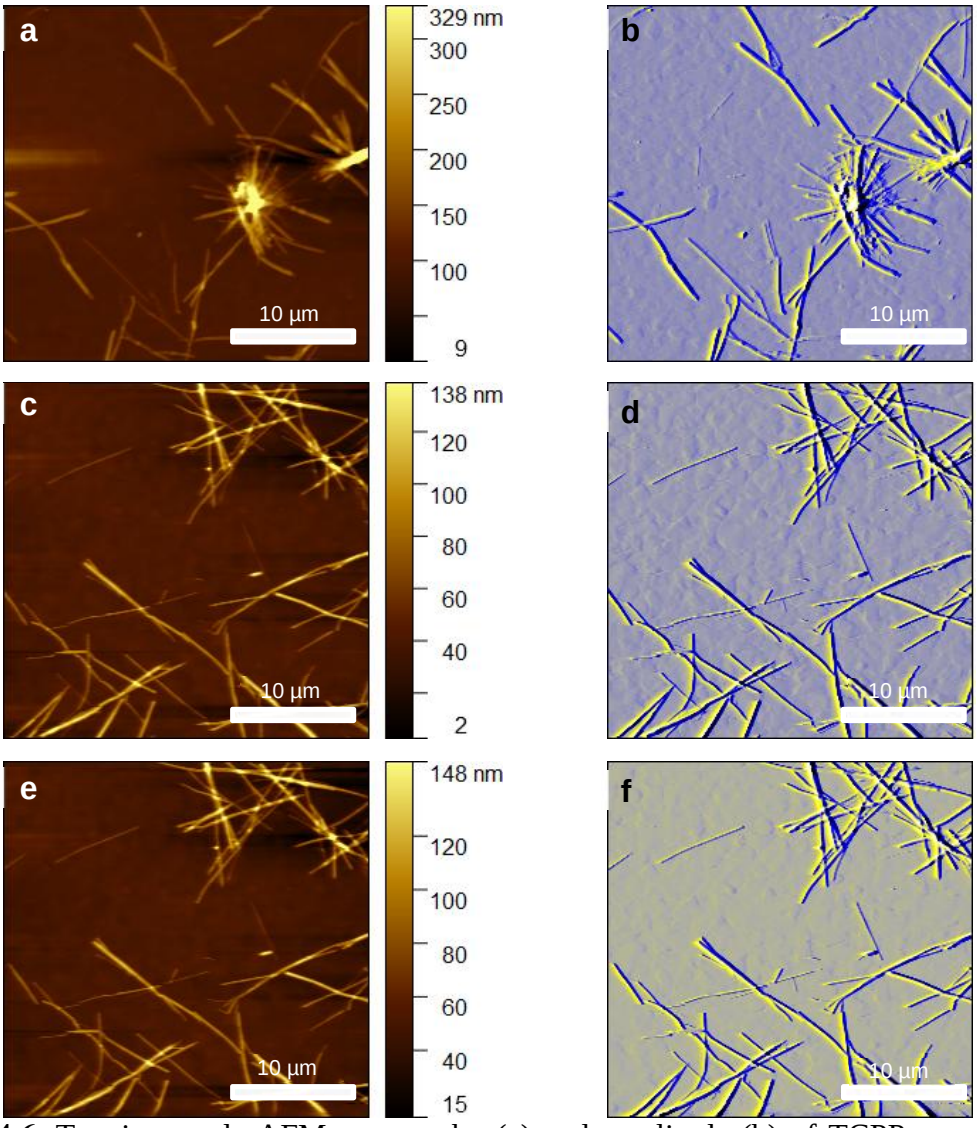


**Figure 4.6.** Tapping mode AFM topography (a) and amplitude (b) of TCPP nanowire "teepee" demonstrating the efficacy of the experiment. Tapping mode AFM Topography(c) and (d) amplitude of TCPP nanowires. Tapping mode AFM topography (e) and (f) amplitude after four consecutive scans.

The transition voltages are similar to work with TSPP nanowires performed with STS where the positive onset was 0.8 V and the negative -1.9 V giving a gap of 2.7 V. Figure 4.5g shows an IV curve that appears to have a very noisy signal but still somewhat semiconducting. Unfortunately this curve was taken on the gold sample which implies either a thin layer of the TCPP material is stuck to the tip or there is a thin layer of porphyrin on the gold surface that is not easily seen.

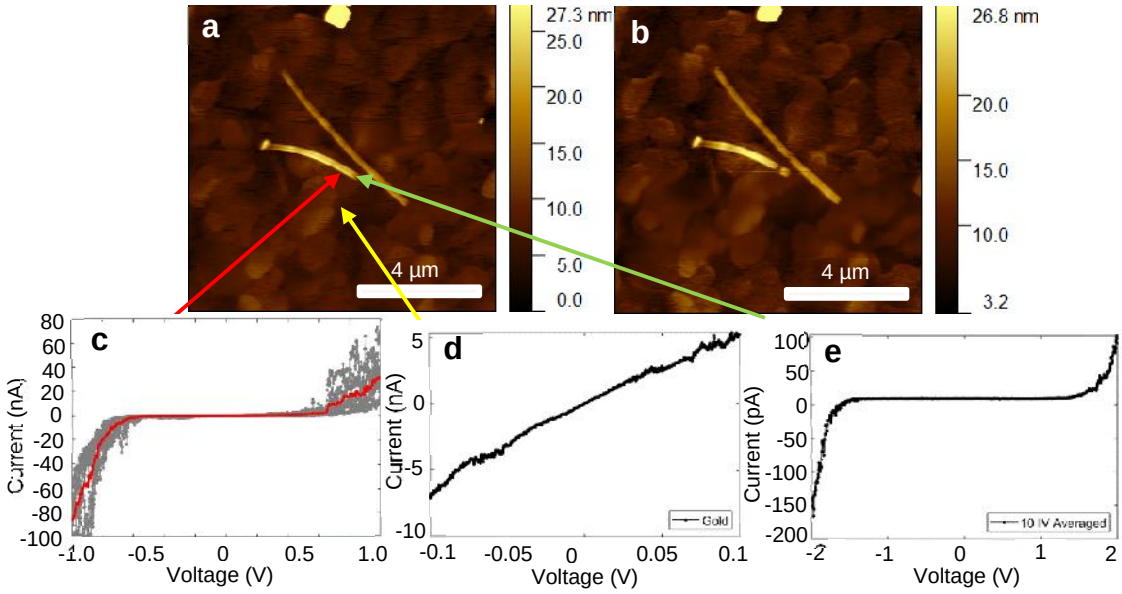


**Figure 4.7.** Tapping mode AFM topography before (a) and after (b) IV curves. (c) Shows the IV curve on nanowire with large current running through the material. IV curve of Au(111) (d) and on the wire (e) adjacent to the area that had large current running through material.

Since contact mode was damaging the delicate TCPP wires the idea of switching from tapping mode for imaging then contact mode was conceived. The idea involves taking an image in tapping mode, move the tip away, switch to contact mode, then landing

the tip in the same spot. The requirements necessary for the experiment to work properly are steep. The microscope must be stable enough that when switching to the alternate mode the sample (or tip depending on the coarse approach mechanism) needs to be in the same place. The MFP-3D is a closed loop AFM with a very ridged frame and can be well insulated within the closed environmental enclosure to keep the thermal drift at a minimum. Initial tests were performed to ensure that the TCPP nanowires could be imaged with lower spring constant levers in tapping mode. Figure 4.6a shows the results of scanning over a nanowire "teepee", a structure that can only be imaged in tapping mode as the result of minimal shear forces acting on the structure. What is interesting is the amplitude signal is very sensitive revealing smaller nanowire structures that are hard to resolve in topography. Usually in tapping mode the phase signal is used when imaging delicate samples since it provides qualitative information on the viscoelastic properties of the sample however since the resonant frequency of the cantilevers are low the phase image is not very stable (albeit still can obtain a decent image). Figure 4.6c,d shows the initial image of nanowires and Figure 6e,f after consecutively scanning in the same area in tapping mode. The four images took approximately 1 hour to obtain with both images appearing to overlap one another suggesting minimal effects of drift. The next thing to check was (after moving the tip away and switching from tapping to contact mode) whether the tip will be in the area designated by the cursor in the software. For many AFM set ups (i.e. Bruker Multimode, Agilent 5500) moving away from the surface can lead to a significant shift from the last position in the scan. This is likely to do with the use of stepper motors for the coarse approach that can displace from the last position by over 1

micron or more. Figure 4.7a,b shows images of a 15 nm nanowire before and after obtaining IV data respectively. The first IV curve (Figure 4.7c) had a large current density than what has ever been observed with sweeping bias on the nanowires. The current range in the averaged IV is -90 nA – 40 nA. Although the shape of the IV is similar to the other curves taken previously the voltage range is much smaller. The tip was moved to an area on gold to make sure that the tip was not contaminated, Figure 4.7d shows the IV curve which is roughly linear suggesting the tip is unaltered and can be used for another set of IV curves. The tip was positioned directly to the right of the area where the last IV curves were taken and the voltage swept, this time between -2 to 2 V. The IV characteristics are similar to those seen in Figure 4.5d, f, where the transition voltage for both wires on the positive side is about 1.3 V however the negative side has a transition voltage of -2.2 V for Figure 4.5d,f and around -1.8 V for Figure 4.7e. The decrease in conductivity in the negative bias region appears to be thickness dependent. The first wire had a thickness of 20 nm and a transition voltage of -2.2 V whereas the other wire was 15 nm and had a transition voltage of -1.8 V. This is similar to a trend seen in $TPSS_4$ nanorods where there was a small shift in the positive bias but the negative bias, based on thickness, decreased exponentially indicating a tunneling charge transport process. The positive bias, for $TSPP_4$ nanorods, the conductivity did not quench with lower temperature which indicates that the conduction mechanism is not thermally activated or the activation energy is smaller than 10 mV, it is possible that similar behavior might be seen in TCPP nanowires. The LUMO orbitals of the $TSPP_4$ AND TCPP are both strongly coupled to each of their respective molecules making up the aggregate providing a large conduction band. This data as

presented is for conduction along the transverse direction which minimizes effects of scattering by means of defects, chemical impurities, etc. due to the short electronic path After the IV were acquired another image was taken to see if there was any damage to the sample. A hole that is left after the measurement that is likely a direct result of the high currents placed through the wire. It may be possible to use the current as a means of estimating the energies holding the molecules together through ionic interactions as well as hydrogen bonding.

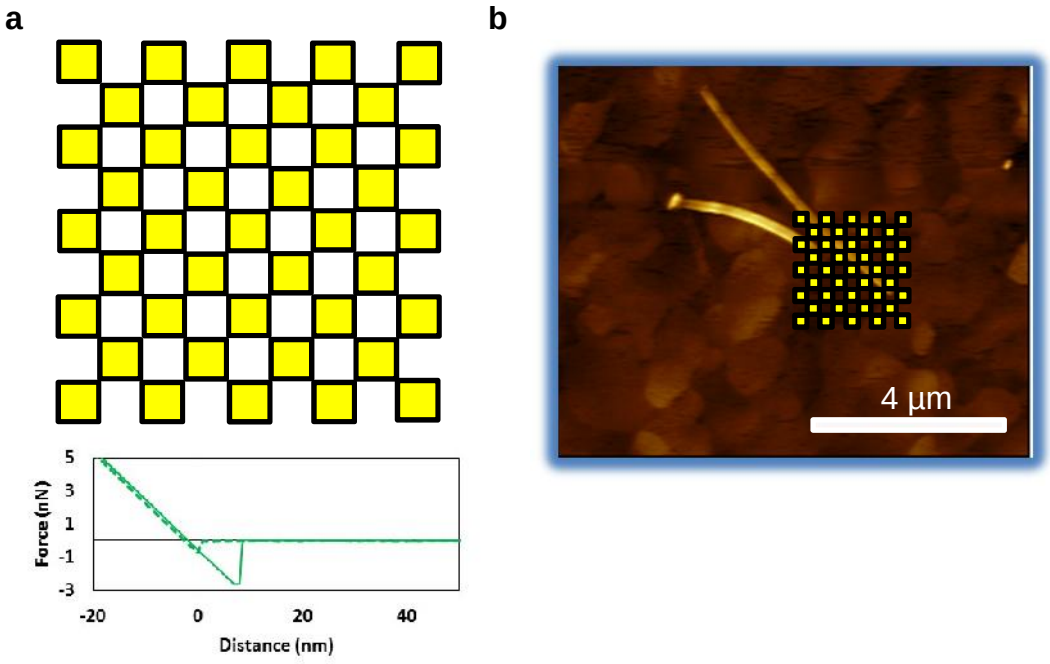


**Figure 4.8.** (a)Pattern showing the grid layout for each Force Distance curve (FD) to be taken which will trigger the IV curve once the force set-point is reached. (b) Grid overlay over top of TCPP nanowire.

Although the method for switching between tapping to contact mode for performing IV analysis on the wires was mostly a success there is an alternative way to perform this

electrical measurement. The technique, shown in Figure 4.8a takes an example from force volume mapping, that is, instead of placing the tip in contact in contact mode the tip is retracted and force distance maps are performed at each pixel (Figure 4.8b). At the end of each force distance pixel, (after acquiring 5-10 FD curves) IV is triggered (10 IV curves) at a set force with the compliance (that is the highest current that will be allowed to be measured through the tip) to be set at around 10 nA so that the TCPP nanowire do not disassemble as a result of high current density). The advantage of this is twofold, one is that the force sensitivity is much better than placing the tip directly on top of the wire compared to moving the tip without acquiring a force curve. Second is mechanical information (adhesion, and elastic modulus) can be mapped with the electrical information which might provide some insight into the relationship between the two that is not immediately clear. This could be especially important while studying the transition from nanoplates to nanowires since we should see a difference in band structure (because of confinement effects) as well a difference in mechanical properties.

## 4.4 Conclusion

Ionic TCPP nanowires were formed through a simple acidification method and their morphological and electrical properties were investigated. AFM showed an interesting step like structure that suggests there is an ordered internal structure that may be brick-like. This suggests that the wires are a result of higher order structuring from subset aggregate units stacking together. The electrical properties of the wires appear to be semiconducting with an interesting trend in the thickness of the wire and the shift of the HOMO to larger voltage at thicker material. More work is necessary in order to

determine if the observed gap is accurate or the real gap is obscured because of systematic error in the measurement process. By performing force distance curves along the line and triggering the IV curve at the correct force may aid in providing accurate electromechanical description of the TCPP nanowires.

## 4.5 References


1. McHale, J. L. Hierarchal Light-Harvesting Aggregates and Their Potential for Solar Energy Applications. *J Phys Chem Lett* **2012,** *3* (5), 587-97.

2. Cherian, S.; Wamser, C. C. Adsorption and photoactivity of tetra(4-carboxyphenyl)porphyrin (TCPP) on nanoparticulate TiO2. *J Phys Chem B* **2000,** *104* (15), 3624-3629.

3. Roth, K. M.; Dontha, N.; Dabke, R. B.; Gryko, D. T.; Clausen, C.; Lindsey, J. S.; Bocian, D. F.; Kuhr, W. G. Molecular approach toward information storage based on the redox properties of porphyrins in self-assembled monolayers. *Journal of Vacuum Science & Technology B: Microelectronics and Nanometer Structures Processing, Measurement, and Phenomena* **2000,** *18* (5), 2359-2364.

4. Gryko, D. T.; Clausen, C.; Roth, K. M.; Dontha, N.; Bocian, D. F.; Kuhr, W. G.; Lindsey, J. S. Synthesis of "Porphyrin-linker-Thiol" molecules with diverse linkers for studies of molecular-based information storage. *J Org Chem* **2000,** *65* (22), 7345-55.

5. Liu, Y.; Wang, L.; Feng, H.; Ren, X.; Ji, J.; Bai, F.; Fan, H. Microemulsion-Assisted Self-Assembly and Synthesis of Size-Controlled Porphyrin Nanocrystals with Enhanced Photocatalytic Hydrogen Evolution. *Nano Lett* **2019,** *19* (4), 2614-2619.

6. Zhang, N.; Wang, L.; Wang, H.; Cao, R.; Wang, J.; Bai, F.; Fan, H. Self-Assembled One-Dimensional Porphyrin Nanostructures with Enhanced Photocatalytic Hydrogen Generation. *Nano Lett* **2018,** *18* (1), 560-566.

7. Schwab, A. D.; Smith, D. E.; Rich, C. S.; Young, E. R.; Smith, W. F.; de Paula, J. C. Porphyrin nanorods. *J Phys Chem B* **2003,** *107* (41), 11339-11345.

8. Rotomskis, R.; Augulis, R.; Snitka, V.; Valiokas, R.; Liedberg, B. Hierarchical structure of TPPS4 J-aggregates on substrate revealed by atomic force microscopy. *J Phys Chem B* **2004,** *108* (9), 2833-2838.

9. Wang, Z. C.; Medforth, C. J.; Shelnutt, J. A. Porphyrin nanotubes by ionic self-assembly. *J Am Chem Soc* **2004,** *126* (49), 15954-15955.

10. Friesen, B. A.; Nishida, K. R. A.; McHale, J. L.; Mazur, U. New Nanoscale Insights into the Internal Structure of Tetrakis(4-sulfonatophenyl) Porphyrin Nanorods. *J Phys Chem C* **2009,** *113* (5), 1709-1718.

11. Friesen, B. A.; Wiggins, B.; McHale, J. L.; Mazur, U.; Hipps, K. W. Differing HOMO and LUMO mediated conduction in a porphyrin nanorod. *J Am Chem Soc* **2010,** *132* (25), 8554-6.

12. Hollingsworth, J. V.; Richard, A. J.; Vicente, M. G.; Russo, P. S. Characterization of the self-assembly of meso-tetra(4-sulfonatophenyl)porphyrin (H(2)TPPS(4-)) in aqueous solutions. *Biomacromolecules* **2012,** *13* (1), 60-72.

13. Vlaming, S. M.; Augulis, R.; Stuart, M. C. A.; Knoester, J.; van Loosdrecht, P. H. M. Exciton Spectra and the Microscopic Structure of Self-Assembled Porphyrin Nanotubes. *J Phys Chem B* **2009,** *113* (8), 2273-2283.

14. Schwab, A. D.; Smith, D. E.; Bond-Watts, B.; Johnston, D. E.; Hone, J.; Johnson, A. T.; de Paula, J. C.; Smith, W. F. Photoconductivity of self-assembled porphyrin nanorods. *Nano Lett* **2004,** *4* (7), 1261-1265.

15. Yeats, A. L.; Schwab, A. D.; Massare, B.; Johnston, D. E.; Johnson, A. T.; de Paula, J. C.; Smith, W. F. Photoconductivity of self-assembled nanotapes made from meso-tri(4-sulfonatophenyl)monophenylporphine. *J Phys Chem C* **2008,** *112* (6), 2170-2176.

16. Riley, C. K.; Muller, E. A.; Feldman, B. E.; Cross, C. M.; Van Aken, K. L.; Johnston, D. E.; Lu, Y.; Johnson, A. T.; de Paula, J. C.; Smith, W. F. Effects of O-2, Xe, and Gating on the Photoconductivity and Persistent Photoconductivity of Porphyrin Nanorods. *J Phys Chem C* **2010,** *114* (45), 19227-19233.

17. Meng, Q. S.; Zhang, C.; Zhang, Y.; Zhang, Y.; Liao, Y.; Dong, Z. C. Tunneling electron induced molecular electroluminescence from individual porphyrin J-aggregates. *Appl Phys Lett* **2015,** *107* (4).

18. Sakuma, T.; Sakai, H.; Hasobe, T. Preparation and structural control of metal coordination-assisted supramolecular architectures of porphyrins. Nanocubes to microrods. *Chem Commun* **2012,** *48* (37), 4441-4443.

19. Serra, V. V.; Andrade, S. M.; Neves, M. G. P. M. S.; Cavaleiro, J. A. S.; Costa, S. M. B. J-aggregate formation in bis-(4-carboxyphenyl)porphyrins in water : pH and counterion dependence. *New J Chem* **2010,** *34* (12), 2757-2765.

20. Beddard, G. S.; Porter, G. Concentration quenching in chlorophyll. *Nature* **1976,** *260* (5549), 366-367.

21. Choi, M. Y.; Pollard, J. A.; Webb, M. A.; McHale, J. L. Counterion-dependent excitonic spectra of tetra(p-carboxyphenyl)porphyrin aggregates in acidic aqueous solution. *J Am Chem Soc* **2003,** *125* (3), 810-20.

22. Doan, S. C.; Shanmugham, S.; Aston, D. E.; McHale, J. L. Counterion dependent dye aggregates: nanorods and nanorings of tetra(p-carboxyphenyl)porphyrin. *J Am Chem Soc* **2005,** *127* (16), 5885-92.

23. Wan, A. Self Assembly of Nanostructures. Ph.D., Texas A&M University2011.

24. Lei, S. B.; Wang, C.; Yin, S. X.; Wang, H. N.; Xi, F.; Liu, H. W.; Xu, B.; Wan, L. J.; Bai, C. L. Surface stabilized porphyrin and phthalocyanine two-dimensional network connected by hydrogen bonds. *J Phys Chem B* **2001,** *105* (44), 10838-10841.

# CHAPTER V

# DEVELOPMENT OF AMBIENT PRESURE LOW NOISE SCANNING THERMALVOLTAGE MICROSCOPE

## 5.1 Introduction

Scanning probe microscopy (SPM) has a multitude of techniques that are meant to move beyond simply studying the morphological characteristics of the samples from hundreds of microns down to single atoms. These include studying thermal,[1] surface potential,[2] conductivity,[3, 4] photovoltaic,[5] capacitance,[6] nanomechanical, and magnetic,[7, 8] properties of materials. Electrical measurements in particular can provide information relating to the band-structure and charge transport mechanisms. An important method for measuring charge carrier type (p or N type) and concentration involves the Seebeck effect. This is the effect used in thermocouples for measuring temperature differences at junctions using two dissimilar metals. The voltage that is developed ΔV, when there is a temperature difference present, is $-\Delta V = S * \Delta T$ where S is called the Seebeck coefficient and T is the temperature. S is typically small for metals and insulators and large for semiconductors. When a temperature differential is developed charge carriers are able to diffuse across the junction and the sign of the voltage is a signature of the carrier type.[9] The measurement is traditionally performed with metal contacts with microsized probes providing contacts either in the vertical or lateral configuration.[10, 11]

Under the umbrella of SPM, scanning tunneling microscopy (STM) is one of the most widely used instruments for studying nanoscale electrical properties of materials, mostly by the use of constant current imaging, local barrier height through dI/dZ, I/V

spectroscopy, dI/dV spectroscopy. The measurement of dI/dV is usually performed at open loop condition through a lock-in technique that is typically performed at lower temperatures (relative to ambient, depending on the bandwidth of the amplifier and impedance of the junction) due to issues with thermal induced drift. Work performed by Williams et. al. showed that with a temperature gradient, and if the sample is sufficiently conductive, a voltage could be measured that was associated with the chemical potential of the surface.[12] Following this work a theoretical framework was developed to understand the origins of the thermoelectric voltage signal.[13] Assuming that the local density of states varies linearly with the energy around the fermi level and the voltage present is smaller than kT then the thermoelectric voltage can be expressed as

$$V_{th} = \frac{\pi^2 k^2}{6e}(T_t^2 - T_s^2)\left(\frac{\partial \ln \rho_t}{\partial E} + \frac{\partial \ln \rho_s(x,y)}{\partial E} + \frac{z}{\hbar}\sqrt{\frac{2m}{\phi}}\right) \quad (5.1)$$

Where k is the Boltzmann constant, $\hbar$ is Planck's constant, m is the mass of the electron, $\phi$ is the work function, $\rho_t$ and $\rho_s$ are the density of states of the tip and sample and $T_t$ and $T_s$ are the tip and sample temperature. There are three main terms that contribute to the thermoelectric voltage signal, with the $\frac{\partial \ln \rho_s(x,y)}{\partial E}$ term dominating the signal, however, the signal level depends on the gap distance (third term) and of course a smooth density of states of the tip.[13, 14]

There are two variations that can be utilized to obtain thermoelectric voltage maps of the surface using a scanning tunneling microscope. As shown in Figure 5.1a, the switch-based set-up takes advantage of an electronic relay that can be used to switch from a current amplifier (closed circuit, biased tip/sample) to a voltage amplifier (open circuit,

ground sample or tip).[12, 15, 16] This method is relatively easy to implement into existing commercial STM instruments and have several different ways to accomplish. One way to do this is upon taking an image of the surface under constant current imaging, at the end of the scan line a transistor-transistor logic (TTL) signal (a voltage pulse that, in this case, will denote that the end of a scan line is complete), is used to switch between the current amplifier to the voltage amplifier. The measured thermoelectric voltage signal is actually distance dependent (this will be detailed later) so the height can be changed, and the tip scanned back over the sample (forward and reverse scan). Depending on the length of the wire from the tip to the amplifier the switching between the current and voltage amplifier can introduce a large amount of capacitance that will need to be discharged before measuring the small voltages. The voltage amplifier can be a number of different electronics such as a low noise commercial electrometer, differential amplifier, or an instrumentation amplifier. Depending on the bandwidth and the input impedance of the electronics different samples can be measured and various levels of contrasts can be obtained. One of the major disadvantageous of this technique is the signal is not simultaneously recorded with the constant current imaging. In addition, there are some STM controllers that do not allow access to the TTL signal leading researchers to find the signal on the control board which is likely out of the area of expertise to many.

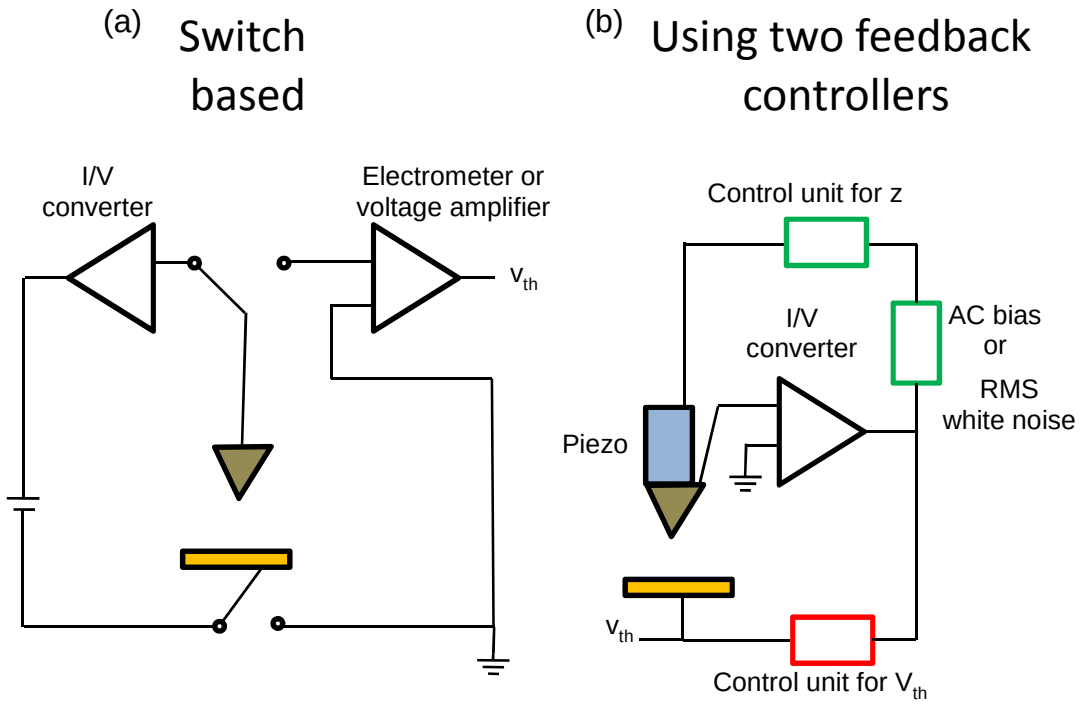


**Figure 5.1.** Schematic of thermoelectric voltage measurement set-ups a) switch based and (b) feedback controlled for simultaneous measurement of topography and thermoelectric voltage.

An alternative way, which has found most applications in ultra-high vacuum (UHV) STM experiments where the use of external connected equipment to the tip/sample circuit may not be possible, uses only the current measured at the tip from the transimpedance amplifier (Figure 5.1b). In order to measure the thermoelectric voltage a separate feedback loop is needed to null the thermally induced current to measure a dc thermoelectric voltage. For distance regulation there are two main ways to make the measurement (making use of some form of modulation on the sample) using either an AC voltage or measuring the power spectral density at some frequency of the thermal noise in the tunnel junction. The AC method is typically performed by applying a small AC voltage

to the tunneling gap, where the AC component of the tunneling current is proportional to the tunneling conductance, which has the same exponential dependence as the tunneling current and so can be used for measuring the topography.[14, 17, 18] While this technique can provide very clear thermoelectric voltage contrast it is much more susceptible to capacitive cross talk between the signals. Instead of using an AC voltage for the modulation, which controls the tip-sample distance, one can use the thermal noise in the tunneling junction as an internal modulation of the white noise.[19]

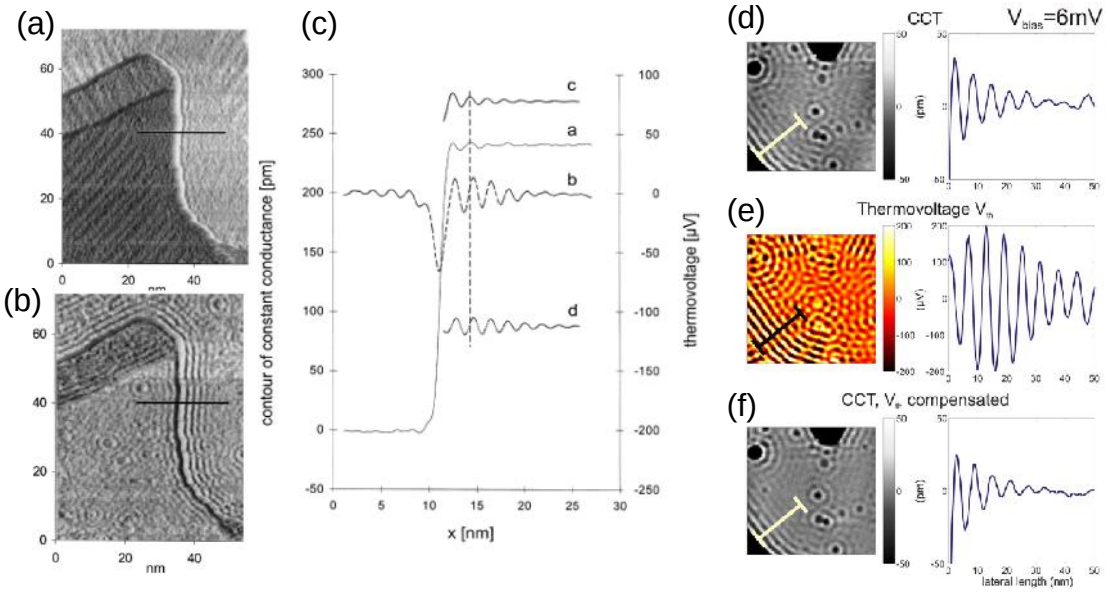


**Figure 5.2.** Au(111) STM of (a) topography and (b) thermoelectric voltage (c) cross section of (a) and (b) overlaid with calculation of thermoelectric voltage amplitude. Ag(111) surface at cryogenic temperature, dI/dV at 6mV before thermoelectric voltage correction (d), thermoelectric voltage signal e) and after thermoelectric voltage correction (f). Part (a), (b) and (c) adapted with permission from Hoffmann et al.[20] Copyright 1997 AIP Publishing. Part (d), (e), and (f) adapted with permission from Homoth et.al.[21] Copyright 2007 APS Publishing.

The root mean square (RMS) of the tunneling current, filtered within a certain bandwidth, has been shown to have the same exponential dependence as the tunneling current. The

resolution for both of these methods is roughly 1 μV, which is still lower than the voltages expected for metals where the Seebeck coefficients are between 1-10 μV/K.

The total number of papers that have used STVM to image their samples is quite modest, with roughly 20 or so unique papers published since 1990. Within this collection there are a large number of different systems ranging from metals, semiconductors, 2D materials, to molecules absorbed on surfaces. Metals were some of the first samples investigated by STVM because metal surfaces can be cleaned and reconstructed routinely in UHV, providing an ideal test sample. Figure 5.2a shows a topography image of a reconstructed Au(111) surface and the corresponding thermoelectric voltage image (Figure 5.2b) taken at roughly 5 K above room temperature (the tip in this case was heated with a 40 mW laser).[20, 22] Comparing the two images, the contrasts are much more prominent in the thermoelectric voltage signal, showing large fringe patterns on the surface of Au(111). The oscillatory behavior is attributed to screening of the step potential by the surface state which results in Friedel oscillations of electron density and are strongest near step edges and defects. A quick calculation was made to sheds light on the qualitative behavior of the lateral variation in the thermoelectric voltage, which shows that the variation is not influenced greatly by variations in parameters relating to the states of the tip, projected density of states of the sample and the weights of the surface states, although the amplitudes in Figure 5.2c were strongly influenced by the slope of the dispersion relation of the surface state.

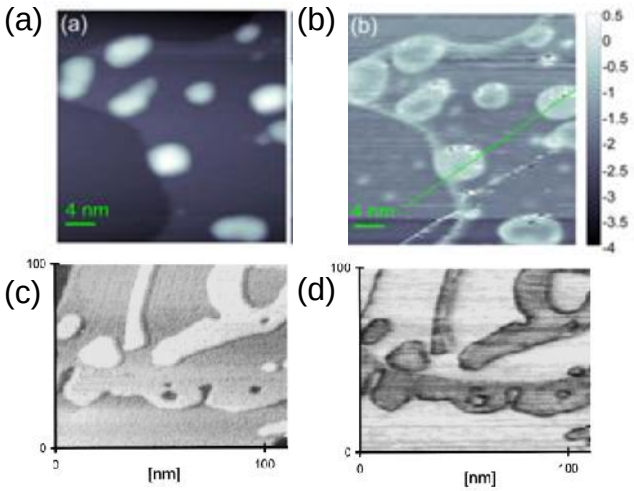


**Figure 5.3**. Epitaxial growth of Fe nanoparticles on Ag(111) via STM (a) topography and (b) thermoelectric voltage. Epitaxial growth of Ag grown on Au(111) (c) topography (d), thermoelectric voltage. Part (a) and (b) adapted with permission from Maksymovych et al.[18] Copyright 2014 ACS Publishing. Part (c) and (d) adapted with permission from Hoffmann et al.[20] Copyright 1997 AIP Publishing.

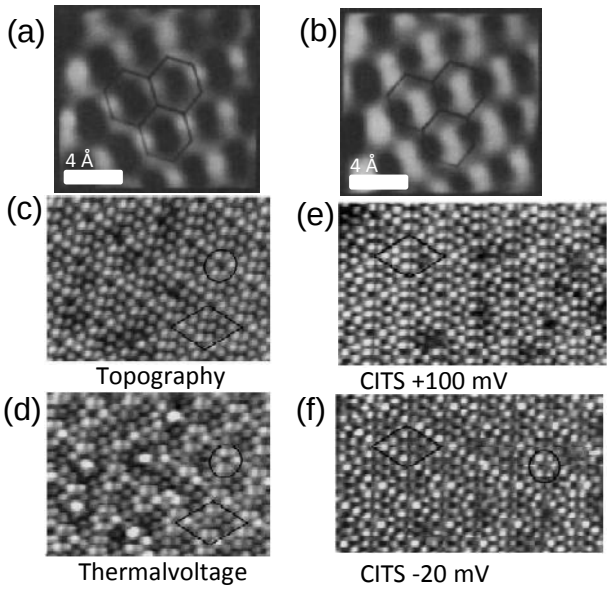


**Figure 5.4.**Bulk $MoS_2$, STM (a) topography and (b) thermoelectric voltage. Si(111) STM (c) topography, and (d) thermoelectric voltage signal. e) dI/dV map, +100 mV and (f) -20 mV. Part (a) and (b) adapted with permission from Williams et al.[12] Copyright 1990 Springer Nature Publishing. Part (c),(d),(e) and (f) adapted with permission from Hoffmann et al.[22] Copyright 2000 Elsevier Publishing.

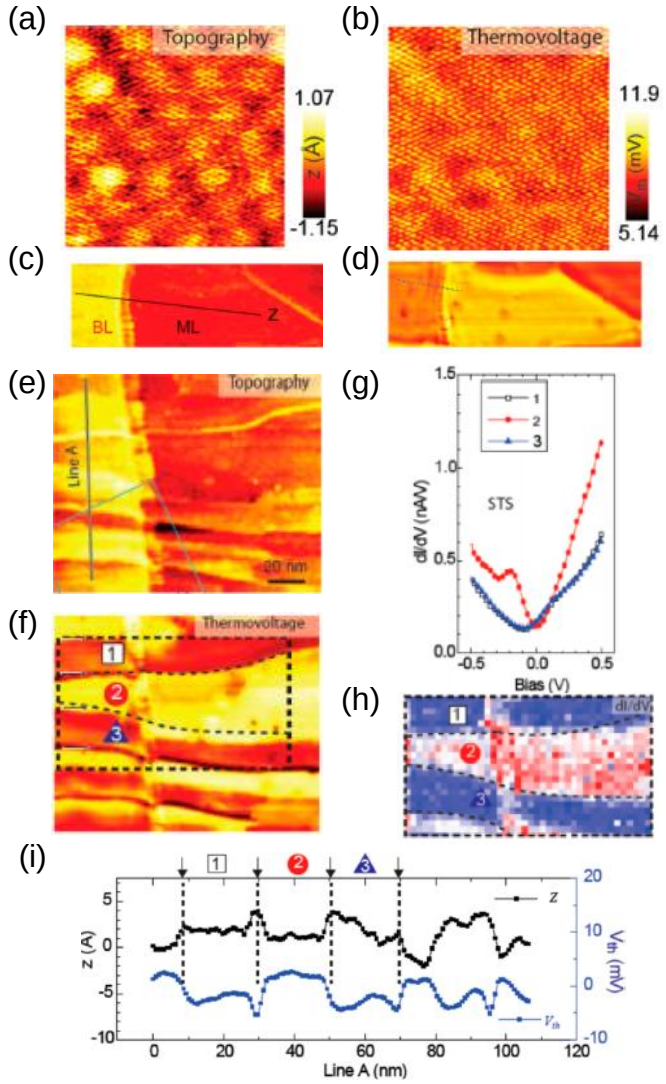


**Figure 5.5.** Atomic resolution epitaxial graphene on SiC, STM (a) topography and (b) thermoelectric voltage. Monolayer and bilayer boundary (c) topography (d) thermoelectric voltage signal. Structural wrinkles in graphene SiC e) topography, f) thermoelectric voltage. dI/dV spectrum on different domains. dI/dV map at -500 mV as indicted in e).Cross section of line indicated in e), showing height differences of areas on the same terrace with variable thermoelectric voltage contrast. Reprinted with permission from Park et. al.[23] Copyright 2013 ACS Publishing.

A lot of scanning tunneling measurements are performed at cryogenic temperatures and involve trying to understand the density states of materials. If a temperature difference exists between the sample and the tip, whether intentional or not,

thermoelectric voltages will be present in the dI/dV signal. The density of states of Ag(111) surfaces as seen in Figure 5.2d must be compensated based of the thermoelectric voltage Figure 5.2e to reveal the true density states of the samples as seen in Figure 5.2f.[21] When metals are grown on metal surfaces a heterogeneous interface will form. Although STM can be used to measure the surface topography it is not always obvious from the image what contrast corresponds to which metal. Figure 3a shows the topography of Fe nanoparticles grown on Ag(111) surfaces.[18] Although there appears to be a height difference between the flat Ag(111) surface and the brighter, presumably, Fe nanoparticles it is not clear the extent of the coverage. The thermoelectric voltage (Figure 5.3b) provides a clear contrast between the Ag and the Fe which authors have claimed is independent of the tip and its termination. The authors noted that quoting a specific value for the thermopower is not justified since the distance dependence study conducted showed a significant slope for $V_{th}(z)$ which in recent work has been associated with the work function of the material. The authors claim that the streakiness of their images are a result of the modification of the tip apex at room temperature which creates large thermoelectric voltage noise variation. Another example of the sharp contrasts showed with STVM for Ag atoms evaporated onto Au(111) surfaces as shown in Figure 5.3c (topography) vs Figure 5.3d (thermoelectric voltage).[20, 22] Comparing the two images the top portion of the topography suggests that there is material that is present that is likely to be the Ag islands, which is corroborated by the thermoelectric voltage image. What is not immediately obvious from the topography (since the height difference between Ag and Au is about 0.01 nm) is the Ag at the steps which are likely to have diffused across the surface.

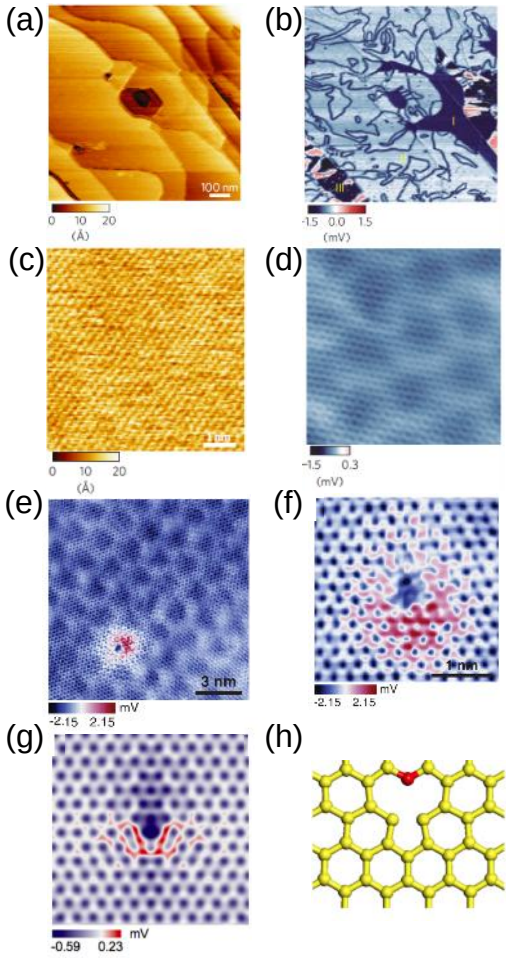


**Figure 5.6.** UHV AFM on epitaxial graphene on SiC with 3 distinct regions I (monolayer), II (bilayer) and III (trilayer) a) topography b) thermoelectric voltage image. AFM bilayer graphene (a) topography and (b) simultaneous atomically resolved thermoelectric voltage image. Large area atomic scale thermoelectric voltage with a point defect (e) and a small area thermoelectric voltage (f). Simulated image of thermoelectric voltage of substitutional oxygen in n-doped freestanding graphene (g). Atomic model of thermoelectric voltage as shown in (g) as a comparison (h). Part (a), (b), (c), and (d) adapted with permission from Cho et al.[24] Copyright 2013 Springer Nature Publishing. Part (e), (f), (g) and (h) adapted with permission from Lee et al.[25] Copyright 2014 APS Publishing.

Only two experiments have been performed using STVM to study semiconductors. In fact the first study published was termed scanning chemical-potential microscopy and obtained images of $MoS_2$ (Figure 5.4a topography and Figure 5.4b thermoelectric

voltage).[12] This work was the first to point out the interesting difference in the atomic resolution thermoelectric voltage having a contrast difference, that is, in the topography where the density of states is higher the thermoelectric voltage signal is weaker. This phenomenon is also seen in other works utilizing STVM however no explanation to the origin of this effect is given, only that it is observed. Si(111) has been studied in some detail using STVM.[22] This is interesting because in order to obtain a thermoelectric voltage signal there must exist a non-vanishing electronic density of states, which might not be expected in high bandgap semiconductors. It turns out that the surface states of the semiconductor may create density of states near the Fermi level, $E_F$. Figure 5.4c,d shows the constant current and thermoelectric voltage of the Si(111) respectively. The images look very similar however the contrast of the thermoelectric voltage appears to have a larger variation in the faulted and unfaulted unit cell. By looking at the Current Imaging Tunneling Spectroscopy (CITS) images at 100 mV (Figure 5.4e) and -20 mV (Figure 5.4f) interesting parallels can be drawn from the contrasts relative to the thermoelectric voltage. The unfaulted portion of the thermoelectric voltage appears brighter than the faulted side, something that is seen in the -20 mV CITS. The contrasts that are seen are dependent on the tip states, something that has been discussed in detail in other works.[13, 14, 23] This makes sense since the density of states of the tip contribute to the observed thermoelectric voltage signal (this is true as well for imaging but probably more so since it is the derivative of the density of states that matters).

Since STVM is very sensitive to the change in the density of states of the materials, as stated previously, characteristics of the surface can be seen with high fidelity such as

atomic scale defects, standing waves and dopent sites. Two-dimensional materials, such as graphene, are a very exciting area of research because of not only the interesting physics that arises out of spatial confinement but also the promising applications in electronics, photonics, chemical sensors, etc. To date there are only three papers that have published work studying the electrical and thermoelectric properties of graphene on Silicon carbide (SiC).[23, 24, 25] The work from Park et.al. looked at the effect on the local electronic structure by the thermally induced strain from epitaxial growth of graphene on SiC(0001).[23] Figure 5.5a,b show the topography and thermoelectric voltage, respectively of the graphene SiC moiré pattern that can be resolved in both images. The moiré pattern is a result of the interference of the 6x6 buffer layer, but what is peculiar is the thermoelectric voltage signal has a much smaller contrast for this moiré pattern while the atomic resolution suggests that the contrast is strongly dependent on the samples density of states. Figure 5.5c,d show the topography and thermoelectric voltage of bilayer to monolayer graphene boundary respectively, where the topography does not appear to show very many interesting features however, from the thermoelectric voltage image there is a large transition from bilayer to monolayer at the step edge that is attributed to the Fermi level shift near the Dirac point (the carrier concentrations change because of the change in the interactions between the graphene and the substrate which leads to a change in the local densities of state). The defects are also obvious in the thermoelectric voltage but also the oscillatory structures on the bilayer graphene which have been attributed to the chiral nature of the quasiparticles in graphene (not seen in monolayer because of scattering suppression). Structural distortions, as a result of the negative thermal expansion

coefficient of graphene (it expands upon cooling), modify the electronic landscape of the graphene. Figure 5.5e, f show the topography and thermalvoltage respectively of graphene on SiC with 3 distinct areas on the same terrace being designated. Figure 5.5g shows the averaged dI/dV spectra of each of the respective areas and Figure 5.5h shows a dI/dV spectroscopy map at -500mV showing the higher conductivity in area 2 versus area 1 and 3, which can be seen to compliment with the thermoelectric voltage map. This is a result of wrinkles in the graphene (where Area 1 and 3 are decoupled from the other graphene layer at the edges). Figure 5.5i shows a cross section showing the 1-2 Å height difference between Areas 1 and 3, which compared to Area 2 provides evidence of the wrinkle effect described. This approach of incorporating STVM provides a unique way to study the electronic, thermoelectric and structural properties of 2D materials in general.

Up until now all the work regarding STVM was performed in STM mode. The opportunity to use an AFM for feedback means that the electric circuit is independent of the z feedback mechanism. There has been a few atomic force microscopy single point thermoelectric voltage spectroscopy publications[26, 27, 28, 29] however there appears to be only three publications using STVM. The work was performed in a UHV AFM using an electrometer to measure the thermoelectric properties of epitaxial graphene grown on SiC[24, 25] or copper[30]. The AFM thermoelectric voltage work is complementary to the STM work just mentioned, in fact the authors go into detail that is mostly omitted from much of the literature, scan speed. This is important because the bandwidth requirements are more difficult to obtain for low noise voltage measurements because they are sensitive to the effects of shielding, guarding and grounding characteristics of the circuit and sample

impedance. An electrometer was used to measure the voltage, which is interesting since the bandwidth on most high grade electrometers are a few hundred Hz, however the one used appear to have sufficient bandwidth to perform the work (the impedance of the sample, as it becomes larger, will degrade the bandwidth). One of the most interesting aspects of the work is the ability to scan large areas, as can be seen in topography (Figure 5.6a) and thermoelectric voltage (Figure 5.6b). AFM, especially in the beam bounce configuration, is not widely used for obtaining atomic resolution on samples unless they are periodic. Most often the lateral signal is obtained in contact mode and Fourier filtered to obtain the atomic resolution. Zooming into the graphene structure the moiré pattern is absent in the topography (Figure 5.6c) but is clearly resolved in the thermoelectric voltage signal (Figure 5.6d). A thermoelectric voltage map (Figure 5.6e) shows a defect site which would likely be absent in topography as well as the lateral signal. Moving beyond the tunneling model for qualitatively describing thermoelectric voltage has provided a new theoretical framework for simulating thermoelectric images in an effort at characterizing the type of defect over large scales to atomic scale. The model makes use of an empirical force balance equation for macroscopic diffusive systems as well as first principle calculations of the defect and correlating the coherent temperature profile with the van der Waals distance between the tip and the sample.[25] Figure 5.6f shows a defect site on monolayer graphene, the simulation (Figure 5.6g) used the density of states of an oxygen bridge across two carbons. It is very surprising to find that the measured and simulated thermoelectric voltages look similar. The impact of this work has yet to be fully realized because the use of UHV for measuring the thermoelectric voltage. Although having the

vacuum conditions helps prevent contamination from the ambient air there are some systems where it may not be as crucial to be under vacuum conditions. There are several STVM studies that have been performed in air and do not appear to have a dramatic loss of resolution.[12, 15]

This study aims to try to understand how an ambient low noise, high bandwidth voltage amplifier could be used to study the thermoelectric effect using atomic force microscopy. Much of the work described below is understanding the issues involved with making a high impedance measurement, use of different equipment for measuring thermoelectric voltage and discussing the construction of a battery powered instrumentation amplifier for the this purpose.

## 5.2 Experimental Methods

High purity water (18.2 MΩ·cm, NANOpure Diamond, Barnstead) was used in this study. 200 nm thick, and flame annealed, Au(111) films on mica (Phasis) were used for all conductive probe measurements. Highly ordered pyrolytic graphite was cleaned using scotch tape and used for preliminary scanning thermoelectric voltage measurement.

Au(111) was cleaned by the following procedure, the sample was UV-ozone irradiated for 10 mins, washed with copious amounts of nanopure water, ethanol, and dried with streaming N2.

**Morphological characterization:** An Asylum MFP3D was used in tapping mode and contact mode. For general imaging in tapping mode silicon tips with nominal radii of 8 nm and 170 kHz resonance frequency were used.

**Thermoelectric voltage Instrumentation:** A modified Bruker Multimode 8 and SR560 voltage amplifier were used for the preliminary Scanning Thermoelectric voltage measurement.

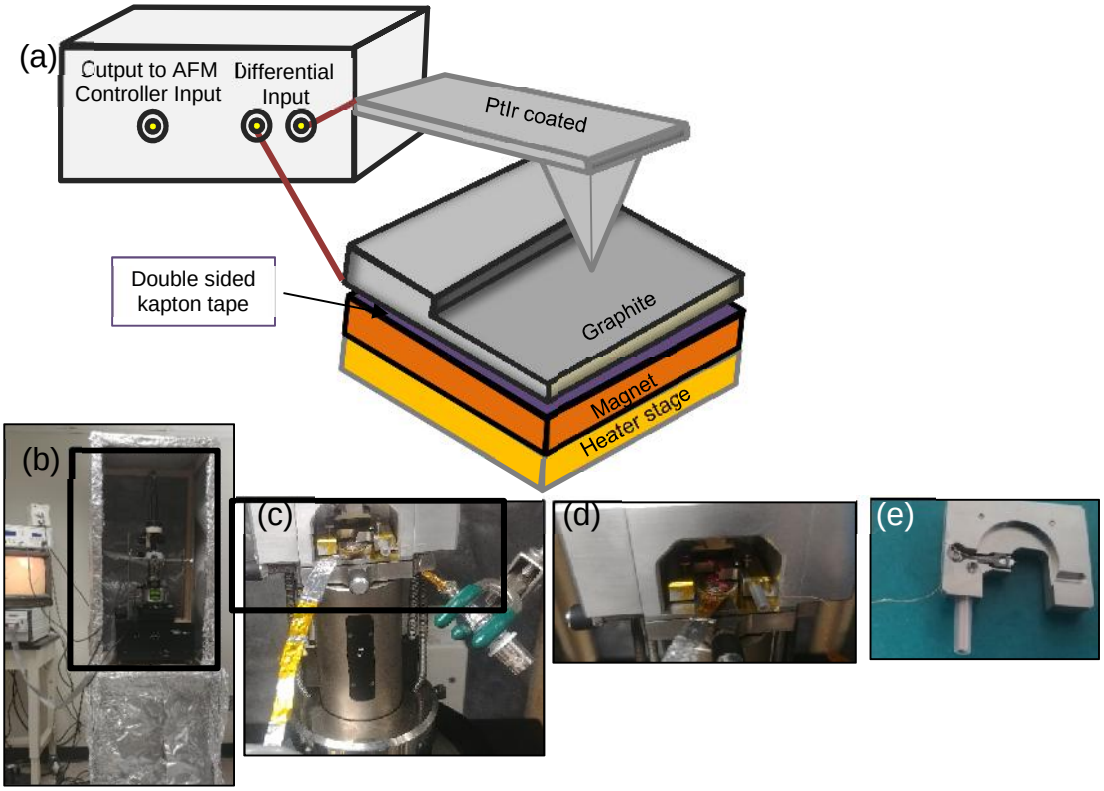


**Figure 5.7.** Schematic of thermoelectric voltage experiment on Bruker Multimode 8 (a). Experimental set-up showing the microscope assembly in the faraday cage (b), and scanner assembly (c). close up of tip holder and sample engaged (d) and the tip holder(e)

For noise analysis a modified Asylum MFP3D AFM holder and an RHK $10^8$ gain transimpedance (TIA) amplifier powered through a RHK controller (version 8). The signal for the TIA amplifier was routed from the RHK controller to the Asylum Arc2 controller for input. All metal platinum probes from Rocky Mountain Probes with a nominal radii of

20 nm were used for all conductive measurements. The noise characteristics of the signal were analyzed using the power spectral density of the TIA amplifier signal out of contact and in contact with the sample. Measuring point source thermoelectric voltage on the Asylum was performed using a Keithley 6517A high impedance electrometer, set using a guard configuration.

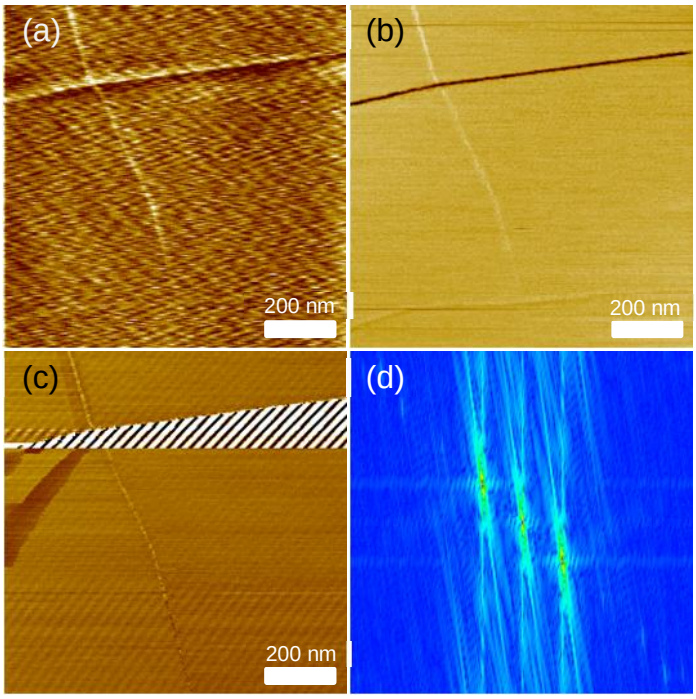


**Figure 5.8.** Contact mode AFM of Graphite, topography (a), friction (b), thermoelectric voltage (c), FFT of (c) showing the harmonics of 60 Hz noise in the thermoelectric voltage signal (d).

## 5.3 Results and Discussion

The first attempts at performing AFM based thermoelectric voltage measurement under ambient conditions were done using a modified Bruker Multimode 8 AFM. Figure 5.7a,b is a picture of the entire microscope/vibration isolation system enclosed within a home-

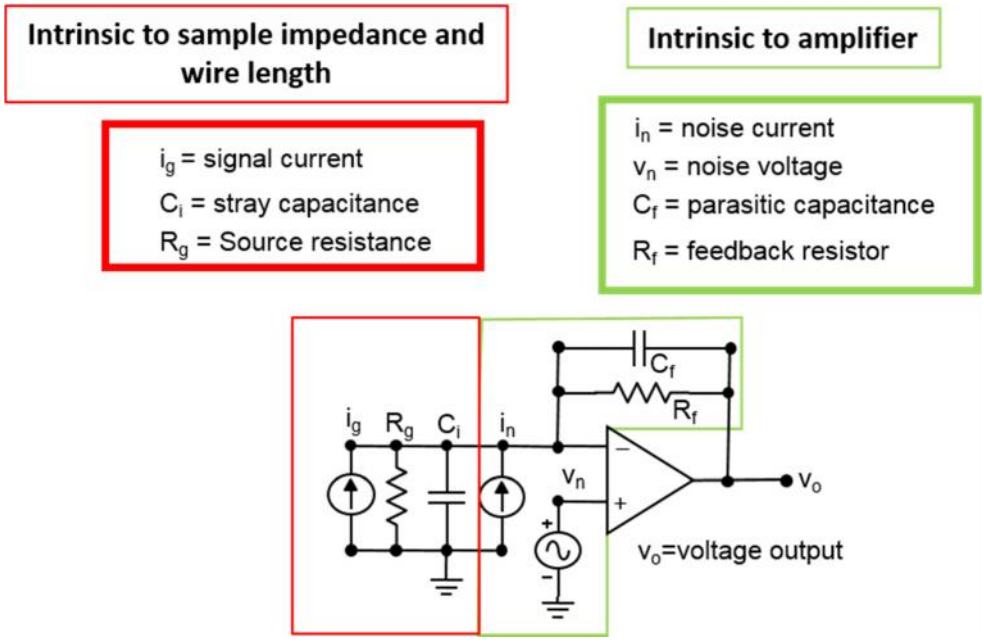


**Figure 5.9.** Noise analysis of classical transimpedance amplifier showing the intrinsic noise sources from the amplifier and the wiring from the tip.

built faraday cage for minimizing electromagnetic interference. The sample and tip holder assembly is shown in Figure 5.7c,d, where the BNC connectors have been attached directly to each of the respective holders. The tip is a PtIr coated silicon tip that has been electrically decouple from the holder using nail polish (nail polish being added to the stainless-steel holder and allowed to dry for 2 days). A kapton coated copper wire, stripped at the end, served as the signal wire which was soldered at one end to a female BNC connector. Notice in figure 5.7e that the copper wire is not shielded, this will be important later. The sample was attached to a magnetic holder with double-sided kapton tape and electrical connection was established with a piece of gold-plated brass sheet metal. The signal from the tip and sample were connected via a BNC to a 100 MΩ input impedance differential voltage amplifier. The output signal from the voltage amplifier was fed to the

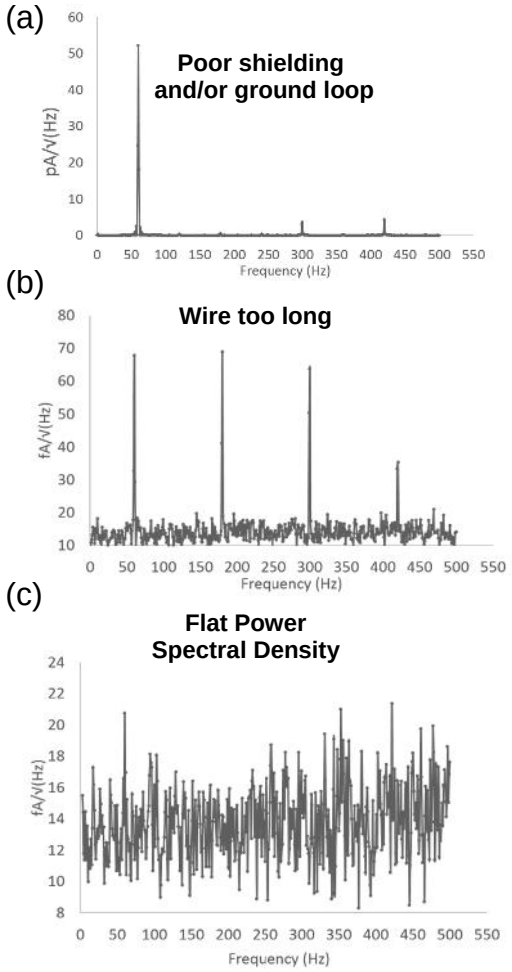


**Figure 5.10.** Power spectral density of various levels of noise introduce into the system. Ground loops or poor shielding (a). When the shielded electrical connection from the tip to the current amplifier is too long (b), when the shielded electrical connection from the tip to current amplifier is short (less than 4-7 cm) (c).

AFM controller input and the data was collected synchronously with the topography and friction image (as shown in Figure 5.8 a,b). The ripples shown in the topography signal is a result of not adequately isolated vibrations being induced into the measurement

This is one of the many problems with this set up but is an excellent example of how noise can be introduced into the measurement. The “thermoelectric voltage” signal was captured

with no temperature difference applied to the sample implying that only noise was being measured. The voltage signal (Figure 5.8c) does have some interesting features that can also be seen in topography (and some that are not). Since this is a high impedance measurement, taking place at an open circuit potential, any leakage current needs to be minimized as much as possible. Significant leakage currents that exist between the tip and sample will result in an ohmic drop which varies with impedance.[15] This will lead to a topography dependent signal which adds to the thermopower signal. The oscillations in the thermoelectric voltage signal is a result of this noise and the periodicity is 60 Hz in origin (Figure 5.8 d). In order to better understand why there is so much noise in the measurement it is important to look at the transimpedance amplifier (also known as a current amplifier, or an IV converter). Figure 5.9 shows an example of a classical transimpedance amplifier. The gain of the amplifier is defined as $v_o/i_g=N*R_f$ where $v_o$ is the output voltage in volts, $i_g$ is the signal current in amps, N is the amplification factor and $R_f$ is the feedback resistor in Ohms. There are two things to consider when trying to measure low current (that is, currents less than 1 nA), one deals with the intrinsic noise sources of the operational amplifier being used as well as the noise picked up from the signal wire and impedance of the sample. The current noise $i_n$ is in parallel with the signal current and in series with the noise voltage. The only way to keep $i_n$ low is to choose an op amp that has a current noise low enough for the required application. The parasitic capacitance is related, not only to the op amp but to the feedback resistor, and if not compensated for will induce a self-oscillation in the circuit.[31] When considering the noise sources that can be picked up from the signal wire, proper shielding and avoiding ground

loops is very important. Electric/magnetic fields can couple to the signal and can be modeled as capacitances. Leakage current can be injected into these cables where the magnitude depends on the whether the signal wire is shielded, how long the wire is and on the sample impedance.[32] The shield in the cabling is connected to ground allowing these capacitive currents to have a low impedance path. Ground loops occur when the system is grounded at several different points within the circuit. The ground currents that may be flowing through the signal originate from the 60 Hz line voltage that powers the instrument. The best advice is to make sure that the shield cable is grounded only at a single end of the cable where the measurement is taking place, preferably at the instrument side. In practice in order to check whether you have noise in your measurement a few simple tests need to be performed. First a wire was connected to a transimpedance amplifier and output voltage was measured as a function of time (if we know the gain on the amplifier, we can convert the voltage to a current). The signal was fed into an analog-digital converter (ADC) and mathematically transformed via a power spectral density (PSD) function which is a weighted distribution of a Fourier Transform binned within a particular bandwidth. Figure 5.10a shows the PSD plot of a signal that has a ground loop intentionally introduced into the system (this is also the case for a wire that is not shielded or poorly shielded). Notice the large 60 Hz peak, in some case the higher harmonics of 60Hz are seen. If the wire is shielded but the length of the wire is too long (Figure 5.10b), as explained earlier, there will be capacitive coupling between the signal and the shield which will induce a current into the signal at the line frequency. Assuming that the signal wire is short and well shielded the PSD plot should look similar to Figure 5.10c, which is

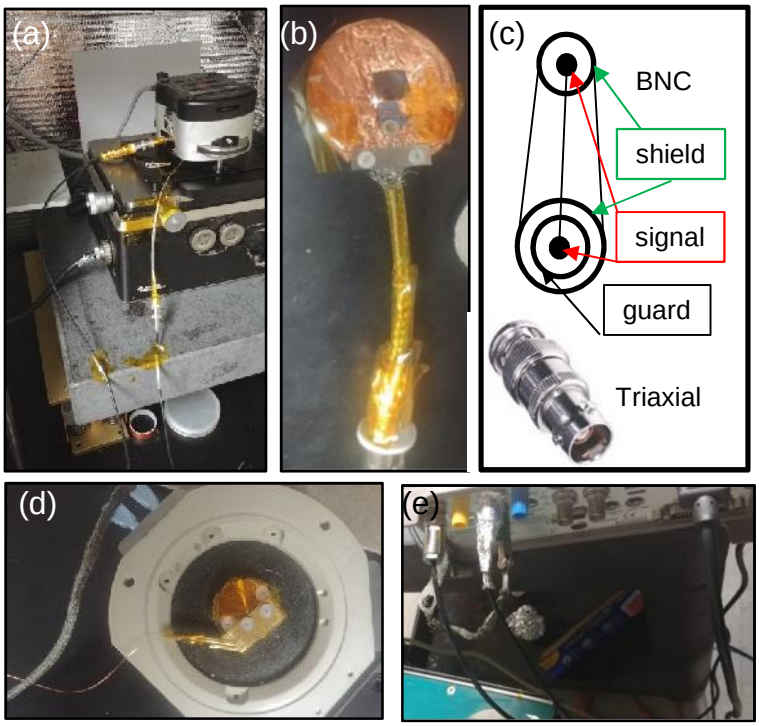


**Figure 5.11.** Single point thermoelectric voltage set-up on an MFP3D using an electrometer (a). Shielded PEEK holder with a BNC connector (b), schematic showing the BNC to triax converter showing the floating guard (c). Modified heater stage for providing the temperature difference as well as completing the circuit (d). The back of the electrometer and the connections of the triax (tip) and common (sample) (e).

characteristically flat without higher harmonics. There are several reasons for eliminating these noise sources for low current measurements. One obvious one is if a current map in conductive probe is required, once the probe is in contact with the sample, with no applied DC bias, it is likely a current will be detected. Upon scanning current will spike near step edges or areas of high topography. It is possible that the current could be so large that the tip can be rendered useless if using a metal coated probe,

The knowledge gained from understanding a low current measurements provides a foundation for understanding the demands of a low noise voltage measurement. In

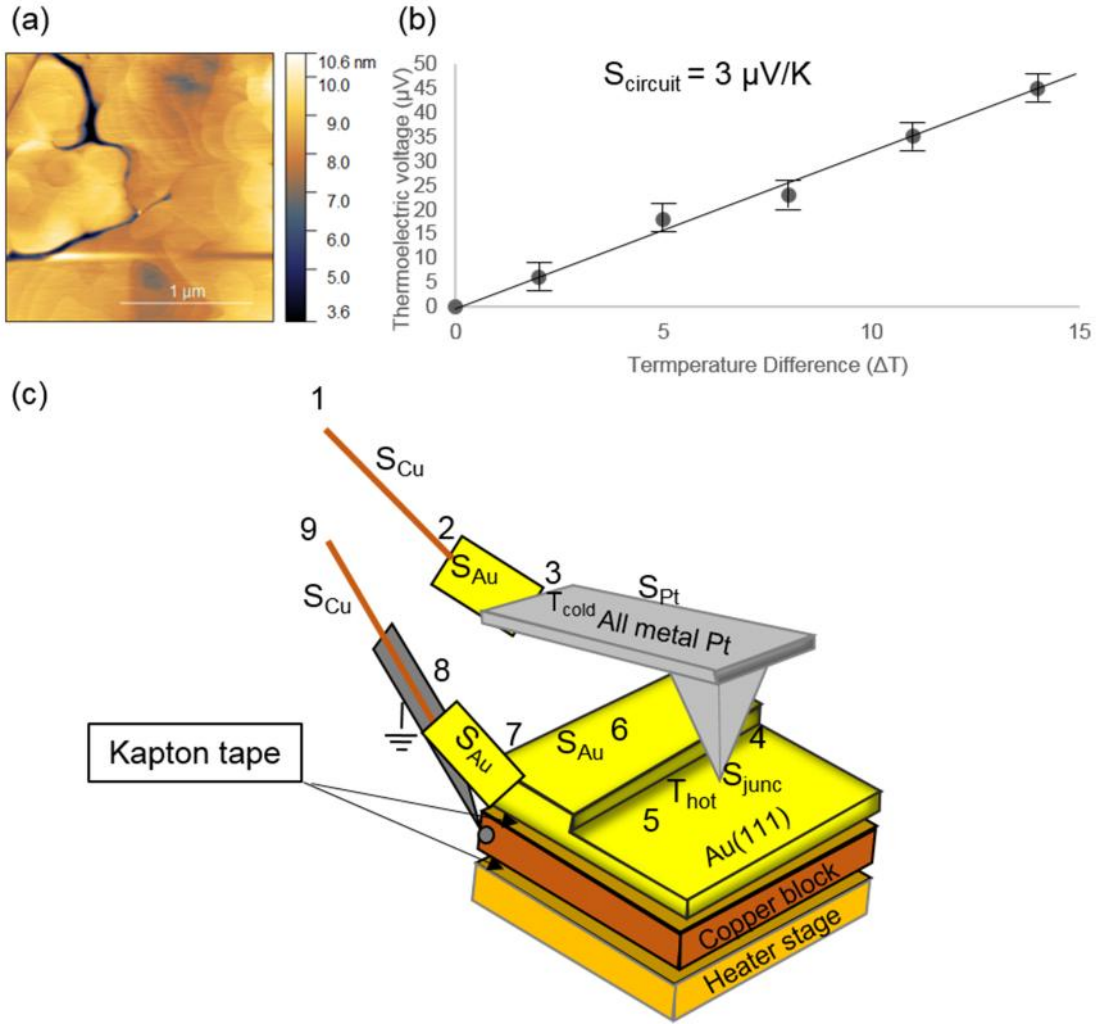


**Figure 5.12.** Contact-mode AFM of Au(111) (a). Single point spectroscopic thermoelectric voltage of Au(111) displaying the Seebeck coefficient of the circuit. Schematic diagram of the circuit in the ambient AFM thermoelectric voltage set-up showing the different materials, points (1-9) and where the voltage and temperature differences are present.

particular, voltage sources having high internal resistance (high impedance if having capacitive/inductive effects) which have errors that can accumulate such as loading errors from the input impedance, input bias current and shunt resistance/capacitance.[33] An instrument that is best suited for the task of measuring small voltages is an electrometer,

which is an instrument whose input impedance is so high (on the order of $10^{13}$-$10^{16}$ Ω) that the current flowing into the input is negligible. Figure 5.11a shows the experimental set-up of a modified MFP-3D AFM and the AFM tip holder (Figure 5.11b), which is similar to the arrangement shown in Chapter 4.

However this uses an electrometer to measure the voltage rather than a transimpedance amplifier. Another difference lies in the use of a triaxal cable using a guard for eliminating the cable capacitance that would occur from using only a BNC. The triaxal cabling works by having three conductors that are electrically isolated from each other named signal, guard, and shield. The signal carries your measurement and is at some voltage (relative to ground), the guard is set to the same voltage as the signal but has a very low impedance and the shield is grounded. If any voltage difference occurs between the signal and shield the current that would normally be injected into the signal now gets carried into the guard. The triax cable is connected to a triax to BNC converter so that a connection can be made to the AFM holder (Figure 5.11c). The sample holder is a modification of Asylums heater stage. The heating element is electrically decoupled from the copper block (used to allow for a more uniform heating distribution) using double sided kapton tape. The copper block also serves as a shield from the noise generated by the heater. The braided shield of the sample connector is mechanically/electrically coupled to the copper block by using 0/80 nylon screws. A stripped kapton coated copper wire was mechanically crimped to a gold-plated D-sub female crimp contact. This was then used to slide into a thin gold-plated copper sheet, which is used as the electrical contact to the sample Figure 5.11d. The

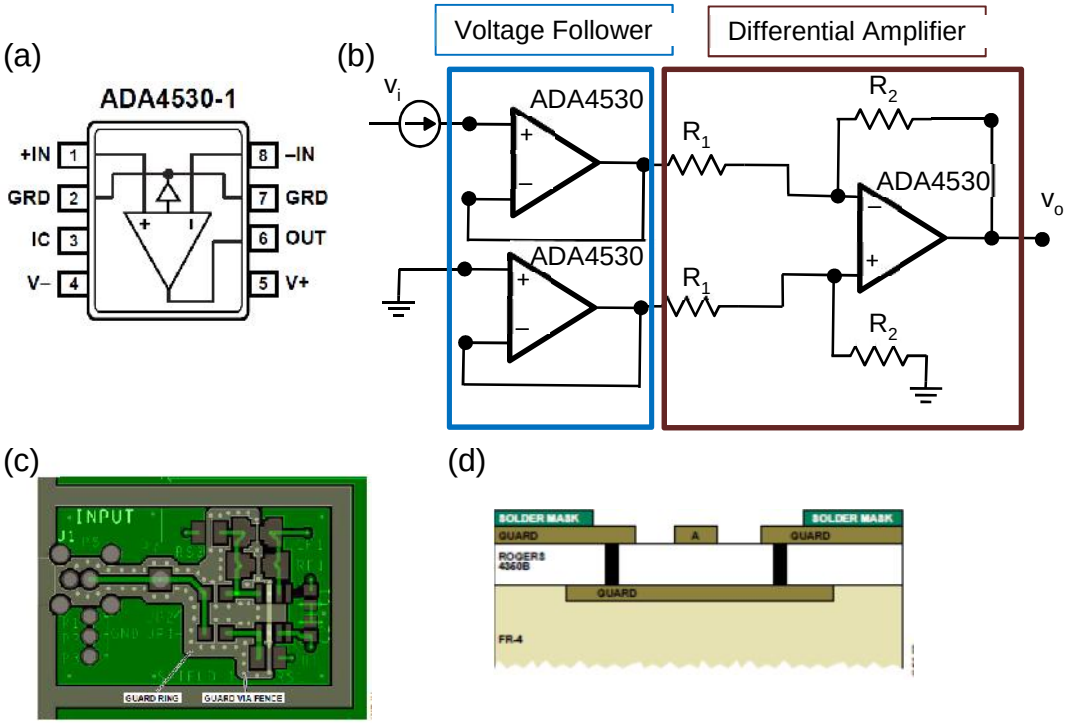


**Figure 5.13.** Pin schematic of the electrometer grade operational amplifier ADA4530-1 (a). Instrumentation amplifier configuration for measuring small thermoelectric voltages (b). Schematic of possible input arrangement for voltage follower at the tip input ($v_i$) (c). Cross-section of (c) showing the guard plate underneath the input and the high dielectric insulator Rodgers 4360B on the board.

sample connection is attached to the common of the electrometer (Figure 5.11(e)), completing the circuit. A fine K type thermocouple wire was used to measure the sample temperature. It was found that the temperature of the sample was 1 $^{o}$C off from what is measured from the thermocouple in the heater assembly suggesting low thermal losses.

To test whether the electrometer based thermoelectric voltage gives reasonable voltages a clean Au(111) sample was used. Figure 5.12a is a contact mode image of Au(111), showing clean terraces. The temperature of the stage was raised by 2 $^{o}$C for the first measurement and raised 3 $^{o}$C for every measurement up to a temperature difference

of 14 $^{o}$C. The results of the measurement are displayed in Figure 5.12b. Note the small slope value in the linear fit. This is the Seebeck coefficient (3 μV/K) for the circuit for a gold surface and an all metal platinum probe. The electrical circuit schematic is drawn in Figure 5.12c showing each of the contributing thermal resistances that contribute to the overall thermoelectric voltage measurement. Whenever there is a dissimilar metal where a thermal gradient exists thermoelectric voltages will be present. By trying to use materials with low Seebeck coefficients, matching the material connections and keeping the thermal gradients to only the stage, a more accurate measurement can be achieved. One of the greatest concerns of the circuit is the possibility that copper oxide (which can have thermoelectric voltages of 1mV) will be present on the stripped Kapton coated copper wires. The connection at site 8 is not too much of a concern since the copper wire is crimped tightly against the gold contact minimizing the possibility of oxidation. The connection at site 2 however is a concern since the wire is stripped and exposed to air for the most part. Since the thermal gradient is occurring on the sample and the thermal conductivity of air has been shown to have a minimal impact at low temperature gradients we expect the thermoelectric voltages at these sites to be negligible.[27]

Having showed that it is possible to take single point thermoelectric voltage measurements with an AFM in ambient air (at least for a low impedance system such as gold). The next step is to try to build an amplifier that has sufficient bandwidth and noise characteristics for performing scanning thermoelectric voltage microscopy. As explained in the introduction there have been several groups that have built or used instrumentation amplifiers for measuring thermoelectric voltage.[16, 27] However; only Poler[15] used the

design for scanning thermoelectric voltage whereas others had used it for single point spectroscopy.[27, 34] There is one other work that used an instrumentation amplifier for measuring the voltage, however the amplifier was monolithic, meaning it was an all in one IC which has notorious leakage currents and parasitic capacitance.[16] To overcome some of the limitations that are caused by a monolithic instrumentation amplifier the ADA4530 (pin arrangement shown in Figure 5.13a) was chosen to be configured in a three component instrumentation amplifier because of its very low input bias current (no higher than 20 fA), low voltage noise density (14nV/$\sqrt{Hz}$ ) and high input impedance, all very important characteristics for making low noise voltage measurements.[33, 35] The amplifier has an integrated guard buffer which may be useful for lowering the parasitic capacitance at the input. The basic circuit design is shown in Figure 5.13b with the whole circuit broken into two parts, the voltage follower and differential amplifier. In theory a differential amplifier is all that would be needed if we are comparing the voltage from the tip relate to the sample (at ground potential). In practice the differential amplifier is susceptible to many noise sources. If common mode noise is present (noise that would be present, or common to both inputs) then the suppression of this noise depends on the impedance of the source. To suppress the common mode noise and not to load down the source the high input impedance ADA4530 are placed into what is known as a voltage follower configuration. This allows for the signal to be converted from a high input impedance signal (vulnerable to noise) to a low impedance signal. The tip side is the thermoelectric voltage signal relative to the sample which is either floating or at ground

potential. The resistors $R_1$ and $R_2$ in the differential amplifier portion of the circuit are used to define the gain. The output voltage can be calculated

$$v_o = v_i \frac{R_2}{R_1} \tag{5.2}$$

the resistors are chosen so that a gain between 100-250x. The resistors should be matched as close as possible so that the CMRR can be as large as possible (the tolerance should be 0.1%).[35] As a first prototype for the board a two-layer printed circuit board (PCB) will be built. In order to test the circuit a voltage source is needed which can output a bipolar voltage down to a few microvolts. This can be done with a battery powered low impedance power supply that is capable of microvolt signal generation. There are anticipated issues that come with using a 2 -layer board versus a four layer. The power supplies rails, as well as any other voltages on the board can interfere with the input (before the voltage followers) and the output signal (after the voltage followers leading into the differential amplifier). In addition, proper board practices for low voltage, high impedance measurements demand certain precautions be taken so that full advantage can be taken of the low noise characteristics of the amplifier. As discussed earlier a guard buffer can protect the input of the signal, in this case to the voltage follower, by minimizing the effects of stray capacitance. Figure 5.13c shows an outline for a board configuration that utilizes many important design rules for low noise current/voltage measurements. These include the use of a guard ring (this is using the integrated guard in the ADA4530) with a perforated fence that protects the input from electromagnetic coupling of the input, with the guard ring extending to below the board as shown in Figure 5.13d. In addition, there is an entire metal strip surrounding the whole interior which a shield casing can be placed

over and held at ground potential. Another important consideration is the type of laminate used in the PCB. A property known as dielectric relaxation can occur in insulators that can affect the performance of low noise circuits (such as those measuring high impedance or low fA). Dielectric relaxation is a delay in polarization of the molecules that make up the

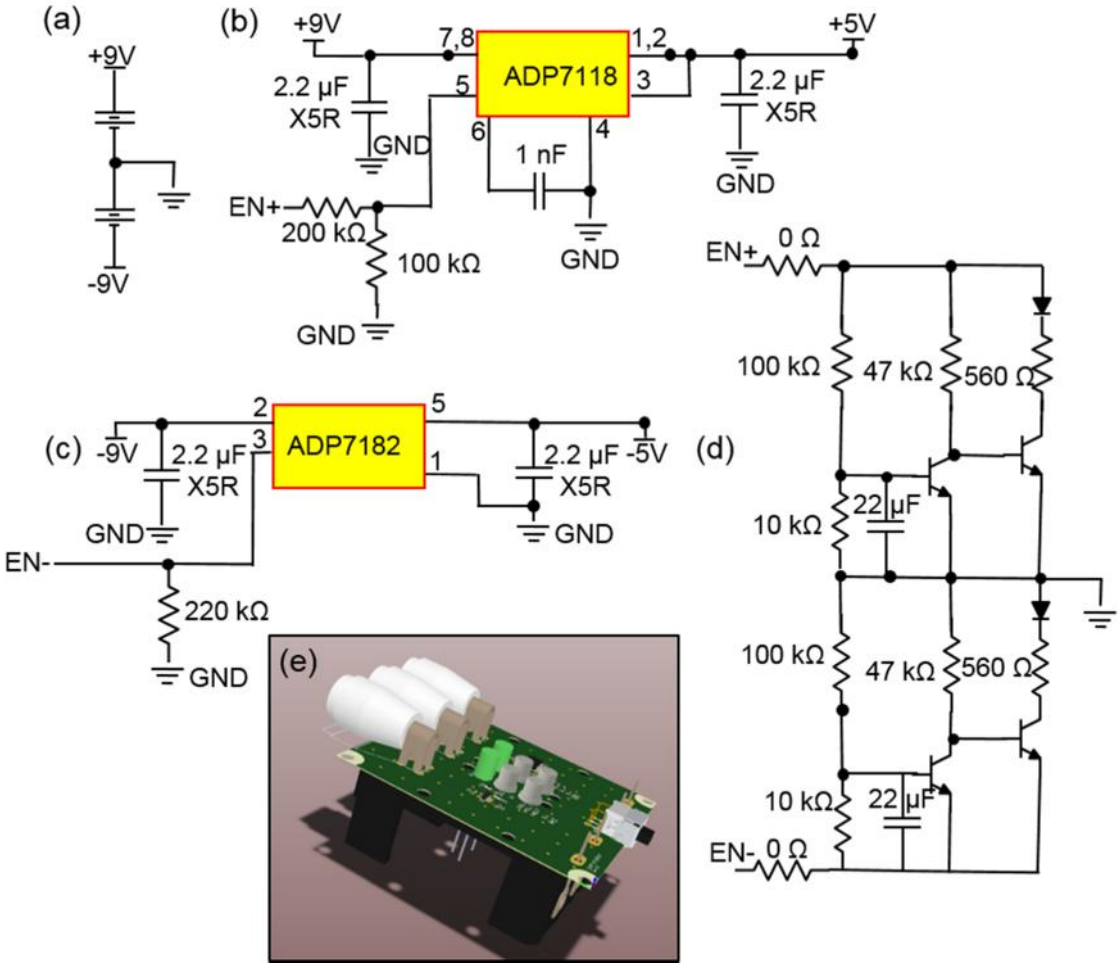


**Figure 5.14.** Circuit schematic for connecting two 9 V batteries for creating dual ±9 V output (a). Circuit schematic of low noise linear regulator ADP7118 for +5V output (b) and Circuit schematic of low noise linear regulator ADP7182 for -5V output (c). Circuit schematic for displaying the battery power state with LEDs (d). 3D model of power supply circuit (e).

dielectric to a change in an electric field. When there are small displacements in current flow through an insulator the time it takes to dissipate this will dominate the settling time of the circuit, a property that is very detrimental to scanning based experiments that rely on high bandwidth. Therefore, instead of using the industry standard FR-4 glass epoxy dielectric material (which can require up to 1 hour to dissipate currents less than 10 fA) the use of Rodgers 4350B ceramic can be used (which can dissipate currents as low as 1 fA within 20 secs). Last but not least is contamination. If the PCB has contamination as a result of oil, dust, solder flux, etc. then everything that has been mentioned for minimizing noise will be in vein.

All the amplifiers that would be used in the instrumentation amplifier configuration need to be powered (these are not passive components like resistors or capacitors). There is some simplicity with using an AC power source however, by using a battery to power the amplifiers we can avoid, to some extent, AC couple line noise and ground loops.[15, 35] When considering powering with batteries we need to consider capacity of the battery, the discharge rate, the current drawn from the op-amp and how long we would like the circuit to run. Ideally, we would like the circuit to run consecutively for 24 hours. The current drawn from the op amps is about 0.9 mA and the capacity of the 9V lithium ion batteries in the dual power supply is about 750mAh. Let us assume the circuit is drawing 3 mA an hour at 1 C, then we expect the battery to supply the energy to the system for 250 hours. In practice the battery will draw this with no load on the circuit. As soon as we connect it to the load it is possible that the op amps will draw more power, especially at high frequencies. Since we wish to measure both positive and negative

voltages a dual rail power supply is needed, which means connecting the batteries in series where the positive side of one battery is connected to the negative of the other which is then considered ground. Figure 5.14a shows the circuit schematic for the output of the battery connection, the output of the battery is ±9 V however our op amps can only accept no higher than 8 V. In addition, we need to make sure that the voltage has a large power supply rejection ratio (PSRR), which is the ability for the amplifier to maintain an output voltage even with a varied DC power supply. The best option is to use low noise linear regulators both for the positive (ADP7118) and the negative (ADP7182) rail. The circuit diagram of the conversion of ±9V to ±5V using the linear regulators is shown in Figure 5.14b. The $EN\_{\pm}$ pin of the circuit acts as the switch for the power supply where the batteries voltage must be at least 1.2 V for a voltage output to be present. The batteries power can be checked with the second circuit as shown in Figure 5.14c, if the voltage drops below 3V the LEDs will turn on. The batteries can then be removed and charged to their full capacity. As of the writing of this thesis the power supply board is being assembled and will be tested to ensure a stable DC output and for powering a configured transimpedance amplifier.

## 5.4 Conclusion

The instrumentation and applications of scanning thermoelectric voltage microscopy has been reviewed in detail. A preliminary study using a voltage amplifier and commercial atomic force microscope demonstrated that a large number of noise sources are present that can distort the thermoelectric voltage signal we are trying to measure. By knowing the origin of these sources and taking special care to eliminate stray capacitance

and electromagnetic interference, high impedance measurements are possible. An instrumentation amplifier, powered with lithium ion batteries, meant for providing low noise, high bandwidth voltage measurements was designed. The instrumentation amplifier, once built, will be tested on a set of standard samples with varying sample impedance and Seebeck coefficients. If successful this amplifier will be very useful for investigating samples with subtle variations in the density of states, such as vacancy, defects, standing waves, all at room temperature and ambient air conditions.

## 5.5 References


1. Cahill, D. G.; Ford, W. K.; Goodson, K. E.; Mahan, G. D.; Majumdar, A.; Maris, H. J.; Merlin, R.; Phillpot, S. R. Nanoscale thermal transport. *J Appl Phys* **2003**, *93* (2), 793-818.

2. Li, G.; Mao, B.; Lan, F.; Liu, L. Practical aspects of single-pass scan Kelvin probe force microscopy. *Review of Scientific Instruments* **2012**, *83* (11), 113701.

3. Homoth, J.; Wenderoth, M.; Druga, T.; Winking, L.; Ulbrich, R. G.; Bobisch, C. A.; Weyers, B.; Bannani, A.; Zubkov, E.; Bernhart, A. M.; Kaspers, M. R.; Moller, R. Electronic transport on the nanoscale: ballistic transmission and Ohm's law. *Nano Lett* **2009**, *9* (4), 1588-92.

4. Druga, T.; Wenderoth, M.; Homoth, J.; Schneider, M. A.; Ulbrich, R. G. A versatile high resolution scanning tunneling potentiometry implementation. *Rev Sci Instrum* **2010**, *81* (8), 083704.

5. Schumacher, Z.; Miyahara, Y.; Spielhofer, A.; Grutter, P. Measurement of Surface Photovoltage by Atomic Force Microscopy under Pulsed Illumination. *Physical Review Applied* **2016**, *5* (4), 044018.

6. Williams, C. C.; Slinkman, J.; Hough, W. P.; Wickramasinghe, H. K. Lateral Dopant Profiling on a 100 Nm Scale by Scanning Capacitance Microscopy. *J Vac Sci Technol A* **1990**, *8* (2), 895-898.

7. Liu, D.; Mo, K.; Ding, X.; Zhao, L.; Lin, G.; Zhang, Y.; Chen, D. Secondary resonance magnetic force microscopy using an external magnetic field for characterization of magnetic thin films. *Appl Phys Lett* **2015**, *107* (10), 103110.

8. Baumann, S.; Paul, W.; Choi, T.; Lutz, C. P.; Ardavan, A.; Heinrich, A. J. Electron paramagnetic resonance of individual atoms on a surface. *Science* **2015**, *350* (6259), 417-420.

9. Cox, P. A. *The electronic structure and chemistry of solids*; Oxford University Press: Oxford [Oxfordshire]; **1987**.

10. Wu, K. H.; Hung, C. I.; Ziolkowski, P.; Platzek, D.; Karpinski, G.; Stiewe, C.; Mueller, E. Improvement of spatial resolution for local Seebeck coefficient measurements by deconvolution algorithm. *Review of Scientific Instruments* **2009**, *80* (10), 105104.

11. Zhang, Y.; Hapenciuc, C. L.; Castillo, E. E.; Borca-Tasciuc, T.; Mehta, R. J.; Karthik, C.; Ramanath, G. A microprobe technique for simultaneously measuring thermal conductivity and Seebeck coefficient of thin films. *Appl Phys Lett* **2010**, *96* (6), 062107.

12. Williams, C. C.; Wickramasinghe, H. K. Microscopy of Chemical-Potential Variations on an Atomic Scale. *Nature* 1990, *344* (6264), 317-319.

13. Stovneng, J. A.; Lipavsky, P. Thermopower in Scanning-Tunneling-Microscope Experiments. *Physical Review B* **1990**, *42* (14), 9214-9216.

14. Maksymovych, P. Distance dependence of tunneling thermovoltage on metal surfaces. *J Vac Sci Technol B* **2013**, *31* (3).

15. Poler, J. C.; Zimmermann, R. M.; Cox, E. C. Scanning Thermopower Microscopy of Guanine Monolayers. *Langmuir* **1995**, *11* (7), 2689-2695.

16. Sotthewes, K.; Siekman, M. H.; Zandvliet, H. J. W. A method to measure the thermovoltage with a high spatial resolution. *Appl Phys Lett* **2016**, *108* (14).

17. Schneider, A.; Wenderoth, M.; Engel, K. J.; Rosentreter, M. A.; Heinrich, A. J.; Ulbrich, R. G. Local electronic structure at steps on Au(111) investigated by the thermovoltage in scanning tunneling microscopy. *Appl Phys a-Mater* **1998**, *66*, S161-S165.

18. Maksymovych, P.; Kelly, S. J.; Cerda, J. I. Surface-State Enhancement of Tunneling Thermopower on the Ag(111) Surface. *ACS Nano* **2014**, *8* (12), 12110-12119.

19. Moller, R.; Baur, C.; Esslinger, A.; Kurz, P. Scanning Noise Potentiometry. *J Vac Sci Technol B* **1991**, *9* (2), 609-611.

20. Hoffmann, D.; Haas, A.; Kunstmann, T.; Seifritz, J.; Moller, R. Thermovoltage in scanning tunneling microscopy. *J Vac Sci Technol A* **1997**, *15* (3), 1418-1422.

21. Homoth, J.; Wenderoth, M.; Engel, K. J.; Druga, T.; Loth, S.; Ulbrich, R. G. Reconstruction of the local density of states in Ag(111) surfaces using scanning tunneling potentiometry. *Phys Rev B* **2007**, *76* (19).

22. Hoffmann, D.; Seifritz, J.; Weyers, B.; Moller, R. Thermovoltage in scanning tunneling microscopy. *J Electron Spectrosc* **2000**, *109* (1-2), 117-125.

23. Park, J.; He, G.; Feenstra, R. M.; Li, A. P. Atomic-scale mapping of thermoelectric power on graphene: role of defects and boundaries. *Nano Lett* **2013**, *13* (7), 3269-73.

24. Cho, S.; Kang, S. D.; Kim, W.; Lee, E. S.; Woo, S. J.; Kong, K. J.; Kim, I.; Kim, H. D.; Zhang, T.; Stroscio, J. A.; Kim, Y. H.; Lyeo, H. K. Thermoelectric imaging of structural disorder in epitaxial graphene. *Nat Mater* **2013**, *12* (10), 913-8.

25. Lee, E.-S.; Cho, S.; Lyeo, H.-K.; Kim, Y.-H. Seebeck Effect at the Atomic Scale. *Physical Review Letters* **2014**, *112* (13), 136601.

26. Balachandran, J.; Reddy, P.; Dunietz, B. D.; Gavini, V. End-Group-Induced Charge Transfer in Molecular Junctions: Effect on Electronic-Structure and Thermopower. *J Phys Chem Lett* **2012**, *3* (15), 1962-1967.

27. Tan, A.; Sadat, S.; Reddy, P. Measurement of thermopower and current-voltage characteristics of molecular junctions to identify orbital alignment. *Appl Phys Lett* **2010**, *96* (1).

28. Kushvaha, S. S.; Hofbauer, W.; Loke, Y. C.; Singh, S. P.; O'Shea, S. J. Thermoelectric measurements using different tips in atomic force microscopy. *J Appl Phys* **2011**, *109* (8), 084341.

29. Miao, R.; Xu, H.; Skripnik, M.; Cui, L.; Wang, K.; Pedersen, K. G. L.; Leijnse, M.; Pauly, F.; Wärnmark, K.; Meyhofer, E.; Reddy, P.; Linke, H. Influence of Quantum Interference on the Thermoelectric Properties of Molecular Junctions. *Nano Letters* **2018**, *18* (9), 5666-5672.

30. Zhao, M.; Kim, D.; Nguyen, V. L.; Jiang, J.; Sun, L.; Lee, Y. H.; Yang, H. Coherent Thermoelectric Power from Graphene Quantum Dots. *Nano Letters* **2019**, *19* (1), 61-68.

31. Petersen, J. P.; Kandel, S. A. Circuit design considerations for current preamplifiers for scanning tunneling microscopy. *J Vac Sci Technol B* **2017**, *35* (3), 033201.

32. Carlà, M.; Lanzi, L.; Pallecchi, E.; Aloisi, G. Development of an ultralow current amplifier for scanning tunneling microscopy. *Review of Scientific Instruments* **2004**, *75* (2), 497-501.

33. Moore, J. H.; Davis, C. C.; Coplan, M. A.; Greer, S. C. *Building scientific apparatus* [Online]; 4th ed. ed; Cambridge University Press: Cambridge, UK ;, **2009**.

34. Reddy, P.; Jang, S. Y.; Segalman, R. A.; Majumdar, A. Thermoelectricity in molecular junctions. *Science* **2007**, *315* (5818), 1568-1571.

35. Horowitz, P.; Hill, W. *The art of electronics*; 2nd ed. ed.; Cambridge University Press: Cambridge [England] ; **1989**.

# CHAPTER VI

# SUMMARY AND OUTLOOK

## 6.1 Summary

The work presented in this dissertation has shown how bottom-up methodologies can be used to fabricate a diverse set of hierarchical nanomaterials. The electrical properties of these materials were assessed using electrochemical means or using scanning probe technologies. Chapter I was an overview giving necessary details as to how nanostructuring can alter the physical properties of materials and methods to fabricate these structures using covalent and non-covalent interactions. The use of sol-gel as a low cost templating precursor for colloidal crystal lithography was also discussed.

Chapter II showed how patterning with a sol-gel precursor and colloidal particle lithography lead to a monolayer inverse opal $V_2O_5$ with an increase in electrochemical activity as assessed by cyclic voltammetry. An increase in capacity at charge/discharge rates of 1C compared to the thin film were also realized with this system. Additionally the morphology of the surface was assessed before and after cycling which indicated that the inverse opal structure appeared to be more mechanically robust under continuous cycling.

Sol-gel derived chemistries are very robust and allow a large number of materials to be fabricated. Following from the work with $V_2O_5$, $MoO_3$ sol-gels were prepared and casted on carbon fiber paper. The $MoO_3$ was crystallized under Ar at 400 $^oC$ and then sulfurized by either chemical vapor deposition or hydrothermal means. The catalytic activity of these materials was assessed electrochemically by determining the overpotential at 10 $mA/cm^2$. It was found that hydrothermal sulfurization appears to have

the highest catalytic activity compared to other preparation methods. Theoretical calculations sought to understand this enhancement and suggests that $MoS_2/MoO_3$ interfacial chemistry may play an important role in the enhanced activity. This is supported by other work and lower mass loading studies.

Work in Chapter IV focused on how noncovalent interactions (as outlined in Chapter I) can be used to create organic nanostructures. In particular porphyrin nanowires were assembled through ionic assembly by means acidification. The wires have applications in dye sensitized solar cells but their electrical characteristics are not well understood. A modified commercial AFM was used to study the electrical properties of these assembled structures, in particular their IV characteristics. It was found that the IV characteristics are thickness dependent with the LUMO state being shift to higher voltages as the thickness increases.

Using the same modified conductive probe microscope Chapter V attempted a proof of concept study to see if it was possible to perform single point thermoelectric voltage measurements under ambient conditions. An overview of important milestones in instrumentation and materials investigated using scanning thermalvoltage was presented. The noise sources were analyzed and a circuit was designed (both power supply and measuring circuit) in order to develop a low noise, high bandwidth voltage amplifier for scanning thermoelectric voltage microscopy.

## 6.2 Outlook

The work summarized in Section 6.1 provides an approach to bottom-up assembly for constructing various inorganic and organic nanostructures using templating and non-covalent interactions. The nanostructuring can have significant impacts on the measured properties of a material, but correlating how the structuring will affect the phase, crystallite domains and density of states is still an active area of research. The use of colloidal crystal templating, especially forming monolayers of inverse opal structures, may find a use in detecting inhomogeneities in charge localization and local structural distortions in inverse opal $V_2O_5$. Scanning transmission x-ray microscopy is a powerful tool that can provide information on trapped electron density (incident photon as a function of absorbance) which can be correlated to lithiation gradients.[1, 2] This could further reflect barriers to phase transformations that would be seen in the V3$d_{xy}$ level and $t_{2g}$ and $e_g^*$.

The patterning approach for sol-gel $MoS_2$ as described in chapter III shows that chemistry ultimately plays the most important role in the catalytic performance in hydrogen evolution reaction. There are still many questions that need to be addressed concerning this work. Information regarding the elemental composition and oxidation states need to be determined using X-ray photoelectron spectroscopy. Data is also needed for determining the electrochemically active surface area, the electrochemical impedance spectroscopy circuit analysis, the turn over frequency of the catalysis and a stability study (1000 polarization curves). Also it may be much easier to investigate the role of patterning by using substrates that are flat rather than the high surface area carbon fiber paper. In this way the contributions of electronic structure and electrochemical surface area could be

distinguished and help to elucidate the mechanisms for the hydrogen evolution. It also should be noted that the spheres that were used in this study were very large (~2.5 μm) and that there is work that suggests that smaller diameter spheres would lead to increase in activity. This assume that the limiting rate is the adsorption of the hydrogen species onto the catalyst and not the addition of an electron to form hydrogen gas. There is still work to be done in this area and careful tuning of the band structure through chemical doping and appropriate hierarchical structuring for increased surface area and structural stability.

The TCPP porphyrin nanowires described in Chapter IV have additional work needed. Having worked out a relatively straight forward way to take IV curves on the wires additional work is needed to see the thickness dependence down to a single layer of porphyrin materials (~2 nm). There is also the question of how confinement might affect the nanostructure of the materials. What happens when the porphyrin wire dimension is decreased (either through mechanical means such as using an AFM tip or through high energy sonication), that is, does the bandgap increase, is there a change on either side of the curve? Focusing a laser on the nanowire near the absorption edge (based on UV vis around, a 488 nm laser would work) would allow for characterizing the vertical photocurrents at zero or low biases and possibly optical absorption imaging.[3] There is also a need to understand the horizontal charge transport which can only be performed using metal (could also use a conductive polymer poly(3,4-ethylenedioxythiophene) (PEDOT) to eliminate band bending) contacts on the nanowires. Through this single wire charge transport measurements can be performed with a light source and without one. With the

contacts made on a surface such as $Si/SiO_2$ gating experiments could be performed to understand the local doping behavior of the nanowires using conductive probe.[4] As an extension into applications it might be interesting to see how the photovoltage generated in a dye sensitized solar cell using an inverse opal $TiO_2$ with the TCPP nanowires performs on an FTO substrate (which could also be an inverse opal structure).

Energy conversion materials in some cases will have defects which lead to an alteration of the intrinsic bandstructure scanning thermoelectric voltage outlined in Chapter V is an attempt to understand and design a low noise, high bandwidth voltage amplifier for directly accessing these states. In general no ambient pressure atomic force/scanning thermoelectric voltage microscope has been demonstrated in the literature. Experiments are still needed to build the board, assess its noise floor and modify the board as necessary. As mentioned for Chapter IV a gated conductive probe set-up would greatly aid in understanding where the Fermi-level lies relative the conduction and valence band edges (or HOMO-LUMO for organic systems).[4] This would be accomplished using a $SiO_2$ dielectric on Si and evaporated metal contacts. This would be especially useful for heterostructures of 2D materials which are likely to have exotic electronic characteristics at edges and on or near defect sites on one of the two materials. Another interesting outlook would be the use of a q-plus (self-actuating tuning fork) sensor as this allows simultaneous AFM/STM and the small amplitudes used have been shown to be directly related to the Lennard Jones potential.[5] If the van der Waals interactions can be directly measured, then the implications for modeling the scanning thermoelectric voltage images (as described in some detail in Chapter V) means a higher confidence of assessing the identity of the

defect/dopant/adsorbate. Since there would be a solvation layer under ambient conditions it is likely that the sample would need to be placed under an inert atmosphere and the heater stage heated to around 50 $^{o}$C (or more) to remove residual water from the surface before doing the experiments. There is also a question of the role of the tip in the use of AFM based scanning thermoelectric voltage. If STM is used all metal wires are used and the conductivity does not change readily. While using contact mode the torsion from the cantilever leads to shear forces that has been shown to lead to tip wear. In Chapter V all metal AFM tips were used and were found to be superior to metal coated probes in terms of reliability and conductivity. For a symmetric junction (if using Au(111) as the substrate) all metal gold probes could be fabricated rather easily with radius of curvature down to approximately 30 nm.[6, 7, 8] A cleaning procedure utilizing an ion gun (not to be confused with focused ion beam) in vacuum with a positive 100-400 V applied to the tip can be used to mill the tip down to less than a 2 nm.[9] Although the pressures would be very large the tip would be very clean and could be sharpened again about 3 more times. These tips could then not only be used for scanning thermoelectric voltage but also for other AFM/STM based experiments such as tip enhanced Raman spectroscopy (TERS), photo-thermal spectroscopy, photocurrent etc.

## 6.3 References

1. Andrews, J. L.; De Jesus, L. R.; Tolhurst, T. M.; Marley, P. M.; Moewes, A.; Banerjee, S. Intercalation-Induced Exfoliation and Thickness-Modulated

Electronic Structure of a Layered Ternary Vanadium Oxide. *Chemistry of Materials* **2017,** *29* (7), 3285-3294.

2. De Jesus, L. R.; Andrews, J. L.; Parija, A.; Banerjee, S. Defining Diffusion Pathways in Intercalation Cathode Materials: Some Lessons from V2O5 on Directing Cation Traffic. *ACS Energy Letters* **2018,** *3* (4), 915-931.
3. Rodriguez, R. D.; Madeira, T. I.; Sheremet, E.; Bortchagovsky, E.; Mukherjee, A.; Hietschold, M.; Zahn, D. R. T. Optical Absorption Imaging by Photothermal Expansion with 4 nm Resolution. *Acs Photonics* **2018,** *5* (8), 3338-3346.
4. Lu, C. P.; Li, G.; Mao, J.; Wang, L. M.; Andrei, E. Y. Bandgap, mid-gap states, and gating effects in MoS2. *Nano Lett* **2014,** *14* (8), 4628-33.
5. Giessibl, F. J. The qPlus sensor, a powerful core for the atomic force microscope. *Rev Sci Instrum* **2019,** *90* (1).
6. Tallarida, N.; Lee, J.; Apkarian, V. A. Tip-Enhanced Raman Spectromicroscopy on the Angstrom Scale: Bare and CO-Terminated Ag Tips. *Acs Nano* **2017,** *11* (11), 11393-11401.
7. Macpherson, J. V.; Unwin, P. R. Combined scanning electrochemical-atomic force microscopy. *Anal Chem* **2000,** *72* (2), 276-285.
8. Kolchuzhin, V. A.; Sheremet, E.; Bhattacharya, K.; Rodriguez, R. D.; Paul, S. D.; Mehner, J.; Hietschold, M.; Zahn, D. R. T. Mechanical properties and applications of custom-built gold AFM cantilevers. *Mechatronics* **2016,** *40*, 281-286.
9. Schmucker, S. W.; Kumar, N.; Abelson, J. R.; Daly, S. R.; Girolami, G. S.; Bischof, M. R.; Jaeger, D. L.; Reidy, R. F.; Gorman, B. P.; Alexander, J.; Ballard,

J. B.; Randall, J. N.; Lyding, J. W. Field-directed sputter sharpening for tailored probe materials and atomic-scale lithography. *Nat Commun* **2012,** *3*.